CZECH TECHNICAL UNIVERSITY IN PRAGUE
FACULTY OF NUCLEAR SCIENCES AND PHYSICAL ENGINEERING

Ph.D. THESIS
HYDRODYNAMIC SIMULATIONS OF HEAVY ION COLLISIONS

PRAGUE 2016 **MARTIN SCHULC**

Bibliografický záznam

Autor	Ing. Martin Schulc, České vysoké učení technické v Praze, Fakulta jaderná a fyzikálně inženýrská, Katedra fyziky, Břehová 7, 115 19 Praha 1
Název práce	Hydrodynamické simulace srážek těžkých iontů
Studijní program	Aplikace přírodních věd
Studijní obor	Jaderné inženýrství
Školitel	doc. Mgr. Boris Tomášik, Ph.D., České vysoké učení technické v Praze, Fakulta jaderná a fyzikálně inženýrská, Katedra fyziky, Břehová 7, 115 19 Praha 1
Akademický rok	2015/2016
Počet stran	115
Klíčová slova	Srážky těžkých iontů, anizotropický tok, hydrodynamické simulace, výtrysky částic

Bibliographic entry

Author	Ing. Martin Schulc, Czech Technical University in Prague, Faculty of Nuclear Sciences and Physical Engineering, Department of Physics Břehová 7, 115 19 Praha 1
Title of Dissertation	Hydrodynamic simulations of heavy ion collisions
Degree Programme	Applications of Natural Sciences
Field of Study	Nuclear Engineering
Supervisor	doc. Mgr. Boris Tomášik, Ph.D., Czech Technical University in Prague, Faculty of Nuclear Sciences and Physical Engineering, Department of Physics Břehová 7, 115 19 Praha 1
Academic year	2015/2016
Number of Pages	115
Keywords	Heavy ion collisions, anisotropic flow, hydrodynamic simulations, jets

Abstrakt:

Při nejvyšších možných dosažitelných energiích v jádro-jaderných srážkách na LHC vzniká velké množství párů výtrysků částic, které deponují čtyřhybnost do expandujícího média. Pomocí trojrozměrné relativistické hydrodynamické simulace se ukazuje, že tato skutečnost vede k měřitelnému příspěvku k anizotropii v expanzi v příčném směru. Tvrdé partony vytvářejí proudy v plazmatu, které se slévají, pokud tečou blízko sebe. Tento mechanismus koreluje příspěvek k anizotropii s geometrií fireballu a zvyšuje hodnotu anisotropického toku v necentrálních srážkách.

Abstract:

In nuclear collisions at highest accessible LHC energies, a lot of dijet pairs deposit momentum into the deconfined expanding medium. This thesis uses 3+1-dimensional relativistic hydrodynamic simulation to show that this leads to measurable contribution to the anisotropy of collective transverse expansion. Hard partons generate streams in plasma which merge if they come close to each other. This mechanism correlates the resulting contribution to flow anisotropy with the fireball geometry and causes an increase of the anisotropic flow in non-central collisions.

Čestné prohlášení

Prohlašuji, že jsem disertační práci na téma Hydrodynamické srážky těžkých iontů vypracoval samostatně s použitím odborné literatury a pramenů, uvedených na seznamu, který tvoří přílohu této práce.

Podpis uchazeče

Datum 25.5. 2016 …….

Ing. Martin Schulc

List of abbreviations

ALICE	A Large Ion Collider Experiment
AMY	Arnold-Moore-Yaffe jet quenching model
ATLAS	A Toroidal LHC ApparatuS
BDMPS	Baier-Dokshitzer-Mueller-Peigne-Schiff jet quenching model
CGC	Color Glass Condensate
EoS	Equation of State
ETBFCT	Type of Flux Corrected Transport algorithm
FAIR	Facility for Antiproton and Ion Research
FCT	Flux corrected transport algorithm
GC	Grand Canonical
GLV	Gyulassy-Levai-Vitev description of induced jet energy loss
GSI	GSI Helmholtz Centre for Heavy Ion Research
HT	Higher Twist jet quenching model
IC	Initial Conditions
JIMWLK	Jalilian-Marian-Iancu-McLerran-Weigert-Leonidov-Kovner equation for the evolution of small-x QCD wavefunctions
JINR	Joint Institute for Nuclear Research
LHC	Large Hadron Collider
LCPFCT	Type of Flux Corrected Transport algorithm
MC	Monte-Carlo
MC-KLN	Monte-Carlo Kharzeev-Levin-Nerdi model
POI	Particle Of Interest
QCD	Quantum Chromodynamics
QGP	Quark Gluon Plasma
RFP	Reference Particle
RHIC	Relativistic Heavy Ion Collider
SHASTA	SHArp and Smooth Transport Algorithm
sQGP	strongly coupled QGP
THERMINATOR	THERMal heavy IoN generATOR
YDFCT	Type of Flux Corrected Transport algorithm

Contents

1 Introduction **9**

2 Heavy-ion collisions **10**
2.1 QGP and Quantum Chromodynamics 10
2.2 Experimental observables and signatures for the QGP 14
2.2.1 Charged-particle multiplicity density 14
2.2.2 Jets and high p_T suppression 15
2.2.3 Quarkonium suppression 19
2.2.4 Anisotropic flow 20
2.2.5 Flow fluctuations and non-flow correlations 21

3 Goals and motivation **23**

4 Hydrodynamics and its application **26**
4.1 Ideal relativistic hydrodynamics 26
4.2 Relativistic viscous hydrodynamics 28
4.3 Transformation between the Laboratory Frame and the Local Rest Frame . 31
4.4 Milne coordinates 32
4.5 Equation of state 34
4.6 Freeze-out 36
4.7 Brief overview of statistical models 38
4.8 THERMINATOR2 description 41

5 Numerical methods for solving hydrodynamic equations **44**
5.1 SHASTA 45
5.2 One-dimensional application of SHASTA algorithm 45
5.2.1 Three-dimensional application of SHASTA algorithm 46
5.3 Numerical tests of implemented algorithm 48
5.3.1 Static tests 49

6 Initial conditions for hydrodynamics **55**
6.1 Optical Glauber model for heavy-ion collisions 57
6.2 LHC inspired initial conditions 58
6.3 Tests for expanding medium 60
6.4 Initial fluctuation characterization 62
6.5 State-of-the-art initial conditions 70
6.5.1 Glauber Monte Carlo approach 70

6.5.2 Fluctuating glasma initial conditions 71

7 Jet energy loss **74**
7.1 Basics of perturbative QCD based approaches 75
7.2 Implemented jet energy loss 76

8 Anisotropic flow analysis methods **79**
8.1 The event plane method 79
8.2 Particle cumulants 80
8.2.1 Reference flow 81
8.2.2 Differential flow 82

9 Results **84**
9.1 Static medium results 85
9.2 Expanding medium results 95

10 Conclusions **101**
List of publications 103
Presentations at international conferences 104
References 105

Chapter 1

Introduction

Relativistic heavy-ion collisions provide the opportunity to recreate and study under laboratory conditions a form of matter, which is believed to have existed in the early phase of the Universe, the Quark-Gluon Plasma (QGP). The Large Hadron Collider (LHC) is the worlds largest and most powerful particle accelerator at CERN located in Switzerland near Geneva. The QGP does not exist at ordinary temperatures and energy densities. However, in the ultrarelativistic high energy collisions of heavy ions, currently performed at BNL's Relativistic Heavy Ion Collider (RHIC) and CERN's Large Hadron Collider (LHC), sufficiently large temperatures and energy densities required for QGP formation can be achieved [1]. Even at the highest collision energies, the time scale for which highly energetic and dense matter is formed in heavy-ion collisions is short, about 10 fm/c. The system thermalizes locally, expands and breaks up and only final state particles remain as remnants of the collision. Only these particles and their decay products can be measured by a detector. Models or simulations are needed to provide a connection to the early phases of the collision which are of highest interest.

The thesis is organized as follows. Firstly, the theoretical relativistic heavy ion collisions background is given, including QGP, QCD phase transitions and some QGP signatures. In Chapter 3, the main goals and motivation of the thesis are presented. Chapter 4 deals with the theory of hydrodynamics and its application since ideal three-dimensional hydrodynamics was used in this thesis including description of freeze-out process. Chapter 5 provides the details about numerical implementation of solving hydrodynamic equations which are developed. Chapter 6 describes the types of initial conditions used in heavy ion physics and points out those used in this thesis. The implemented source terms for hydrodynamics and jet quenching models are presented in Chapter 7. Chapter 8 provides the details concerning the methods for extracting anisotropic flow. Our results for both static and expanding medium are presented in Chapter 9. The most important results are summarized in concluding Chapter. Throughout this thesis, we will use natural units, i.e. $c = k_B = \hbar = 1$.

Chapter 2

Heavy-ion collisions

This chapter focuses on the QGP as described by the theory of strongly interacting matter, Quantum Chromodynamics (QCD). QGP is the state of matter consisting of deconfined quarks and gluons, mutually interacting dominantly via the strong nuclear force. The experimental signatures of the deconfined matter are reviewed, as well.

2.1 QGP and Quantum Chromodynamics

Quantum Chromodynamics is a part of the Standard Model, the state-of-the-art theory of particle physics, describing the strong interaction between quarks and gluons. Gluons are bosons which carry the strong interaction between quarks. There are six known types of quarks: up, down, strange, charm, bottom and top. Quarks carry the SU(3) charge which due to its analogy with addition of colours is often referred to as colour with states described as red, green, and blue. Antiquarks then carry the complementary colours to these. The interaction in QCD is invariant under the SU(3) transformation in colour space. Combination of a colour and anticolour is assigned to each gluon. There are nine of such combinations. They are divided into a singlet and an octet state according to the properties of the SU(3) group symmetry. Experimental results show that gluons belong to the octet state. In fact all known hadrons are colour-neutral, and it seems that Nature avoids free colour charge. This is known as colour confinement. While potential energy of the gravity and the electromagnetic interaction between two charges has an upper limit, potential energy of two quarks is rising linearly. This is known as colour confinement. This means that two quarks moving away from each other will increase the energy in the colour field between them, until at some point the stored energy is converted into a new quark-antiquark pair, thus the original quarks are confined in two new hadrons, each with one of the newly created quarks. In the opposite limit, in case of large momentum transfers, the coupling becomes weak and therefore the fundamental degrees of freedom, quarks and gluons, are quasifree. Effectively, this means that at some distance, where two quarks are very close to each other, they will not interact via the strong force at all, they are free quarks. This is known as asymptotic freedom, and is of great importance in the field of heavy ion physics [2].

Strongly interacting matter can occur in various phases. A phase describes a state of system in thermal equilibrium which is characterized by a certain set of macroscopic observables. Phase transitions are characterized by the change of the relevant thermodynamic variable(s) and are commonly classified into phase transitions of first order, second order and cross-over. Generally, there is an nth order phase transition if the (n–1)th derivative of a thermodynamic variable (like the energy density or the number density) is discontinuous. While first-order transition always implies the existence of a mixed phase, second order transition does not exhibit a mixed phase. If the characteristic observables change rapidly, but without any discontinuity, the transition is called a cross-over and the actual transition between the phases cannot be exactly specified.

The QCD phase diagram (see Fig. 2.1) is obtained by plotting the relevant degrees of freedom for strongly interacting matter. Commonly, these degrees of freedom are studied as a function of temperature T and quark chemical potential μ which is associated with baryon number. Thus, for vanishing quark chemical potential, an equal number of quarks and antiquarks is present in the system. A positive quark chemical potential implies an excess of quarks over antiquarks. For low temperatures and small values of the quark chemical potential, strongly interacting matter forms hadron gas. At sufficiently high temperature and/or chemical potential, hadrons strongly overlap, creating an extended region of deconfined quark-gluon matter, the QGP [3, 4, 5]. Lattice-QCD calculations have shown that the transition between the hadronic and quark-gluon plasma phases of quantum chromodynamics (QCD) at vanishing baryon chemical potential μ_B and around $T \approx 170$ MeV is a crossover transition [6]. For higher values of quark chemical potential there is a first-order phase transition which ends in a critical end point of second order. Several attempts have been made to locate the critical point, i.e. the endpoint of the first-order transition line, in lattice simulations [7, 8, 9], but its location is still in doubt [10]. The inconclusive theoretical results have motivated plans for a systematic exploration of the properties of hot QCD matter as a function of the net baryon density by means of a collision energy scan at the Relativistic Heavy Ion Collider (RHIC) [11, 12]. The search for the QCD critical point also forms part of the motivation for the NA61 experiment [13] at the CERN-SPS and for a new facility dedicated to the study of compressed baryonic matter at the Facility for Antiproton and Ion Research (FAIR) in Germany as well as the NICA facility in JINR Dubna. For cold and dense quark matter another phase transition is proposed. Due to the attractive interaction between quarks in some channels the formation of Cooper pairs is expected. This phase is commonly referred to as color-superconducting [14, 15] and seems to contain a variety of additional phases [16]. At high temperatures, the nature of the QGP is not yet fully explored. At medium-high temperatures, the QGP is most probably not an ideal gas of non-interacting quarks and gluons [17], but behaves like a strongly coupled plasma (strongly coupled QGP, sQGP) corresponding to an ideal fluid.

One feasible method to probe the phase diagram of QCD is to study the collisions of heavy nuclei at ultra-relativistic energies which offer the possibility to artificially create matter under extreme conditions. Different collision energies enable us to test various regions of the phase diagram. While the high-energy runs (at RHIC and LHC) explore the region around $\mu \approx 0$, the lower-energy runs at RHIC and GSI (FAIR) are dedicated to the search for the critical end point. As RHIC launched beam energy scan program to inves-

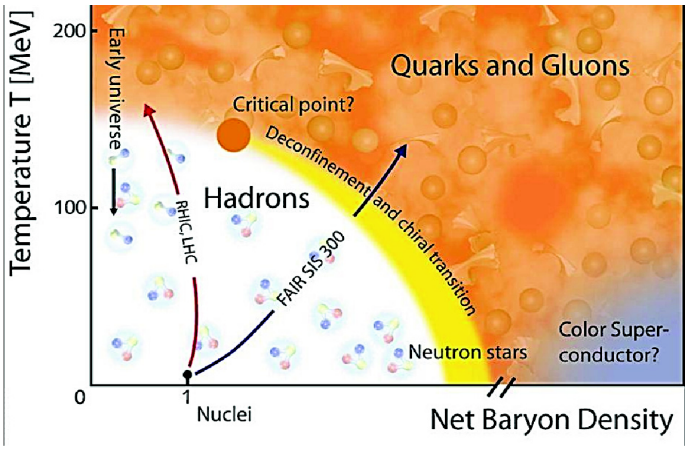

Figure 2.1: A schematic QCD phase diagram in the (T, net baryon density)-plane. Figure taken from [18].

tigate this phase diagram, it is mentioned in both cases. Furthermore, the experimentally collected data allow to draw conclusions about the properties of matter.

Though it is conjectured that already the collision of two nuclei at the center-of-mass energy larger than $\sqrt{s_{NN}} \approx 8$ GeV leads to such a strong heating of matter that colour charges are deconfined, the experimental proof that such a QGP is really created in a heavy-ion collision is extremely challenging since the deconfined phase is supposed to exist only for a very short time of roughly $\Delta t \leq 10$ fm/c, depending on the collision energy. The description of such a collision is based on the assumption that ions are composed of nucleons. Due to the fact that these ions are accelerated to ultra-relativistic velocities, they are Lorentz-contracted, approaching each other along the beam axis (which is normally taken to be the z-axis, see Fig. 2.2) with perpendicular distance between the projectile and the target that is called the impact parameter b. The impact parameter and the direction of the beam axis determine the so-called reaction plane. For $b \geq 0$ fm, some of the nucleons do not participate in the collision. They are called spectators and leave the reaction zone immediately, in contrast to the participants of the reaction. Series of snapshots of the subsequent collision (which is here assumed to be central, i.e., $b = 0$ fm) is shown in Fig. 2.3.

After the impact, in the early phase of the collision, the matter is in a pre-equilibrium state. When compression is completed, a phase with extremely high temperatures and densities is created. The system rapidly equilibrates, developing a fireball which expands and cools rapidly. As soon as the temperature drops below the phase transition to the deconfined phase, hadrons are created again. Subsequent interactions of those hadrons (in the hadronic phase) will be both elastic and inelastic until chemical freeze-out is reached where inelastic collisions terminate. Chemical freeze-out fixes the abundance ratios of the hadronic species into an equilibrium distribution.

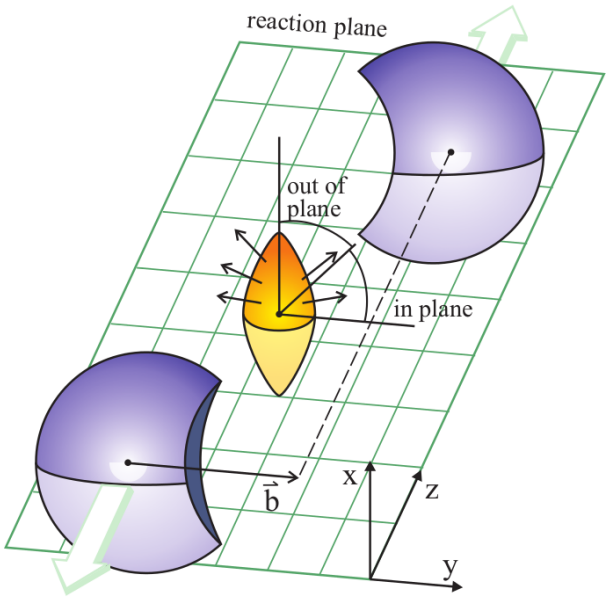

Figure 2.2: Geometry of a heavy-ion collision. The two nuclei move along the beam axis (z-axis) with an impact parameter b, determining the reaction plane. The corresponding definitions of in-plane and out-of-plane are also displayed. Figure taken from [19].

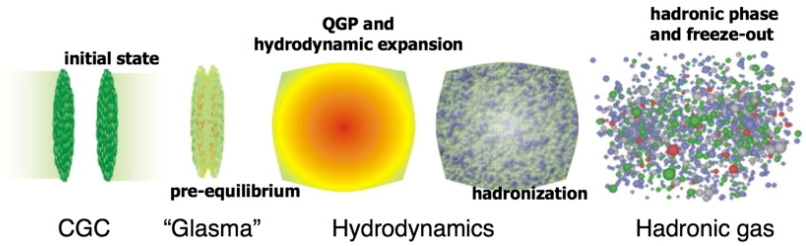

Figure 2.3: Sequence of a heavy-ion collision. The incoming nuclei are Lorentz-contracted since they are accelerated to ultra-relativistic velocities. At the beginning of the collision, a non-equilibrated phase (pre-equilibrium) is created that develops into a thermalized and expanding fireball. During the expansion fireball is cooling until hadrons are formed again (hadronization) which interact unless the system is too dilute. Figure taken from [20].

The expanding system becomes more and more dilute so that finally, at the kinetic freeze-out, all further interactions have ceased. The created hadrons and/or their daughter particles will finally reach the detectors. Hadrons are always created in a heavy-ion collision, independent of QGP formation. Thus, the only way to prove the existence of a QGP experimentally, via a heavy-ion collision, is to analyze the particle distributions at the end of the collision and to compare them to theoretical predictions assuming the creation of a deconfined phase. Therefore, it is extremely important to identify robust critera to distinguish QGP from a hot and dense hadron gas.

2.2 Experimental observables and signatures for the QGP

One of the main challenges of heavy-ion collision experiments is the identification and examining properties of the QGP. Since the QGP can not be studied directly, theoretical models have to predict which properties of the final state of the interactions could provide information about the QGP formation. That is, they have to predict which properties are expected to be different in colliding systems where the QGP is or is not produced. These properties have then to be experimentally investigated (signature of the QGP). Depending on the phase of the collision when they are produced, these signatures can be classified as hard probes or soft probes. Hard probes are signals produced in the first stages of the collision by the interaction of high momentum partons (production of heavy flavour quarks and their bound states, jet quenching). Soft probes correspond to signals produced in the later stages of the collision (spectra of hadrons, anisotropy, fluctuations, femtoscopy, thermal photons and dileptons). Even if they are produced during the hadronization stage, they keep indirect information on the properties of the phase transition and on the QGP formation. Some of the mentioned signatures will be reviewed.

2.2.1 Charged-particle multiplicity density

The first step in characterizing the system produced in A-A collisions is the measurement of the charged particle pseudorapidity density. It constrains the dominant particle production mechanisms and is essential to estimate the initial energy density. The dependence of the charged-particle multiplicity density on energy and system size reflects the interplay between parton-parton scattering processes and soft processes for particle production and may provide information on the partonic structure of the projectiles. Figure 2.4 shows the charged particle multiplicity at mid-rapidity as a function of energy for pp and A+A collisions. For A+A systems it is divided by the number of participant pairs in order to be able to compare between different collision systems including pp. The observed trend from lower energies fits with the LHC data, and generally there is higher multiplicity in A+A collisions than in pp. The charged particle multiplicity per participant pair has doubled in going from RHIC to LHC.

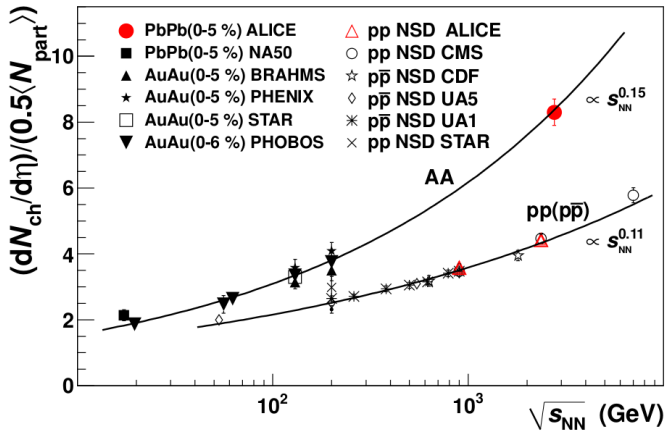

Figure 2.4: Charged particle multiplicity at mid-rapidity scaled to the number of participant pairs at different energies and for different collision systems. The LHC data fit into the trend from lower energies well [21].

2.2.2 Jets and high p_T suppression

A jet is a shower of highly correlated hadrons produced by the hadronization of a hard quark or gluon. Due to momentum conservation, jets are always produced back-to-back, i.e., separated by an angle of π in the azimuthal plane. When the parton pair is created close to the medium surface, one parton can leave the expanding fireball without any further interaction while its partner parton traverses the medium depositing energy and momentum. It was calculated that the energy loss of partons in QGP is much higher than that in hadronic matter [22]. In the most general case, the total energy loss of a highly energetic parton traversing a medium is the sum of collisional and radiative terms: $\Delta E = \Delta E_{coll} + \Delta E_{rad}$. Depending on the kinematic region, a (colour) charge can lose energy in a medium with temperature T mainly by two mechanisms, one of them is collisional energy loss through elastic scatterings with the medium constituents. It dominates at low particle momentum. The second one is radiative energy loss through inelastic scatterings within the medium, it dominates at higher momenta. This phenomenon leads to the jet quenching [23, 24], which is defined as the suppression of high-p_T hadron yields in nucleus-nucleus (e.g. Au-Au or Pb-Pb) collisions relative to that in pp collisions scaled by the number of elementary nucleon-nucleon collisions. The observable used to measure such an effect is called the nuclear modification factor (R_{AA}) and is defined as

$$R_{AA} = \frac{d^2N_{AA}/(dp_T dy)}{T_{AA} d\sigma_{NN}/(dp_T dy)}, \tag{2.2.1}$$

where $T_{AA} = \langle N_{coll} \rangle / \sigma_{NN}$ is the nuclear overlap function and σ_{NN} is the nucleon-nucleon cross section.

Figure 2.5 shows the nuclear modification factor R_{AA} of charged hadrons for central Pb-Pb collisions at ALICE compared to that from the PHENIX and STAR experiments at RHIC. In central collisions at the LHC, R_{AA} exhibits very strong suppression, reaching a minimum of ≈0.14 at p_t = 6-7 GeV. Despite the much flatter p_t spectrum in pp collisions at the LHC, the nuclear modification factor at p_T= 6-7 GeV is smaller than at RHIC. This

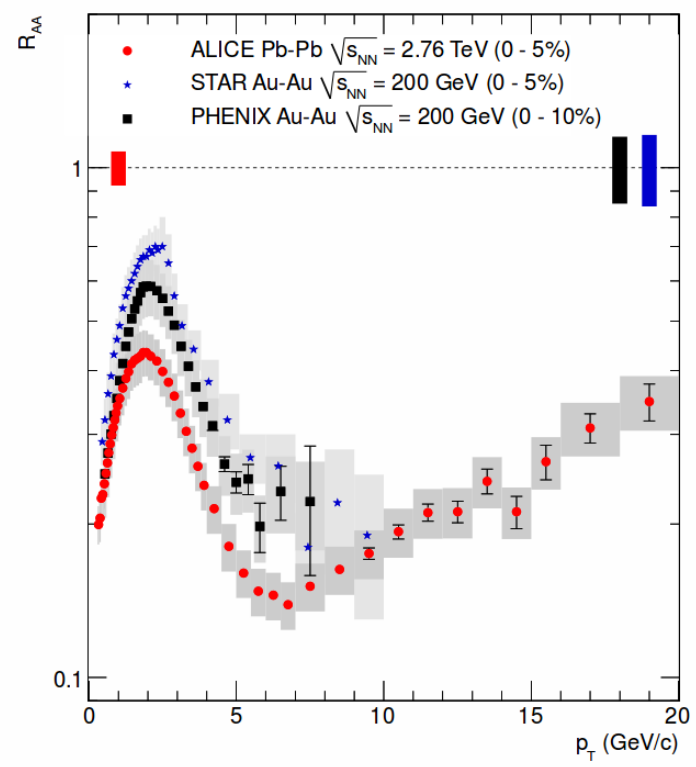

Figure 2.5: Comparison of R_{AA} for charged hadrons in central Pb–Pb collisions at the LHC to measurements at $\sqrt{s_{NN}} = 200$ GeV by the PHENIX [25] and STAR [26] experiments at RHIC. Error bars of the ALICE data indicate the statistical uncertainties. The boxes contain the systematic errors in the data and the p_T dependent systematic errors on the pp reference, added in quadrature. The statistical and systematic errors of the PHENIX data are shown as error bars and boxes, respectively. The statistical and systematic errors of the STAR data are combined and shown as boxes. The vertical bars around $R_{AA} = 1$ indicate the p_T independent scaling errors on R_{AA}. Figure taken from [27].

suggests an enhanced energy loss at LHC and therefore a denser medium. A significant rise by about a factor of two is observed for $7 < p_T < 20$ GeV. This pattern is very intriguing, because it suggests that very high momentum partons may lose only a small fraction of their energy in the medium and, thus, be sensitive probes of its properties.

In order to investigate potential cold nuclear effects in the initial state, p-Pb or d+Au collisions are measured. The LHC p-Pb results can provide valuable information on the elastic, inelastic and coherent multiple parton scattering processes inside a large nucleus. Data from p–Pb are important also to provide constraints to different theoretical models. The measurement of the nuclear modification factor R_{pPb} for charged particles at $|\eta_{CMS}| < 0.3$, is shown in Fig. 2.6. It compares measurement of the nuclear modification factor in p–Pb [28] to that in central (0–5 % centrality) and peripheral (70–80 % centrality) Pb–Pb collisions at $\sqrt{s_{NN}}$=2.76 TeV [33]. The uncertainties of the p–Pb and pp spectra are added in quadrature, separately for the statistical and systematic uncertainties. Modification factor R_{pPb} corresponds to unity for $p_T > 2$ GeV, it shows that the strong suppression observed in central Pb-Pb collisions at LHC [27] is not due to initial state, but rather an

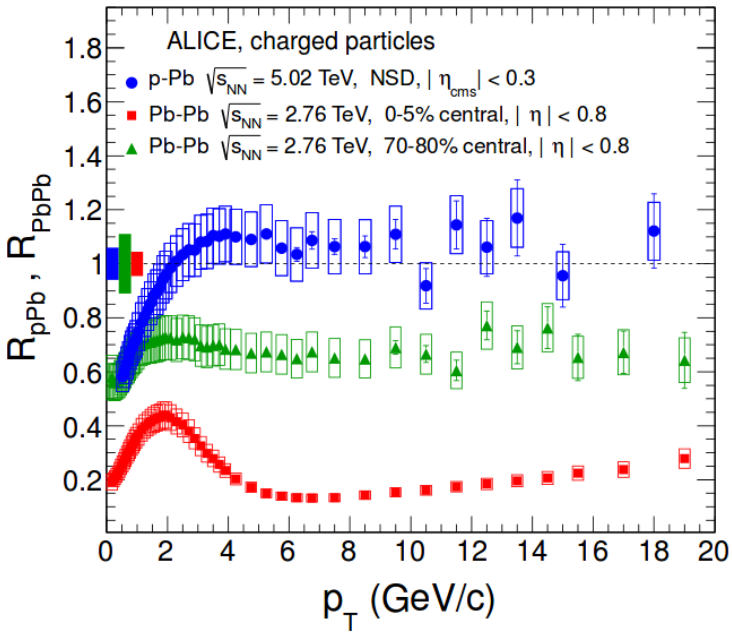

Figure 2.6: The nuclear modification factor of charged particles as a function of transverse momentum in non-single-diffractive p–Pb collisions at $\sqrt{s_{NN}}$= 5.02 TeV. The data for $|\eta_{cms}| < 0.3$ are compared to measurements [33] in central (0–5% centrality) and peripheral (70–80%) Pb–Pb collisions at $\sqrt{s_{NN}}$=2.76 TeV. The statistical errors are represented by vertical bars, the systematic errors by (filled) boxes around data points. The relative systematic uncertainties on the normalization are shown as boxes around unity near p_T=0 for p–Pb (left box), peripheral Pb–Pb (middle box) and central Pb-Pb (right box). Figure taken from [28].

evidence of the hot matter created in collisions of heavy ions. The so-called Cronin effect [29], namely a nuclear modification factor above unity at intermediate p_T, was observed at lower energies in proton–nucleus collisions. In d–Au collisions at $\sqrt{s_{NN}}$=200 GeV, R_{dAu} reached values of about 1.4 for charged hadrons in the p_T range from 3 to 5 GeV/c [30]. The present measurement clearly indicates a smaller magnitude of the Cronin effect at the LHC, the data are even consistent with no enhancement within systematic uncertainties. For directly emitted photons we observe no suppression, it indicates that suppression is in fact a QCD phenomenon, and not electromagnetic in origin [31].

Figure 2.7 compares the ALICE jet measurement [32] to the nuclear modification factor for charged hadrons measured by ALICE [33] and CMS [34] and to the calorimetric jet measurements by ATLAS [35]. Comparing the R_{CP} of jets to charged particles in Fig. 2.7, one would expect the suppression for jets to be smaller than for hadrons, since jet reconstruction collects multiple jet fragments into the jet cone, thus recovering some of the medium-induced fragmentation. However, it can be seen that the R_{CP} for jets is similar to that observed for single hadrons over a broad momentum range. This indicates that the momentum is redistributed to angles larger than R=0.3 by interactions with the medium. Such a strong redistribution of momentum might also be expected to lead to a significant broadening of the energy profile within the larger cone radius R =0.3. The

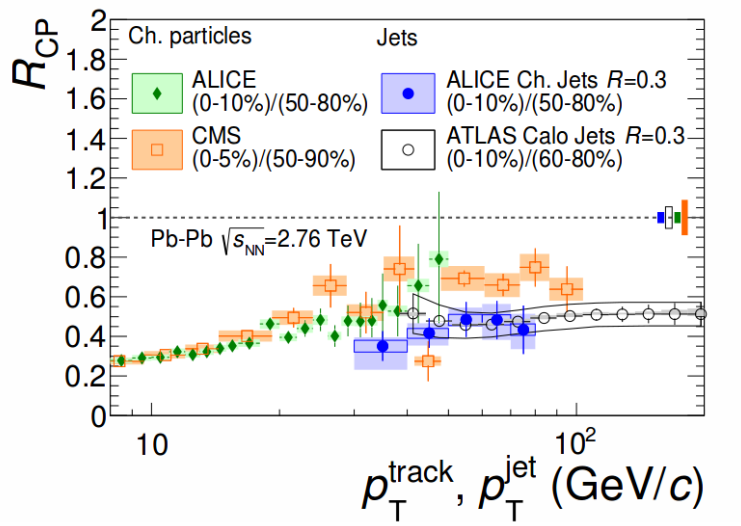

Figure 2.7: Nuclear modification factor of central collisions compared to peripheral ones, for charged jets, fully reconstructed jets and charged hadrons, versus the corresponding transverse momentum of the jet or hadron. Figure taken from [32].

results presented in Fig. 2.8, however, show that the ratio of yields for jets with R =0.2 and R =0.3 is similar in PYTHIA [36] pp simulation and Pb–Pb collisions, indicating that the energy profile of the found jets is not significantly modified. Also the comparison of the measured ratio to the ratio obtained with PYTHIA simulations shows that the transverse jet shape in central and peripheral Pb–Pb collisions are consistent with jet shapes in vacuum. No sign of a modified jet structure is observed between radii of 0.2 and 0.3 within uncertainties.

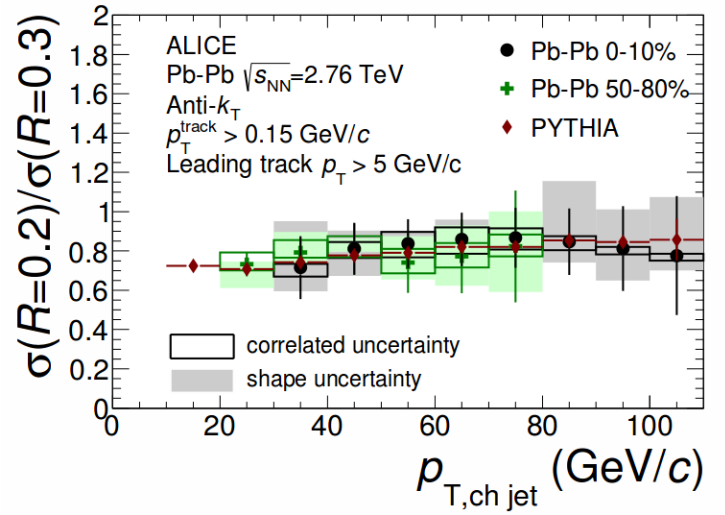

Figure 2.8: Ratio of spectra of charged jets defined with reconstruction parameter R =0.2 and R=0.3, versus charged jet transverse momentum. Figure taken from [32].

2.2.3 Quarkonium suppression

Heavy quarkonia are $c\bar{c}$ (charmonium) or $b\bar{b}$ (bottomonium) bound states. As c and b quarks are not present in the initial flavour content of the colliding nuclei, they must all be produced in pairs at the moment of the fireball creation. Due to their large mass, only in the initial phase of the collision the energy density is high enough to produce those partons abundantly. In the QGP, the distance at which the partons feel interaction with each other, becomes very small due to Debye screening; and the two heavy quarks do not form a bound state. Since the amount of heavy quarks in the fireball is small, the probabilities for the two partons to meet another heavy quark to combine with at the hadronization are small also, so that they will finally build up two hadrons each of them with only one heavy quark. These hadrons are called open-charm and open-beauty hadrons. This means that the quarkonium states will be suppressed in heavy ion collisions, with respect to pp collisions, if a QGP is formed.

Figure 2.9 shows the J/Ψ nuclear modification factor measured at ALICE for Pb-Pb collisions at $\sqrt{s_{NN}} = 2.76$ TeV [37] compared to PHENIX results in Au-Au collisions at $\sqrt{s_{NN}} = 200$ GeV [38]. A rather small J/Ψ suppression of about 0.5 was observed, practically independent of centrality: this is a smaller suppression than that observed at RHIC. The above results hint at J/Ψ regeneration in hot matter at the LHC energies, but it is worth noting that the J/Ψ production can be modified by the initial state effect which could modify the medium. For $\langle N_{part} \rangle$ larger than 70, corresponding to the 50% most central Pb–Pb collisions, the $J/\Psi R_{AA}$ is consistent with a constant within uncertainties. Such behavior was not observed in heavy ion collisions at lower energies (SPS, RHIC) where R_{AA} is continuously decreasing as a function of centrality.

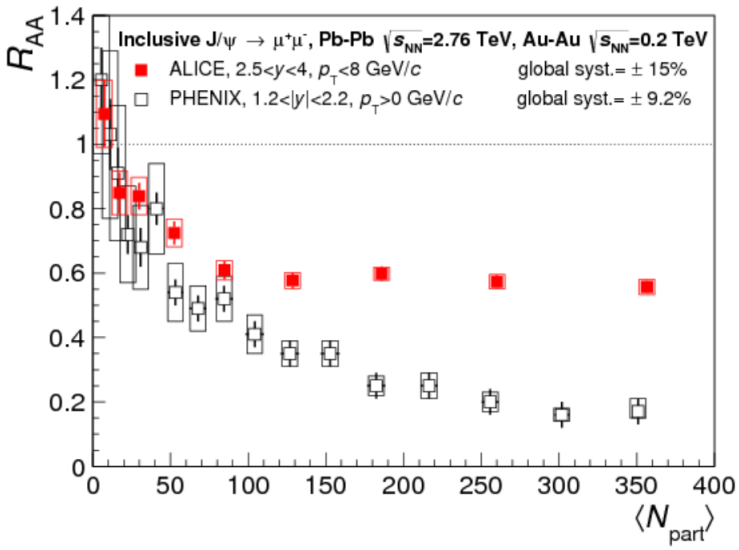

Figure 2.9: Inclusive R_{AA} of J/Ψ as a function of the number of participant nucleons measured in Pb-Pb collisions at $\sqrt{s_{NN}} = 2.76$ TeV [37], compared to the PHENIX measurement in Au-Au collisions at $\sqrt{s_{NN}} = 200$ GeV [38]. Figure taken from [37].

At LHC, measurement of upsilons is also feasible thanks to more energy available.

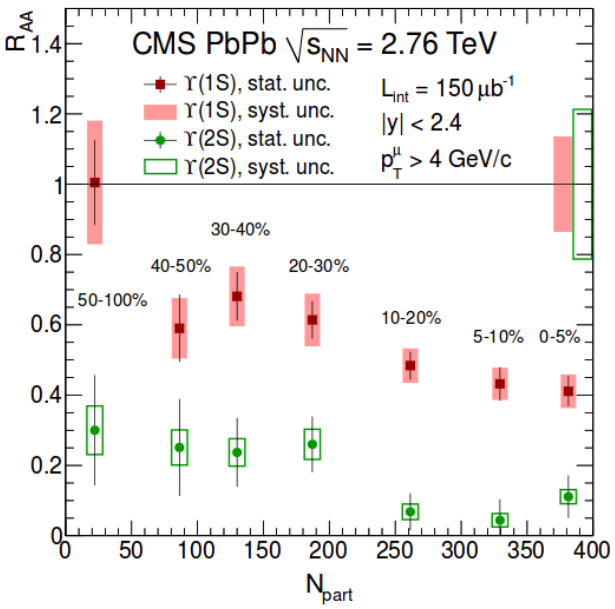

Figure 2.10: Nuclear modification factor R_{AA} for bottomonium states versus centrality. Figure taken from [40].

The nuclear modification factor R_{AA} of upsilons as a function of centrality (number of participating nucleons) is shown in Fig. 2.10. A strong suppression, increasing with centrality, is seen, in particular for the relatively less less bound 2S state. Such a behaviour is consistent with the observation of the sequential suppression of the quarkonium states according to their binding energy [39]. One should note that a significant fraction of measured $\Upsilon(1S)$ states comes from the decay of higher mass bottomonium resonances so that a large fraction of the observed 1S suppression is connected to such feed-down effects. The contribution of regeneration effects is expected to be much smaller in the bottomonium sector, due to the lower $b\bar{b}$ yields compared to charm. Hence, upsilons are more suppressed than J/Ψ particles.

2.2.4 Anisotropic flow

Study of anisotropic flow of particles produced in relativistic heavy-ion collisions [41] has emerged as an important tool to probe the early history, especially the thermalization of the dense fireball produced in these collisions. "Flow" is caused by anisotropic expansion of the fireball. Anisotropic flow means that the azimuthal distribution of particles is not flat. In general, these anisotropies are studied in terms of Fourier decomposition [42]

$$E\frac{d^3N}{d\mathbf{p}} = \frac{1}{2\pi}\frac{d^2N}{p_t dp_t dy}\left(1 + 2\sum_{n=1}^{+\infty} v_n \cos[n(\phi - \Psi_r)]\right), \tag{2.2.2}$$

where E is the energy of the particle, $\mathbf{p}$ the momentum, p_t the transverse momentum, ϕ the azimuthal angle, y the rapidity, and Ψ_r the n-th harmonics reaction plane angle.

The Fourier coefficients are p_t and y dependent and are given by

$$v_n(p_t, y) = \langle \cos[n(\phi - \Psi_r)] \rangle, \tag{2.2.3}$$

where the angular brackets denote an average over the particles, in the (p_t, y) bin under study. In this Fourier decomposition, the coefficients v_1, v_2, v_3 and v_4 are known as directed, elliptic, triangular and quadrangular flow, respectively. The origin of the triangular flow and higher odd harmonics is fluctuation of initial conditions [43]. However, this work aims to consider different source of fluctuations. In particular, v_3 vanishes, if the system starts in non-central collisions with a smooth almond-shaped initial state [43]. But if we take into account initial state fluctuations, the odd harmonics do not vanish for single event. If particle distributions are summed up over a large number of events odd harmonics again vanish. Investigation of the relation between initial geometry and higher harmonics has been also carried out in [44, 45, 46, 47]. Due to fluctuations in the initial state densities, the exact shape of the interaction region in a heavy-ion collision varies event-by-event. The consequence would be that for any centrality, in addition to ellipticity, the shape would also have higher order deviations producing higher harmonics in the decomposition of the azimuthal asymmetry. For more quantitative analyses, however, contributions of final state interactions should be evaluated. The experimental methods for determination of the reaction plane and anisotropic flow coefficients is given in Chapter 8.

The measurement of v_3, combined with other harmonics can give a constraint on the η/s ratio which is a quantity of highest interest. Appropriate models implicitly assume that the equilibration time is below 1 fm/c [48, 49].

The observation of scaling of the elliptic flow per constituent quark versus the transverse kinetic energy per constituent quark (elliptic flow per quark) at RHIC [50, 51] is another experimental fact thought to point to a collective pre-hadronization stage of the evolution of the heavy-ion collision. The main idea is that when the deconfined medium is thermalised, the flow of all constituent partons should be the same. Then, if a significantly large portion of the final state hadrons is produced through the mechanism of parton coalescence [52, 53] the flow per quark would scale with the momentum per constituent quark. This simple coalescence picture does not account for the mass dependence of flow due to the radial expansion of the medium. The transverse kinetic energy per quark is proposed as a scaling variable instead of to account for this [50].

The scaling property of v_2, i.e. v_2/n_q is plotted as a function of p_T/n_q in Fig. 2.11 for various particle species and centrality intervals for ALICE [54]. In the so-called intermediate transverse momentum region (i.e. $2 - 3 < p_T < 5 - 6$ GeV or for $p_T/n_q > 1$ GeV), where the coalescence mechanism is argued to be dominant, the experimental data indicate that the scaling is only approximate in contrast to RHIC. The magnitude of the observed deviations seems to be similar for all centrality intervals.

2.2.5 Flow fluctuations and non-flow correlations

The effects known as flow fluctuations and non-flow correlations bias the measured flow values. That is why we have to take them into account. There are several sources of

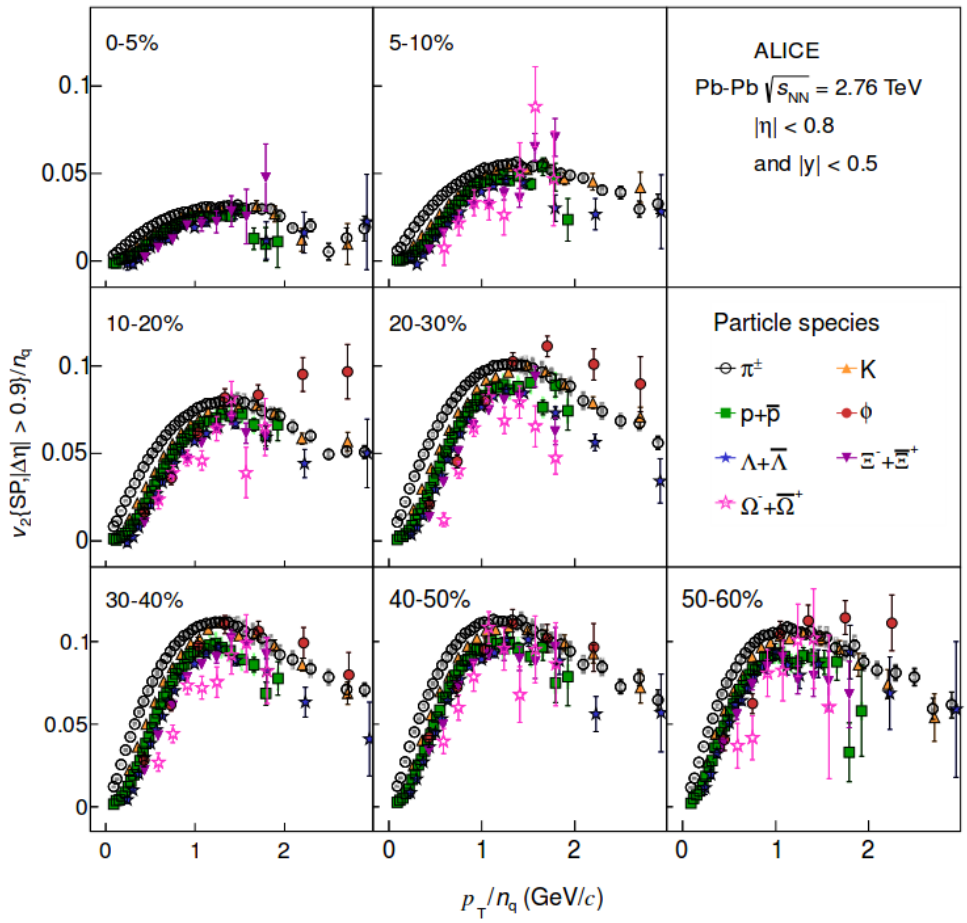

Figure 2.11: The p_T/n_q dependence of v_2/n_q for $\pi^{\pm}, K, p+\bar{p}, \phi, \Lambda+\bar{\Lambda}, \Xi^- + \bar{\Xi}^+$ and $\Omega+\bar{\Omega}^+$ for Pb-Pb collisions in various centrality intervals at $\sqrt{s_{NN}} = 2.76$TeV [54].

flow fluctuations. One of them is if the centrality binning is too coarse. In this case, events with different flow are analysed together and when averaged to extract the actual value there may be influences due to the centrality dependence of flow. Another cause are fluctuations of the initial geometry, such as those that create the odd flow harmonics [55]. Different flow analysis methods respond differently to fluctuations. In general two particle correlation measurements overestimate the flow when the fluctuations are present. On the other hand, multi-particle correlations underestimate the flow when the fluctuations are present [56].

"Non-flow correlations" is the name for azimuthal correlations which look like flow but are caused by diferent mechanisms. There are several sources of non-flow contribution. One source of non-flow are resonance decays such as $\Delta \to p\pi$ or $\rho \to \pi\pi$. In these cases the decay products are highly correlated due to momentum conservation. The Hanbury-Brown-Twiss effect is also known to cause correlations which can contribute to elliptic flow measurements. Finally, jets create many particles that are highly correlated in a back-to-back structure.

Chapter 3

Goals and motivation

As mentioned before, fluctuations in initial conditions introduce higher order flow coefficients that have been observed in RHIC and LHC experiments. Fluctuations in initial energy density distribution are of quantum origin. This is in addition to any geometrical anisotropies which are due to non-zero impact parameter in the collision.

In non-central collisions, pressure gradients within the excited matter are larger in the direction of the impact parameter, which is usually called the in-plane direction. The other transverse direction is denoted as out of plane. The anisotropic pressure gradients lead to different accelerations of the collective flow in the different directions. The fireball then finally expands faster in the in-plane direction. Therefore, more hadrons are emitted in this direction and their transverse momentum spectra are flatter than in the out-of-plane direction. The evolution from such an initial state is reasonably well described by hydrodynamic models. This is the point where the Equation of State (EoS) and transport coefficients enter simulations. The resulting freeze-out state depends on EoS and transport properties. Thus by calculating hadronic spectra and their anisotropy one hopes to be able to tune parameters in hydrodynamic simulations until an agreement with data is reached. However, initial conditions can only be determined in framework of various models. Unfortunately, the resulting anisotropies of the hadron distributions are strongly model-dependent [57]. Thus, without the exact knowledge of the initial conditions the extraction of transport coefficients seems difficult. Recent calculations suggest that final fluctuations depend linearly on fluctuations in initial conditions [45].

Furthermore, usually, it is assumed that there is no contribution to fluctuations during the hydrodynamic evolution. However, it can be wrong assumption. Hydrodynamic simulations with the fluid energy and momentum density coupled to dynamically fluctuating order parameter field show fluctuations in the evolving energy density which can well cause flow anisotropies observable in data [58].

More precise quantitative impact of such a mechanism remains to be studied. The aim of this thesis is to introduce another mechanism that can induce flow anisotropies during the hydrodynamic evolution, simulate this scenario by means of three-dimensional hydrodynamics and estimate its contribution to anisotropic flow.

Hard partons from initial scatterings do not thermalise immediately as they are pro-

duced, but interact with the hot and dense quark-gluon plasma. There, they are mostly fully quenched so that their momentum is transferred into the fluid. Momentum must be conserved and thus the momentum of the hard parton must be transformed into momentum of a stream of matter within the wake behind the parton. This will show up in the flow pattern. What would be the result of many such streams, if they all are initiated in the fireball? The energy in a collision at the LHC is so large that there may be pairs of hard partons which are close in rapidity and are directed so that they might come close to each other during the evolution of the collision. Some of the streams which they induce could merge and either cancel or flow in a new direction so that energy and momentum are conserved, see Fig. 3.1. Original hard partons are produced with no preferred transverse direction. The first expectation would be that the large number of fluid streams they initiate cancel out in some way and in the end there remains just thermalized matter with some energy density and no macroscopic flow. However, in non-central collisions the argument might not be so straightforward. The streams have random directions, but

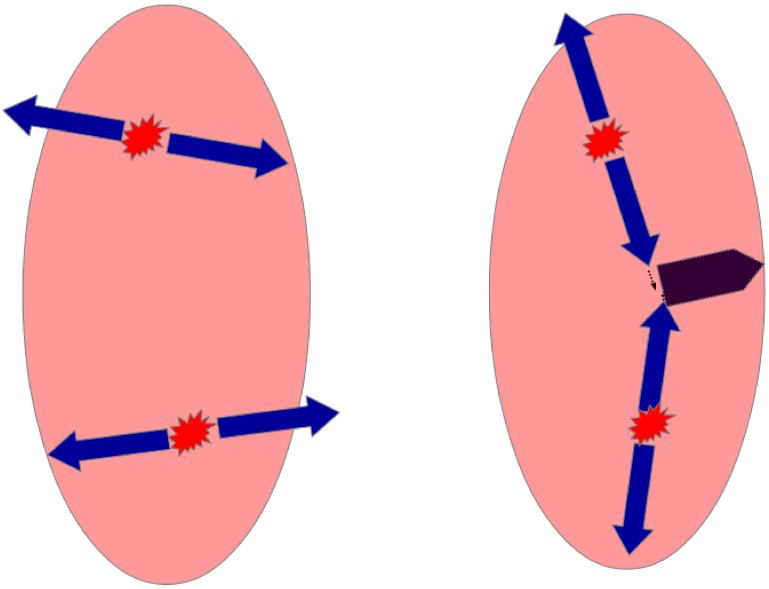

Figure 3.1: Transverse cross-section through the fireball with two dijet pairs produced. Reaction plane is horizontal. Left: two dijets both emitted in the direction of the reaction plane both contribute positively to the elliptic flow, which is dominant in the same direction. Right: if hard partons are produced off the reaction plane, some of their streams can come together and merge.

their spatial distribution is not isotropic, since it is given by the initial collision geometry. In the out-of-plane direction the fireball is narrower. Thus, there is a good chance that two streams having finite width and flowing in the out-of-plane direction will meet. On the other hand, streams could more easily pass each other without interacting when produced in the in-plane direction. Thus, streams perpendicular to the reaction plane are more likely to cancel each other, while those flowing in directions parallel to the reaction plane survive. Moreover, if hard partons are even fully quenched before they could

actually meet, their momentum has been shown to be further carried by the generated streams in the fluid [59].

As a result, the anisotropy of the flow of bulk matter receives some feeding from hard partons and this feeding exhibits signs of positive elliptic flow. The novelty of this proposal consists in accounting for the possibility of interactions between streams generated in the bulk. The proper way to do so is the use of a hydrodynamic simulation with included energy and momentum deposition from hard partons into the bulk. The way of implementation and results of hydrodynamic simulations will be described in following Chapters.

Chapter 4

Hydrodynamics and its application

Relativistic hydrodynamics is helpful tool because of its simplicity and generality. It is simple because the information about the system is described in terms of its thermodynamic properties, e.g., its Equation of State (hereinafter EoS). This is the point where hydrodynamics is connected with lattice QCD calculations which provide the EoS. Hydrodynamics relies on only one assumption, unfortunately a very strong one: local thermodynamic equilibrium. How does it happen is not known yet. No other assumption is made concerning the nature of the particles and fields, their interactions, the classical/quantum nature of the phenomena involved.

Hydrodynamics is applicable when the mean free path of the particles is much smaller than the typical scale of the fireball on which its properties are changing; and allows for a description of the system in terms of macroscopic quantities.

The present understanding of heavy-ion collisions strongly suggests that a multi-module modeling is indispensable for the description of the entire history of heavy-ion collisions. Knowledge of dominant physics at each stage has been accumulated, but a comprehensive model is still missing. For the construction of such a multi-module model, hydrodynamic models are a promising starting point, because at present they are considered as one of the most reliable and successful dynamical models for understanding of experimental data at RHIC and LHC comprehensively, especially for the description of the QGP phase. At the same time, it is easy to implement the latest developments in the physics of heavy-ion collisions such as fluctuating initial conditions, the lattice QCD inspired equation of state, recombination mechanism for hadronization, and final state interactions in freeze-out processes into a hydrodynamic model.

4.1 Ideal relativistic hydrodynamics

Any system can be described by symmetric energy-momentum tensor $T^{\mu\nu}$ which describes not only the distribution of energy and momentum in the system. It also provides information about the flow of these quantities. In a given reference frame the time-time component T^{tt} is the energy density, the time-space component $T^{it} = T^{ti}$ is the i'th component of the momentum density, and the space-space component T^{ik} is the flux of i'th

component of the momentum across the surface perpendicular to x^k. Tensor of energy and momentum of ideal relativistic fluid (i.e. without dissipation) takes the form

$$T^{\mu\nu} = (\epsilon + p)u^\mu u^\nu - pg^{\mu\nu} = \epsilon u^\mu u^\nu - p\Delta^{\mu\nu}, \tag{4.1.1}$$

where ϵ and p are energy density and pressure in the local rest frame of the fluid and

$$\Delta^{\mu\nu} = g^{\mu\nu} - u^\mu u^\nu \tag{4.1.2}$$

is the projection operator on the space orthogonal to the fluid velocity. It has the properties $\Delta^{\mu\nu}u_\mu = \Delta^{\mu\nu}u_\nu = 0$ and $\Delta^{\mu\nu}\Delta^\alpha_\mu = \Delta^{\nu\alpha}$. If there are no external forces, the energy-momentum tensor is conserved

$$\partial_\mu T^{\mu\nu} = 0 \tag{4.1.3}$$

and so is the local charge

$$\partial_\mu N^\mu = \partial_\mu n u^\mu = 0, \tag{4.1.4}$$

where n is charge density in the local rest frame of the fluid, $u^\mu = \gamma(1, \vec{v})$ is the fluid four-velocity ($\gamma = (1 - \vec{v}^2)^{-\frac{1}{2}}, \vec{v}$ is the fluid three-velocity), and $g^{\mu\nu}$ =diag$(+1, -1, -1, -1)$ is the metric tensor. If the source current term describing deposition (extraction) of energy and/or momentum J^ν is present then conservation of energy and momentum is expressed as

$$\partial_\mu T^{\mu\nu} = J^\nu. \tag{4.1.5}$$

The equation (4.1.5) can be rewritten in the useful way:

$$\partial_t T^{tt} + \partial_x T^{xt} + \partial_y T^{yt} + \partial_z T^{zt} = J^t, \tag{4.1.6}$$
$$\partial_t T^{tx} + \partial_x T^{xx} + \partial_y T^{yx} + \partial_z T^{zx} = J^x, \tag{4.1.7}$$
$$\partial_t T^{ty} + \partial_x T^{xy} + \partial_y T^{yy} + \partial_z T^{zy} = J^y, \tag{4.1.8}$$
$$\partial_t T^{tz} + \partial_x T^{xz} + \partial_y T^{yz} + \partial_z T^{zz} = J^z. \tag{4.1.9}$$

There are 5 unknown quantities: p, ϵ and three-velocity but we have only four equations. These equations of ideal fluid-dynamics are closed by specifying the EoS. Equation of State connects pressure with energy and charge density in the form $p = p(\epsilon, n)$. For heavy-ion collisions, the conserved charge is for example (net) baryon number. There is an equation of the type (4.1.4) for every conserved charge.

The equations of ideal (relativistic) hydrodynamics emerge from the conservation equations (4.1.4) and (4.1.5). It is very useful to project these equations in the direction parallell ($u_\nu \partial_\mu T^{\mu\nu}$) and perpendicular ($\Delta^\alpha_\nu \partial_\mu T^{\mu\nu}$) to the fluid velocity. For the first projection, one finds

$$\begin{aligned} u_\nu \partial_\mu T^{\mu\nu} &= u^\mu \partial_\mu \epsilon + \epsilon(u_\nu u^\mu) + \epsilon u_\nu u^\mu \partial_\mu u^\nu - p u_\nu \partial_\mu \Delta^{\mu\nu} \\ &= (\epsilon + p)\partial_\mu u^\mu + u^\mu \partial_\mu \epsilon = u_\mu J^\mu. \end{aligned} \tag{4.1.10}$$

For the other projection one finds

$$\begin{aligned} \Delta^\alpha_\nu \partial_\mu T^{\mu\nu} &= \epsilon u^\mu \Delta^\alpha_\mu \partial_\mu u^\nu - \Delta^{\mu\alpha}(\partial_\mu p) + p u^\mu \Delta^\alpha_\mu \partial_\mu u^\nu \\ &= (\epsilon + p) u^\mu \partial_\mu u^\alpha - \Delta^{\mu\alpha}\partial_\mu p = \Delta^\alpha_\mu J^\mu. \end{aligned} \tag{4.1.11}$$

Introducing the shorthand notations

$$D \equiv u^\mu \partial_\mu, \tag{4.1.12}$$
$$\nabla^\alpha \equiv \Delta^\alpha_\mu \partial^\mu \tag{4.1.13}$$

for the projection of derivatives parallel and perpendicular to u^μ, equations (4.1.10) and (4.1.11) can be simplified to

$$D\epsilon + (\epsilon + p)\partial_\mu u^\mu = u_\mu J^\mu, \tag{4.1.14}$$
$$(\epsilon + p)Du^\alpha - \nabla^\alpha p = \Delta^\alpha_\mu J^\mu. \tag{4.1.15}$$

For the numerical implementation of relativistic ideal hydrodynamics it is convenient to consider the energy density in the calculational frame

$$E \equiv T^{tt} = (\epsilon + p\vec{u}^2)\gamma^2, \tag{4.1.16}$$

the momentum density

$$M^i \equiv T^{ti} = (\epsilon + p)\gamma^2 v^i, \tag{4.1.17}$$

and the charge density

$$R \equiv N^t = \gamma n. \tag{4.1.18}$$

Using them, the equations of motion (4.1.4), (4.1.5) then take the form

$$\partial_t E + \nabla \cdot (E\vec{v}) + \nabla \cdot (p\vec{v}) = J^t, \tag{4.1.19}$$
$$\partial_t \vec{M} + \nabla \cdot (\vec{M}\vec{v}) + \nabla p = \vec{J}, \tag{4.1.20}$$
$$\partial_t R + \nabla \cdot (R\vec{v}) = 0. \tag{4.1.21}$$

The proper energy density ϵ is calculated from the relation $\epsilon = E - Mv$, where v is the magnitude of velocity three-vector and M is the magnitude of momentum density three-vector. The pressure p is inferred from the EoS employed. The four-velocity $u^\mu = \gamma(1, \vec{v})$ can be computed from three-velocity components. Detailed description of this process is given in Chapter 4.3.

Although the ideal relativistic hydrodynamics was used throughout this work, relativistic viscous hydrodynamics introduced in the next section is presented for summary purposes as state-of-the-art.

4.2 Relativistic viscous hydrodynamics

One of the main exciting discoveries at RHIC was the fact that the medium created during a heavy-ion collision behaves like a "nearly perfect fluid" [60, 61, 62, 63, 64]. This implies that dissipative effects have to be small, but we do not know exactly how "small" they are. This issue cannot be answered using ideal hydrodynamics. Therefore, dissipative quantities have to be included into the description of heavy-ion collisions in order to obtain the correct qualitative understanding. It is necessary to apply viscous hydrodynamics for various realistic initial conditions (which are unfortunately not known explicitly for a heavy-ion collision) to confirm the smallness of the dissipative quantities.

Nowadays, we have so detailed measurements of anisotropic flow, that ideal hydrodynamics does not suffice to reproduce all of these data. In current understanding, the most realistic hydrodynamic model should have the following features: viscosity effects, (3+1)-dimensional space-time expansion, event-by-event fluctuating initial conditions, lattice QCD inspired EoS, and freeze-out process which is described by hadron-based cascade models [65].

Relativistic viscous hydrodynamics describes non-equilibrium processes of the system as corrections to ideal hydrodynamics. When one starts to include the effects of dissipation into relativistic hydrodynamics, one is confronted with rather complicated situation. One of the difficulties is that a naive introduction of viscosities, a first-order theory (i.e., first order in gradients) suffers from acausality. Heat conduction equation allows instantaneous propagation of heat because of its parabolicity. The acausality of first-order hydrodynamics stems from the same reason. In order to avoid this problem, second order terms in gradients of velocities and energy density have to be included in the expression for the entropy [66, 67, 68, 69, 70, 71, 72] but the systematic treatment of these second order terms has not been established yet. Although there is remarkable progress towards the construction of a fully consistent relativistic viscous hydrodynamic theory, there are still ongoing discussions about the formulation of the equations of motion and about the numerical procedures to solve them [73]. The equations of hydrodynamics are then generalized to include dissipative, or viscous, effects.

The basic quantities characterizing dissipative fluids are the net charge current N^μ and the energy-momentum tensor $T^{\mu\nu}$. These can be decomposed with respect to the fluid four-velocity u^μ as [74, 75, 76, 77]:

$$T^{\mu\nu} = T^{\mu\nu}_{ideal} + \delta T^{\mu\nu} = eu^\mu u^\nu - (p + \Pi)\Delta^{\mu\nu} + W^\mu u^\nu + W^\nu u^\mu + \pi^{\mu\nu}, \quad (4.2.1)$$

$$N^\mu = N^\mu_{ideal} + \delta N^\mu = nu^\mu + V^\mu, \quad (4.2.2)$$

where $n = N^\mu u_\mu$ is the net charge density and $e = u_\mu T^{\mu\nu} u_\nu$ is the energy density in the Landau local rest frame, i.e., where $u^\mu = (1, 0, 0, 0)$. The charge diffusion current $\delta N^\mu = V^\mu = N_\nu \Delta^{\mu\nu}$. The energy-momentum flow orthogonal to u^μ is given by $W^\mu = \Delta^{\mu\alpha} T_{\alpha\beta} u^\beta$. This quantity can be written as $W^\mu = q^\mu + (e+p)V^\mu/n$, where q^μ is the heat flow. The local isotropic pressure is denoted by $p + \Pi = -\frac{1}{3}\Delta_{\mu\nu} T^{\mu\nu}$, where p is the equilibrium pressure and Π is the bulk viscous pressure measuring the deviation from the local equilibrium pressure. The shear stress tensor is defined as $\pi^{\mu\nu} = \left[\frac{1}{2}(\Delta^\mu_\alpha \Delta^\nu_\beta + \Delta^\mu_\beta \Delta^\nu_\alpha) - \frac{1}{3}\Delta^{\mu\nu}\Delta_{\alpha\beta}\right] T^{\alpha\beta}$. This representation is completely general, valid in any coordinate system, and independent of the definition of the flow velocity.

When all dissipative quantities are zero, $V^\mu = W^\mu = 0, \Pi = 0, \pi^{\mu\nu} = 0$, the decompositions (4.2.1) and (4.2.2) reduce to perfect fluid form, $N^\mu = N^\mu_{eq} = nu^\mu$ and $T^{\mu\nu} = T^{\mu\nu}_{eq} = \epsilon u^\mu u^\nu - p(\epsilon, n)\Delta^{\mu\nu}$. The local rest frame energy and charge densities are always fixed to their equilibrium values by the Landau matching conditions, i.e., $n = n_{eq}$, and $\epsilon = \epsilon_{eq}$. Then, the equilibrium pressure is given by the EoS $p = p(\epsilon, n) = -\frac{1}{3}\Delta_{\mu\nu} T^{\mu\nu}_{eq}$. The non-equilibrium entropy current can be written as

$$S^\mu = S^\mu_{eq} + \delta S^\mu = su^\mu + \Phi^\mu, \quad (4.2.3)$$

where the entropy flux relative to u^μ is $\Phi^\mu = S_\nu \Delta^{\mu\nu}$. The local rest frame entropy density is $s = S^\mu u_\mu$. The phenomenological extension of the entropy four-current by Israel and Stewart (IS) can be written without heat conductivity as [67, 69, 78, 79]

$$S^\mu = su^\mu = s_{eq}u^\mu - (\beta_0 \Pi^2 + \beta_2 \pi^{\alpha\beta}\pi_{\alpha\beta})\frac{u^\mu}{2T}, \tag{4.2.4}$$

where the coefficients β_0 and β_2 are functions of ϵ and n. Their exact value can be determined explicitly from kinetic theory. The requirement of non-decreasing entropy leads to relaxation equations for the bulk pressure and shear stress tensor. Here are also included the vorticity terms which follow from the kinetic theory derivation, but we neglect the coupling between bulk and shear viscosity. Then, the IS equations [69, 80] can be written as

$$D\Pi = \frac{1}{\tau_\Pi}(\Pi_{NS} - \Pi) - I_0, \tag{4.2.5}$$

$$D\pi^{\mu\nu} = \frac{1}{\tau_\pi}(\pi^{\mu\nu}_{NS} - \pi^{\mu\nu}) - I_1^{\mu\nu} - I_2^{\mu\nu} - I_3^{\mu\nu,}, \tag{4.2.6}$$

where $D = u^\mu \partial_\mu$ is the covariant convective time derivative, $\tau_\Pi = \zeta\beta_0$ denotes the relaxation time of the bulk viscous pressure and $\tau_\pi = 2\eta\beta_2$ is the relaxation time of the shear stress tensor. The relativistic Navier-Stokes values are given by [74, 81]

$$\Pi_{NS} = -\zeta\theta, \tag{4.2.7}$$

$$\pi^{\mu\nu}_{NS} = 2\eta\sigma^{\mu\nu}, \tag{4.2.8}$$

where ζ is the bulk viscosity coefficient and η is the shear viscosity coefficient. The abbreviations are defined as

$$I_0 = \frac{1}{2}\Pi(\nabla_\lambda u^\lambda + D\ln\frac{\beta_0}{T}), \tag{4.2.9}$$

$$I_1^{\mu\nu} = (\pi^{\lambda\mu}u^\nu + \pi^{\lambda\nu}u^\mu)Du_\lambda, \tag{4.2.10}$$

$$I_2^{\mu\nu} = \frac{1}{2}\pi^{\mu\nu}(\nabla_\lambda u^{\lambda + D\ln\frac{\beta_2}{T}}), \tag{4.2.11}$$

$$I_3^{\mu\nu} = \pi^{\mu\lambda}\omega_\lambda^\nu + \pi^{\nu\lambda}\omega_\lambda^\mu, \tag{4.2.12}$$

$$\theta = \partial_\mu u^\mu + \Gamma^\mu_{\alpha\mu}u^\alpha, \tag{4.2.13}$$

$$\sigma^{\mu\nu} = \frac{1}{2}(\partial^\mu u^\nu - u^\mu u^\alpha \partial_\alpha u^\nu + \partial^\nu u^\mu - u^\nu u^\alpha \partial_\alpha u^\mu) + \\ + \frac{1}{2}(\Delta^{\mu\alpha}u^\beta\Gamma^\nu_{\alpha\beta} + \Delta^{\nu\alpha}u^\beta\Gamma^\mu_{\alpha\beta}) - \frac{\theta}{3}\Delta^{\mu\nu}, \tag{4.2.14}$$

$$\omega^\mu_\nu = \frac{1}{2}(\partial_\nu u^\mu - \partial^\mu u_\nu - u^\mu u^\alpha \partial_\alpha u_\nu - u_\nu u^\alpha \partial_\alpha u^\mu), \tag{4.2.15}$$

$$\sigma^{\mu\nu}u_\nu = 0, \tag{4.2.16}$$

$$\omega^{\mu\nu}u_\nu = 0. \tag{4.2.17}$$

If we use non flat space-time metrics, there will rise non-zero Christoffel symbols defined as follows

$$\Gamma^\mu_{\alpha\beta} = \frac{1}{2}g^{\gamma\mu}(\frac{\partial g_{\alpha\gamma}}{\partial x_\beta} + \frac{\partial g_{\beta\gamma}}{\partial x_\alpha} - \frac{\partial g_{\alpha\beta}}{\partial x_\gamma}). \tag{4.2.18}$$

The explicit expressions for the dissipative terms are not unique but depend on considered equations. This ambiguity comes from the choice of local rest frames of the fluid. As stated before we chose the Landau frame which is tied to the energy flow where $W^\mu = q^\mu + (e+p)V^\mu/n = 0$:

$$u^\mu = \frac{T^\mu_\nu u^\nu}{\sqrt{u^\alpha T^\beta_\alpha T_{\beta\gamma} u^\gamma}}. \tag{4.2.19}$$

In addition, there is another choice used to define the flow velocity besides the Landau frame. It is tied to the net charge flow when diffusion current vanishes $V^\mu = 0$ (Eckart frame)

$$u^\mu = \frac{N^\mu_i}{\sqrt{N_i N_i}}. \tag{4.2.20}$$

Without conserved charges only Landau's definition of the flow velocity is appropriate. In this case the heat flow is $q^\mu = -(e+p)V^\mu/n$. For net charge-free matter, q^μ is not well defined, but also irrelevant, so it is set to zero, $q^\mu = V^\mu = 0$.

4.3 Transformation between the Laboratory Frame and the Local Rest Frame

During the numerical solving of the hydrodynamic equations it is necessary to perform transformation from the laboratory frame to the local rest frame to extract the values of velocity v and energy density ϵ. It is essential to perform this transformation to be able to proceed to the next step in hydrodynamic computation. The approach is the following: from the EoS follows $p = p(\epsilon, n)$. The local rest frame variables ϵ, n and the velocity v^i have to be determined from the calculational frame variables E, M^i, N. This requires in general an inversion of the five equations

$$E = (\epsilon + p)\gamma^2 - p, \tag{4.3.1}$$

$$M^i = (\epsilon + p)\gamma^2 v^i, \tag{4.3.2}$$

$$N = n\gamma. \tag{4.3.3}$$

Nevertheless, it is not necessary to perform a five-dimensional root search in ideal hydrodynamics. Note that M^i and v^i point into the same direction. Let $M = \sqrt{\sum_{i=1}^3 T_{\tau i} T^{\tau i}}$ and $v = |\mathbf{v}|$.

Now the relation $M = (E+p)v$ holds in ideal hydrodynamics and also

$$\epsilon = E - Mv, \tag{4.3.4}$$

$$n = N(1-v^2)^{1/2}. \tag{4.3.5}$$

Hence,

$$|v| = \frac{M}{E + p(E - Mv, (1-v^2)^{1/2}N)}. \tag{4.3.6}$$

For given calculational frame quantities $E, T^{\tau i}, N$ this is a simple fixed-point equation for $|v|$ and can be solved iteratively. Once v is known, ϵ and n can be inferred from (4.3.4)

and (4.3.5) and p from the EoS. The different components of v can be obtained from the collinearity of M and v. For a simple EoS, one might even find an analytical solution for v [82].

Much more difficult task is to perform previous calculation in 2nd order viscous hydrodynamics. We can introduce a simplified notation which mimics the perfect fluid relations [83], $N = n\gamma, E = T^{\tau\tau} - \pi^{\tau\tau}, M_i = T^{\tau i} - \pi^{\tau i}$, where $M = |\mathbf{M}| = (M_x^2 + M_y^2 + M_z^2)^{1/2}$. Hence $\mathbf{M}$ is parallel to the velocity $\mathbf{v}$, similarly as in the perfect fluid case. These quantities have to obey the physical constraint $M \leq E$, in order to obtain meaningful solutions. Therefore, we can express the local rest frame charge density, energy density, the absolute magnitude of the velocity, and the velocity components as

$$n = N(1 - v^2)^{1/2} \tag{4.3.7}$$

$$\epsilon = E - \mathbf{vM} \tag{4.3.8}$$

$$v = M/[E + p + \Pi] \tag{4.3.9}$$

$$v_i = vM_i/M. \tag{4.3.10}$$

This set of equations can be solved by using a one-dimensional root search. However, in case of dissipative fluids, ideal fluid computation may not always be possible. This is due to the fact that the vectors $T^{\tau\mu}$ and $\pi^{\tau\mu}$ are not parallel to each other. Hence choosing other shear stress tensor components as independent variables, or in cases which take into account the heat flow, it is required to carry out a multidimensional root search to find the velocity [83, 84, 85, 86]. This procedure is obligatory in both the Cartesian as Milne coordinates described below.

4.4 Milne coordinates

In this section we move from Cartesian coordinate system to coordinate system preferable for expanding system, e.g. Milne coordinates. Milne coordinates are advantegeous for hydrodynamic description of expanding fireball since they are used to treat the predominant expansion in longitudinal (beam) direction effectively so they are the choice for hydrodynamic simulations related to the physics of ultrarelativistic heavy ion collisions. The new coordinates for the $t - z$ plane in spacetime (z being the collision axis) are expressed via coordinate transformation from Minkowski coordinates t, x, y, z as

$$x^\mu = (t, x, y, z) \to \bar{x}^m = (\tau, x, y, \eta), \tag{4.4.1}$$

$$\tau = \sqrt{t^2 - z^2} \qquad \eta = \operatorname{artanh}(z/t) = \frac{1}{2} \ln \left(\frac{t+z}{t-z} \right). \tag{4.4.2}$$

The inverse transformations are defined as

$$t = \tau \cosh \eta \qquad z = \tau \sinh \eta, \tag{4.4.3}$$

while the definitions of x and y coordinates are unchanged. Here η denotes the longitudinal space-time rapidity and τ the proper time. The metric in Milne coordinates follows from

the invariant line element in this coordinate system $ds^2 = g_{\mu\nu}dx^\mu dx^\nu = d\tau^2 - dx^2 - dy^2 - \tau^2 d\eta^2$ to be

$$g_{\mu\nu} = diag(1, -1, -1, -\tau^2). \tag{4.4.4}$$

The only non-vanishing Christoffel symbols in this metric are

$$\Gamma^\eta_{\eta\tau} = \frac{1}{\tau}, \Gamma^\eta_{\tau\eta} = \frac{1}{\tau}, \Gamma^\tau_{\eta\eta} = \tau. \tag{4.4.5}$$

The equation of energy-momentum conservation in this metric is thus in form of

$$\partial_\mu T^{\mu\nu} + \Gamma^\mu_{\mu\alpha} T^{\alpha\nu} + \Gamma^\nu_{\mu\alpha} T^{\mu\alpha} = J^\nu. \tag{4.4.6}$$

Equations of motion in this metric take the form

$$\begin{aligned}
\partial_\tau T^{\tau\tau} + \partial_x T^{\tau x} + \partial_y T^{\tau y} + \partial_\eta T^{\tau\eta} + \frac{1}{\tau} T^{\tau\tau} + \tau T^{\eta\eta} &= J^\tau \\
\partial_\tau T^{\tau x} + \partial_x T^{xx} + \partial_y T^{yx} + \partial_\eta T^{\eta x} + \frac{1}{\tau} T^{\tau x} &= J^x \\
\partial_\tau T^{\tau y} + \partial_x T^{xy} + \partial_y T^{yy} + \partial_\eta T^{\eta y} + \frac{1}{\tau} T^{\tau y} &= J^y \\
\partial_\tau T^{\tau\eta} + \partial_x T^{x\eta} + \partial_y T^{y\eta} + \partial_\eta T^{\eta\eta} + \frac{3}{\tau} T^{\tau\eta} &= J^\eta.
\end{aligned} \tag{4.4.7}$$

For charged currents the equation of motion is following

$$\partial_\tau n + \partial_x (n v_x) + \partial_y (n v_y) + \partial_\eta (n v_\eta) + \frac{1}{\tau} n + \frac{1}{\tau} n v_\eta + \tau n v_\eta = 0. \tag{4.4.8}$$

Again it is necessary to specify EoS to close this set of equations. In Milne coordinates, $T^{\mu\nu}$ and N^ν keep the same structure.

The accurate numerical solution would eventually require to apply a higher order numerical time integration scheme. This can be circumvented by redefining the variables in Milne coordinates as [87]:

$$T^{\mu\nu} = \tilde{T}^{\mu\nu}, \qquad \mu, \nu \neq \eta, \tag{4.4.9}$$

$$T^{\mu\eta} = \tilde{T}^{\mu\eta}/\tau, \qquad \mu \neq \eta, \tag{4.4.10}$$

$$T^{\eta\eta} = \tilde{T}^{\eta\eta}/\tau^2, \tag{4.4.11}$$

$$N^\eta = \tilde{N}^\eta/\tau. \tag{4.4.12}$$

Rewriting the equations for $\tau\tilde{T}^{\mu\nu}$:

$$\begin{aligned}
\tilde{\partial}_\nu(\tau\tilde{T}^{\tau\nu}) + \frac{1}{\tau}(\tau\tilde{T}^{\eta\eta}) &= 0, \\
\tilde{\partial}_\nu(\tau\tilde{T}^{x\nu}) &= 0, \\
\tilde{\partial}_\nu(\tau\tilde{T}^{y\nu}) &= 0, \\
\tilde{\partial}_\nu(\tau\tilde{T}^{\eta\nu}) + \frac{1}{\tau}(\tau\tilde{T}^{\eta\tau}) &= 0, \\
\tilde{\partial}_\nu(\tau\tilde{N}^\nu) &= 0,
\end{aligned} \tag{4.4.13}$$

with

$$\tilde{\partial}_\nu \equiv \{\partial/\partial\tau, \partial/\partial x, \partial/\partial y, (1/\tau)\partial/\partial\eta\}, \tag{4.4.14}$$

all the components of $\tilde{T}^{\mu\nu}$ have the same units as well as $\tilde{\partial}_\nu$ [1/length]. The actual conserved variables are then $\tau\tilde{T}^{\mu\tau}$, and fluxes $\tau\tilde{T}^{ij}$, so that $\tilde{T}^{\eta\eta} = (\epsilon + p)\tilde{u}^\eta\tilde{u}^\eta + p$, where $\tilde{u}^\eta = \tau u^\eta$. Then equations (4.4.14) provide the explicit form of the energy-momentum and charge conservation equations which are solved numerically. The above equations were exploited for numerical solving of expanding bulk matter.

4.5 Equation of state

One of the advantages of hydrodynamic models over phenomenological models is their direct relation with the equation of state of QCD. Using the hydrodynamic models one

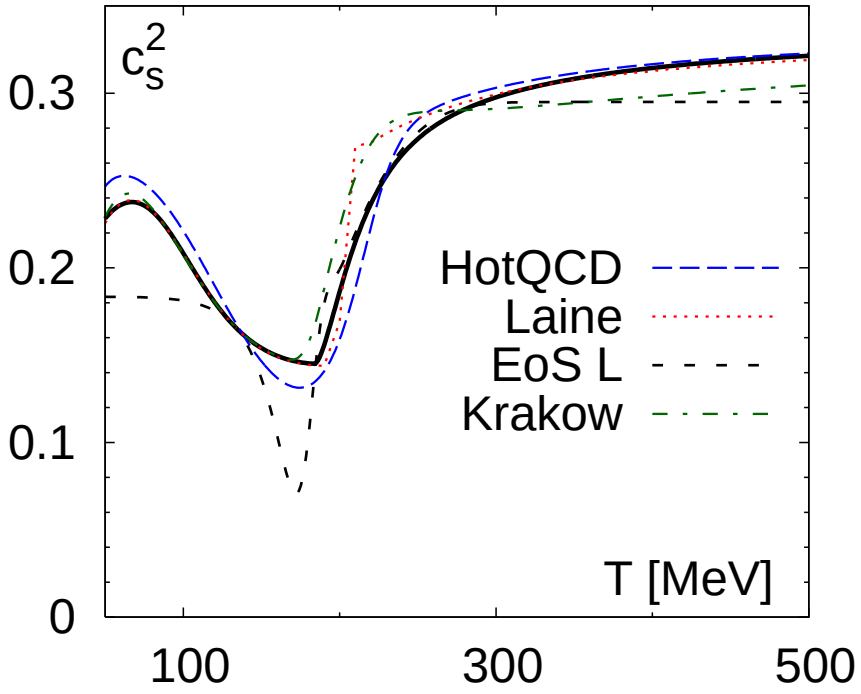

Figure 4.1: The speed of sound as a function of the temperature for different parametrizations used in hydrodynamic models. The solid black line corresponds to state-of-the-art EoS [88].

can find directly the consequence of the phase transition in experimental observables. Historically, the EoS with a first order phase transition based on the bag model was widely used because of its simplicity. In recent hydrodynamic calculations, lattice-inspired EoS has been widely employed, because of the development of thermodynamical analyses based on the first principle calculation, lattice QCD simulation. The EoS of QCD for 2+1 flavors and also EoS including charm quark by means of lattice simulations were reported by [88] or [89].

To be able to numerically solve hydrodynamic equations we must provide EoS as mentioned earlier by relation $p(\epsilon, n)$ which relates the local thermodynamic quantities. For our simulations we have used a modeled state-of-the-art EoS by Huovinen and Petreczky [88], which combines hadron resonance gas at low temperatures with lattice QCD at high temperatures. For comparison, some calculations were done with Laine's EoS [90] which is derived from hadron resonance gas at low temperatures, a high-order weak-coupling perturbative QCD calculation at high temperatures, and an analytic crossover regime interpolating between the high and low temperature regime. Results obtained with the two EoS were compared. The differences in results between these Equations of State are very small.

The brief description of the employed EoS [88] will be given below. Available lattice data provide an EoS which is not easy to use in hydrodynamic models because different thermodynamic quantities are suppressed in the low temperature region due to discretization errors. In lattice QCD, the calculation of the pressure, energy density and entropy density usually proceeds through the calculation of the trace anomaly $\Theta(T) = \epsilon(T) - 3p(T)$. Thermodynamic trace anomaly is simply the difference between the considered EoS and the EoS in ultrarelativistic limit ($\epsilon = 3p$), i.e. ($\epsilon - 3p$). Using the thermodynamic identity, the pressure difference at temperatures T and T_{low} can be expressed as the integral of the trace anomaly

$$\frac{p(T)}{T^4} - \frac{p(T_{low})}{T_{low}^4} = \int_{T_{low}}^{T} \frac{dT'}{T'^5}\Theta(T'). \tag{4.5.1}$$

By appropriate choosing of the lower integration limit T_{low} sufficiently small, $p(T_{low})$ can be neglected due to the power law suppression. Region below T_{low} uses the assumption that thermodynamics there is well described by a gas of non-interacting hadrons and resonances. Then the energy density $\epsilon(T) = \Theta(T) + 3p(T)$ and the entropy density $s(T) = (\epsilon + p)/T$ can be calculated. This procedure is known as the integral method [91]. Finite temperature lattice calculations are usually performed at fixed temporal extent N_τ and the temperature is varied by varying the lattice spacing a, $T = 1/(N_\tau a)$. Thus, calculations at low temperatures are performed on coarse lattices, while the lattice spacing gets smaller as the temperature is increased. Consequently the trace anomaly can be accurately calculated in the high temperature region, while in the low temperature region it is affected by possibly large discretization effects. Therefore, to construct realistic EoS authors [88] use the lattice data for the trace anomaly in the high temperature region, $T >$250 MeV, and use hadron resonance gas model in the low temperature region $T \lessapprox$ 180 MeV. The hadron resonance gas model with modified masses appears to describe the lattice data quite well up to temperatures of about $<$ 180 MeV. In the intermediate temperature region 180 MeV$\lessapprox$ T $<$ 250 MeV the hadron resonance gas model is no longer reliable, whereas discretiztion effects in lattice calculations could be large. The trace anomaly in the intermediate region is constrained only by the value of the entropy density at high temperatures. So the guidance from existing lattice QCD calculations is used which require that the entropy density is below the ideal gas limit by either 5% or 10%, when parametrizing the trace anomaly.

At high temperature the trace anomaly can be well parametrized by the inverse polynomial form [92]. Therefore the parametrization used in [88] employs the following Ansatz

for the high temperature region

$$(e-3p)/T^4 = d_2/T^2 + d_4/T^4 + c_1/T^{n_1} + c_2/T^{n_2}, \tag{4.5.2}$$

with d_2=0.2660 GeV^2, $d_4 = 2.403 \times 10^{-3}$, $c_1 = -2.809 \times 10^{-7}$ GeV^{10}, $c_2 = 6.073 \times 10^{-23}$ GeV^{30}, n_1=10 and n_2=30. This form does not have the right asymptotic behavior in the high temperature region, where we expect $(\epsilon - 3p)/T^4 \sim g^4(T)1/\ln^2(T/\Lambda_{QCD})$, (where g is the gauge coupling parameter and Λ_{QCD} denotes QCD scale) but works well in the temperature range of interest. Furthermore, it is flexible enough to do the matching to the hadron resonance gas result in low temperature region. It is matched to the hadron resonance gas model at temperature T_0 by requiring that the trace anomaly as well as its first and second derivatives are continuous. The hadron resonance gas result for the trace anomaly can also be parametrized by the simple form

$$\frac{\epsilon - 3p}{T^4} = a_1 T + a_2 T^3 + a_3 T^4 + a_4 T^{10}, \tag{4.5.3}$$

with a_1 =4.654 GeV^{-1}, $a_2 = -879$ GeV^{-3}, a_3=8081 GeV^{-4}, $a_4 = -7039000$ GeV^{-10} and T_0=183.8 MeV.

4.6 Freeze-out

At some stage in the evolution of the matter produced in a heavy-ion collision, the system will become too dilute for hydrodynamic description to be applicable. This "freeze-out" process is most probably happening gradually, but difficult to model realistically. A widely used approximation is therefore to assume instantaneous freeze-out whenever a certain fluid cell cools below a certain predefined temperature or energy density. The standard prescription for this freeze-out process is the Cooper-Frye formula [93], which allows conversion of the hydrodynamic variables (energy density, fluid velocity,...) into particle distributions. Specifically, in the case of isothermal freeze-out at a temperature T_f, the conversion from hydrodynamic to particle degrees of freedom will have to take place on a three-dimensional freeze-out hypersurface Σ, which can be characterized by its normal four-vector, and parametrized by three space-time variables [94, 95]. The single-particle spectrum for species with degeneracy g is then given by

$$E\frac{d^3N}{d^3\mathbf{p}} = \frac{g}{(2\pi)^3}\int_\Sigma p_\mu d\Sigma^\mu f(x^\mu, p^\mu), \tag{4.6.1}$$

where $d\Sigma_\mu$ is the normal vector on the hypersurface Σ and f is the distribution function. The number of hadrons being produced on the freeze-out hypersurface Σ^μ is expressed by the following integral

$$N = g\int \frac{d^3\mathbf{p}}{(2\pi)^3 E}\int d\Sigma_\mu(x) p^\mu f(x^\mu, p^\mu), \tag{4.6.2}$$

where the phase-space distribution function of the particles (the stable ones and resonances) can be written for ideal hydrodynamics as

$$f(x^\mu, p^\mu) = \left\{\exp\left[\frac{p_\mu u^\mu - (B\mu_B + I_3\mu_{I_3} + S\mu_S + C\mu_C)}{T}\right] \pm 1\right\}^{-1}. \tag{4.6.3}$$

Physical meaning of the introduced variables is following: T is temperature, μ_B is baryon chemical potential, μ_{I_3} is isospin chemical potential, μ_S is strange chemical potential, μ_C is charmed chemical potential, B is baryon number, I_3 is 3rd component of isospin, S is strangeness and C is charm. Normal vector $d\Sigma^\mu$ may be calculated with the help of the formula from differential geometry [96],

$$d\Sigma_\mu = \epsilon_{\mu\alpha\beta\gamma}\frac{\partial x^\alpha}{\partial\alpha}\frac{\partial x^\beta}{\partial\beta}\frac{\partial x^\gamma}{\partial\gamma}d\alpha d\beta d\gamma, \tag{4.6.4}$$

where $\epsilon_{\mu\alpha\beta\gamma}$ is the Levi-Civita tensor ($\epsilon_{0123} = +1$) and the variables α, β, and γ are used to parametrize the three-dimensional Minkowski space. The quantity $d\Sigma^\mu$ may be interpreted as the four-vector normal to the hypersurface with the norm equal to the volume of the hypersurface element. Explicitly,

$$d\Sigma_0 = \begin{vmatrix} \frac{\partial x}{\partial\alpha} & \frac{\partial x}{\partial\beta} & \frac{\partial x}{\partial\gamma} \\ \frac{\partial y}{\partial\alpha} & \frac{\partial y}{\partial\beta} & \frac{\partial y}{\partial\gamma} \\ \frac{\partial z}{\partial\alpha} & \frac{\partial z}{\partial\beta} & \frac{\partial z}{\partial\gamma} \end{vmatrix} d\alpha d\beta d\gamma, \tag{4.6.5}$$

while the remaining components are obtained via cyclic permutations of t, x, y, and z. The formulas are directly used to generate the hadrons with the Monte-Carlo method implemented in THERMINATOR2 package [97]. THERMINATOR2 package was used to convert thermodynamic variables obtained from hydrodynamic simulations into observable particles. Description of THERMINATOR2 is given in Section 4.8.

Originally, the Cooper-Frye prescription was derived for systems in thermal equilibrium, where f is built out of a Bose-Einstein or Fermi-Dirac distribution, function $f_0(u^\mu p_\mu) = (\exp[u^\mu p_\mu - \mu_i] \pm 1)^{-1}$ depending on the statistics of the particle under consideration. In order to generalize it to systems out of equilibrium, one customarily relies on the ansatz used in the derivation of viscous hydrodynamics from kinetic theory [98].

In the early days of hydrodynamics only kinetic freeze-out was implemented. Indeed, at lower collision energies such as at SIS and AGS, the separation between the chemical freeze-out and kinetic freeze-out points is not large on the $T-\mu$ plane. At RHIC and LHC there may be a significant difference between kinetic freezeout temperatures from hydro-inspired models and the chemical freeze-out from the statistical model [99]. Nevertheless, there is a Cracow single freeze-out model which assumes that chemical and thermal freeze-out occur simultaneously [100, 101]. It turns out that some experimental data are still not understood in a satisfactory way even with the two separate freeze-outs. For example, mean transverse momentum p_T as a function of particle mass does deviate from the linear scaling law, which suggests significant final state interactions in the hadronic phase [102].

To explain these effects, and to account for the apparently large viscosities in the hadronic phase, as discussed before, hydro+cascade hybrid models were introduced. They use hydrodynamic computation of the expansion and cooling of hot QCD bulk matter, and then couple the output consistently to a hadron-based transport model in order to take an account of the final state interactions. A pioneering work on hydro+cascade hybrid models was done by Bass *et al.* [103] using UrQMD.

The Cooper-Frye recipe [93] has been extensively used in hydrodynamic calculations, however it is not free of problems either. It gives negative contribution to the particle

spectrum in some kinematic regions in which the normal vector to the freeze-out hypersurface is time-like, $p_\mu n_\sigma^\mu < 0$. This negative contribution corresponds to frozen out particles returning to the hydro phase (see Fig. 4.2). Cut off of this negative contribution drives us to the violation of the energy conservation. To get rid of this negative spectrum, there was a proposal of the Cooper-Frye recipe modification based on a cut Jüttner distribution [104, 105, 106, 107]. Jüttner distribution could be described as relativistic Boltzmann distribution that means that in limit where $c \to \infty$ Jüttner distribution becomes identical to Boltzmann's. In this distribution the part of the Jüttner distribution that gave the negative spectrum is simply cut off. To ensure the energy conservation, the rest of Jüttner distribution is renormalized, effectively resulting in a new temperature and chemical potential (so called "freeze-out shock"). In fact, this cut-Jüttner recipe has no physical justification, except for practical utility. Moreover the cut-Jüttner recipe is not supported by schematic kinetic treatment [108] of the transition region from hydro regime to that of dilute gas. There was proposal of a new freeze-out recipe, a canceling-Jüttner distribution [109], which complies with the results of schematic kinetic treatment [108]. The region, where the transition from highly collisional dynamics to the collisionless one occurs, is highly difficult for the kinetic treatment and hardly allows any justified simplifications.

4.7 Brief overview of statistical models

Statistical models have proved to be very useful in the description of soft physics in relativistic heavy-ion collisions [110]. In particular, with a few phyical input parameters, such as the temperature, chemical potentials, and velocity of the collective flow, the models reproduce the observed particle abundances [111, 112, 113, 114, 115, 116], the transverse-momentum spectra [100], the balance functions [117], the elliptic flow coefficient [118], and femtoscopic observables [119, 120]. The key element of the approach is the inclusion of the complete list of hadronic resonances, whose number grows rapidly as a function of their mass according to the Hagedorn hypothesis [121, 122, 123, 124, 125]. Their two- and three-body decays, taken from the tables, proceed in cascades, ultimately producing the stable particles observed in detectors. There are several codes to compute the abundances of particles such as SHARE [126] or THERMUS [127]. It is a simple task, since the abundances are insensitive to the geometry of the fireball and its expansion. The calculation of the transverse-momentum spectra of particles is much more complicated due to the sensitivity to these phenomena. THERMINATOR2 [97], described in the next section, deals with this issue, offering the full information on space-time positions and momenta of the produced particles. As a result, the program allows to compute very efficiently the transverse-momentum spectra of identified particles and examine implications of the assumed expansion model. In the next paragraph we start with statistical approach with grand canonical formalism.

The basic quantity required to compute the thermal composition of particle yields measured in heavy ion collisions is the partition function $Z(T, V)$. In the Grand Canonical (GC) ensemble, it can be written as

$$Z^{GC}(T, V, \mu_q) = \mathrm{Tr}[\exp(-\beta(H - \sum_i \mu_{Q_i} Q_i))], \tag{4.7.1}$$

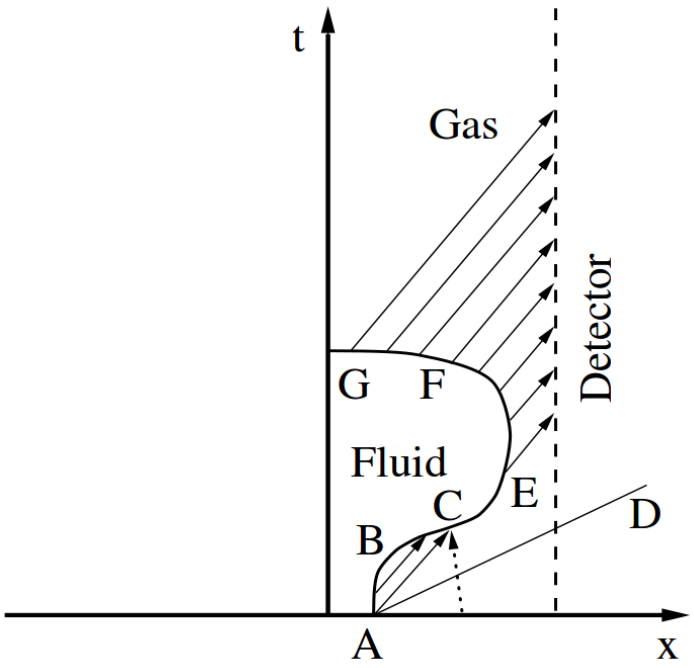

Figure 4.2: Decay of the fluid into the gas of free particles on the concave freeze-out hypersurface $ABCDEFG$. Trajectories of the particles are indicated by the lines with arrows. Dashed line represents the detector's world line. Line AD denotes light cone. For given particle velocity $v = p^x/p^0$ the integration limits in coordinate space, points E and G, are found from the condition $p_\rho d\sigma^\rho = 0$. In this case, however, one has to take into account the particles feeding back to fluid on the part ABC of the freeze-out hypersurface. These particles were emitted earlier and do not appear from rescattering. The latter is forbidden by the assumption that particle spectra are "frozen" once they belong to the gas of free particles. Hence, particle trajectories, like the one shown by the dotted line, are not allowed in the freeze-out picture because those particles appear from nothing [104].

where H is the Hamiltonian of the system, $\beta = 1/T$ is the inverse temperature, Q_i are the conserved charges and μ_{Q_i} are the chemical potentials that guarantee that the charges Q_i are conserved on the average in the whole system. The Hamiltonian is usually the one describing hadron resonance gas. The main motivation of using the Hamiltonian of hadron resonance gas in the partition function is that it contains all relevant degrees of freedom of the confined, strongly interacting medium. Second one is that this model is consistent with the EoS obtained from the lattice gauge theory below the critical temperature [128]. In a strongly interacting medium, one includes the conservation of electric charge, baryon number and strangeness. The GC partition function of a hadron resonance gas can then be written as a sum of partition functions $\ln Z_i$ of all hadrons and resonances

$$\ln Z(T, V, \vec{\mu}) = \sum_i \ln Z_i(T, V, \vec{\mu}), \tag{4.7.2}$$

where $\vec{\mu} = (\mu_B, \mu_S, \mu_Q)$ are the chemical potentials related to baryon number, strangeness and electric charge, respectively. Thus, for particle i of strangeness S_i, baryon number

B_i, electric charge Q_i, degeneracy factor g_i, and energy $\epsilon_i = \sqrt{p^2 + m_i^2}$, it is

$$\ln Z_i(T, V, \vec{\mu}) = \frac{V g_i}{2\pi^2} \int_0^{+\infty} \pm p^2 dp \ln[1 \pm \lambda_i \exp(-\beta\epsilon_i)], \tag{4.7.3}$$

where + stands for fermions, – for bosons and the fugacity $\lambda_i(T, \vec{\mu})$ is defined as

$$\lambda_i(T, \vec{\mu}) = \exp\left(\frac{B_i\mu_B + S_i\mu_S + Q_i\mu_Q}{T}\right). \tag{4.7.4}$$

Expanding the logarithm and performing the integration over momentum, we obtain

$$\ln Z_i(T, V, \vec{\mu}) = \frac{VTg_i}{2\pi^2} \sum_{k=1}^{\infty} \frac{(\pm 1)^{k+1}}{k^2} \lambda_i^k m_i^2 K_2\left(\frac{km_i}{T}\right), \tag{4.7.5}$$

where K_2 is the modified Bessel function and the upper sign is for bosons and lower for fermions. The density of particle i is then

$$n_i(T, \vec{\mu}) = \frac{\langle N_i \rangle}{V} = \frac{Tg_i}{2\pi^2} \sum_{k=1}^{\infty} \frac{(\pm 1)^{k+1}}{k} \lambda_i^k m_i^2 K_2\left(\frac{km_i}{T}\right). \tag{4.7.6}$$

In view of importance of accounting for resonances and their decay into lighter particles we can rewrite the particle average number $\langle N \rangle$ of species i in volume V and temperaure T, that carries strangeness S_i, baryon number B_i, and electric charge Q_i, using Eq. (4.7.1) as

$$\langle N_i \rangle(T, \vec{\mu}) = \langle N_i \rangle^{th}(T, \vec{\mu}) + \sum_j \Gamma_{j\to i} \langle N_j \rangle^{th,R}(T, \vec{\mu}), \tag{4.7.7}$$

where the first term describes the thermal average number of particles of species i. The second term is taken as a sum of all resonances that decay into particle species i. The $\Gamma_{j\to i}$ is the corresponding decay branching ratio of $j \to i$. The corresponding multiplicities in Eq. (4.7.7) are obtained from Eq. (4.7.6). This is important at high temperature or density since the overall multiplicity of light hadrons is dominated by resonance decays. If T and/or μ_b is large, the repulsive interactions of hadrons should be included in the partition function Eq. (4.7.1). To incorporate the repulsion at short distances one usually uses a hard core description by implementing excluded volume corrections [129]. In a thermodynamically consistent approach [130] these corrections lead to a shift of the baryo–chemical potential. The repulsive interactions are important when discussing observables of density type. However, particle density ratios, are only weakly affected [131] by the repulsive corrections.

The partition function (4.7.1) depends generally on five parameters. However, only three of them are independent, since the isospin symmetry in the initial state fixes the charge chemical potential and the strangeness neutrality condition eliminates the strange chemical potential. Thus, on the level of particle multiplicity ratios, we are only left with temperature T and baryonic chemical potential μ_B as independent parameters. More details concerning practical application and results can be found in [110].

4.8 THERMINATOR2 description

When hydrodynamic evolution ends, i.e. the energy density in fireball descends below some value $\epsilon_{freeze-out}$, the freeze-out hypersurface is recorded. In our simulations, this hypersurface is input for THERMINATOR2 [97], a Monte Carlo event generator dedicated to studies of the statistical production of particles in relativistic heavy-ion collisions. The code has an important feature: it allows the input of any shape of the freeze-out hypersurface and the expansion velocity field, including the 3+1 dimensional profiles, in particular those generated externally with various hydrodynamic codes. In our simulations, freeze-out in THERMINATOR2 is handled by the Cooper-Frye prescription [93], on the hypersurface given by $T = 150$ MeV.

THERMINATOR2 is updated and largely extended version of THERMINATOR [132], the THERMal heavy IoN generATOR, created to carry out the statistical hadronization in relativistic heavy-ion collisions. Numerous successful analyses have been performed by means of this code [133, 134, 135, 136]. As THERMINATOR2 is a Monte Carlo event generator written in the object-oriented C++ language in the ROOT [137] environment it can be straightforwardly used in data analysis, detector modeling, or estimates for relativistic heavy-ion colliders, such as RHIC and LHC.

Figure 4.3 describes the system of coordinates used to parametrize the freeze-out hypersurface obtained from the 3+1 dimensional hydrodynamic code. One axis denotes distance in transverse plane $\rho = \sqrt{x^2 + y^2}$, second axis denotes proper time past from initial proper time for hydrodynamics, third axis denotes space-time rapidity scaled with parameter Λ to get correct dimension, ζ denotes angle in $\rho - \tau$ plane, θ describes angle between Y_s-axis and the direction determined by the origin and the point on the freeze-out hypersurface. Finally, d is the distance from the origin to the point on the freeze-out hypersurface. Minkowski coordinates are obtained as [138],

$$t = (\tau_i + d(\zeta, \phi, \theta) \sin\theta \sin\zeta) \cosh \frac{d(\zeta, \phi, \theta)}{\Lambda}, \tag{4.8.1}$$

$$x = d(\zeta, \phi, \theta) \sin\theta \cos\zeta \cos\phi, \tag{4.8.2}$$

$$y = d(\zeta, \phi, \theta) \sin\theta \cos\zeta \cos\phi, \tag{4.8.3}$$

$$z = (\tau_i + d(\zeta, \phi, \theta) \sin\theta \sin\zeta) \sinh \frac{d(\zeta, \phi, \theta)}{\Lambda}. \tag{4.8.4}$$

The parameter Λ is a scale used to change the dimensionless space-time rapidity Y_s into a dimensional quantity, namely

$$Y_s = Y_s(\zeta, \phi, \theta) = \frac{d(\zeta, \phi, \theta)}{\Lambda},$$
$$\tau = \tau(\zeta, \phi, \theta) = \tau_i + d(\zeta, \phi, \theta) \sin\theta \sin\zeta. \tag{4.8.5}$$

In addition, the particle four-momentum and the fluid four-velocity can be expressed in terms of particle rapidity $Y = \frac{1}{2} \ln \frac{E+p_z}{E-p_z}$ and fluid rapidity $Y_f = \frac{1}{2} \ln \frac{1+v_z}{1-vz}$, respectively, which leads to the expression

$$p_\mu u^\mu = \sqrt{1 + u_x^2 + u_y^2}[m_t \cosh(Y_f - Y) - p_t(u_x \cos\phi_p + u_y \sin\phi_p)]. \tag{4.8.6}$$

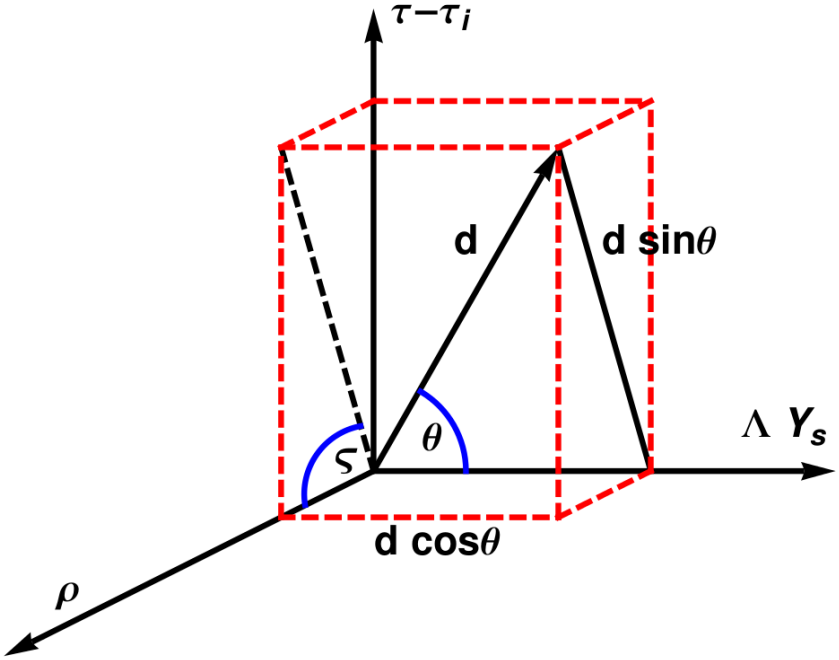

Figure 4.3: The system of coordinates used to parametrize the freeze-out hypersurfaces obtained from the 3+1 hydrodynamic codes. Figure taken from [97].

The calculation of the integration measure in the Cooper-Frye formula gives

$$d\Sigma_\mu p^\mu = \frac{d\sin\theta}{\Lambda} d\tau \Big[\frac{\partial d}{\partial \zeta} \cos\zeta \Big(-m_t \cos\zeta \cosh(Y - Y_s) + p_t \sin\zeta \cos(\phi - \phi_p) \Big) + \cos\zeta \sin\theta (d\sin\theta - \frac{\partial d}{\partial \theta}\cos\theta) \times \Big(m_t \sin\zeta \cosh(Y - Y_s) + p_t \cos\zeta \cos(\phi - \phi_p) \Big) + \frac{\partial d}{\partial \phi} p_t \sin(\phi - \phi_p) + \frac{\Lambda}{\tau}(d\cos\theta + \frac{\partial d}{\partial \theta}\sin\theta)\sin\theta \sinh(Y - Y_s) \Big]. \quad (4.8.7)$$

The generation of particle distributions proceeds in three main steps, two of which are performed only once per given parameter set. In order to generate particles through a Monte Carlo method, the maximum value of the distributions for different species in right hand side of Eq. (4.6.1) must be known. It is found through a simple numerical procedure. A sample of particles is generated and the values of the distributions are calculated for each of them. The maximum value obtained is taken as the maximum of the requested distribution for the considered particle type. The maximum value depends, in principle, on the particle type and values of parameters, but does not change from event to event. Therefore the value is calculated once for each particle type and stored. Hence, subsequent generations of events with the same parameters do not require the regeneration of the maximum values. This saves computation time. In order to generate events, a multiplicity of each particle type must be known. The average multiplicity per event can be calculated in a straightforward manner by numerically integrating the distribution

functions in the given integration ranges (determined by the model parameters). This procedure must also be done only once per parameter set. The average multiplicity of each particle is then stored. The multiplicities are then read in by subsequent generations, saving the time of calculation.

In the next step the program proceeds to its ultimate goal of generating events, i.e., the data sets containing full information about produced particles, the history of their evolution, resonance decays, etc. Each event is generated separately. First, the multiplicities of each particle type are generated as random numbers from a Poissonian distribution, with the mean being the average particle multiplicity determined earlier.

Then the program proceeds to generate particles, sequentially from the heaviest to the lightest particle type depending on the selected model. The event generation procedure is a standard von Neumann method of rejection/acceptance of the given set of numbers based on the randomly generated test value distributed uniformly between 0 and f_{max}, where f_{max} is the maximum value of the distribution determined earlier. The procedure ends when the determined number of particles of each particle type is generated. All the primordial particles, stable and resonances, have been generated and stored in the event.

In subsequent procedure the decays of resonances proceed sequentially from the heaviest to the lightest particle. The decay daughters are immediately added to the set of particles in the current event, hence they may decay in the subsequent steps. Most particles have several decay channels. In each decay one of them is selected randomly with appropriate probability corresponding to the branching ratio. Details concerning the implementation of two-body and three-body decays can be found in [97].

Chapter 5

Numerical methods for solving hydrodynamic equations

In this chapter we present detailed description of the numerical alorithm used to solve the equations of relativistic fluid dynamics in (3+1) dimensional geometries starting from (1+1) dimensional geometry. Detailed implementation follows the state-of-the-art SHASTA algorithm approach presented in [139]. No suitable hydrodynamic code was available at the time of implementation, so for our simulations it was necessary to implement this approach from the very beginning.

In solving the equations of hydrodynamics numerically, we should be able to resolve all relevant time and length scales in the problem. In practice this means that the grid spacing Δx and time step Δt should be smaller than any of these scales. In perfect fluid dynamics all scales are macroscopic, i.e., they are inversely proportional to the gradients of the fluid-dynamical variables like flow field and densities. Thus it is sufficient to have a numerical resolution that correctly resolves the macroscopic structures. However, shocks introduce scales below this spacing. Therefore shock-wave capturing schemes play an important role to deal with discontinuities in the event-by-event fluctuating initial conditions. A lot of shock-wave capturing schemes have been proposed and developed.

In relativistic heavy-ion collisions, SHASTA [140], rHLLE [141], and KT (Kurganov and Tadmor) [142] algorithms are mainly used. The work of [139] compares between the different shock-wave capturing schemes, SHASTA, KT, and NT (Nessyahu and Tadmor) [143] schemes were made and it was found that all the algorithms reproduce the analytic solution of shock propagation with nearly the same accuracy and numerical artifacts. In particular, SHASTA-based algorithms [140], are widely used in the study of relativistic heavy-ion collisions. SHASTA-based algorithms are known as the versions of Flux Corrected Transport (FCT) algorithm. The SHASTA algorithm was used here because it can handle numerical diffusion and oscillations originating from hydrodynamic computations with steep gradients very well.

5.1 SHASTA

SHASTA (SHarp And Smooth Transport Algorithm) [140] is a flux-corrected transport algorithm for solving generalized continuity equations. It can be used for non-relativistic calculations as well as for relativistic calculations. In the phenomena occuring in heavy ion physics, convection is often not a simple flow, but rather it has shock waves, where the profile of fluid properties has strong discontinuity or steep gradients. Therefore, we need numerical algorithm which can handle these discontinuities. The important properties of Flux-Corrected Transport (FCT) are that it is a high-order, monotone, conservative, positivity preserving algorithm. This means that the algorithm is accurate and resolves steep gradients, allowing grid scale numerical resolution. When a convected quantity such as an energy density is initially positive, it remains positive and no new maxima or minima are introduced due to numerical errors in the convection process. These are the properties that are extremely important for most problems of practical interest. Due to its simplicity, accuracy, and easy implementation we choose the SHASTA [140] which was one of the first versions of Flux Corrected Transport algorithms in the 1970's. Ever since, the FCT method has been extensively tested and refined for various studies, for example, the ETBFCT version by Boris [144], which also forms the basis for the LCPFCT algorithm [145], and the YDFCT algorithm by Toth and Odstrcil [146].

The SHASTA algorithm is an example for an algorithm that uses a stable but diffusive difference scheme. Numerical diffusion is of conservative form and arises as a consequence of the physical requirements that the profiles being convected remain stable while remaining positive. Numerical diffusion is an inherent problem in Eulerian convection, and unless controlled, it can invalidate numerical calculations using linear algorithms unless they have very fine computational meshes. The basic idea of the flux-corrected transport method is to increase the stability of a differencing scheme by introducing a corrective nonlinear diffusion step. In the succeeding antidiffusion step this diffussion is removed partially by flux limiter to avoid spurious oscillations while retaining sharp profiles in cases of discontinuities or steep gradients.

5.2 One-dimensional application of SHASTA algorithm

How one can solve hydrodynamic equations numerically using SHASTA? To solve hydrodynamic equations numerically, the original partial differential equations are replaced by an approximate algebraic difference equations and the values of U, v, and J are given at discrete grid points, where $U = U(t, x)$ is conserved quantity, v_x is the flow velocity in x direction and $J = J(t, x)$ is the source term. For example $U(t, x)$ can correspond to charge density N, energy density E or momentum density M^i in laboratory frame. The conservative, or primary, variable $U(t, x)$ is replaced by its average U_i^n over the cell i at coordinate point x_i , and at the discrete time step t^n. In (1+1)-dimensional systems the equations of charge and energy-momentum conservation are of conservation type and can

be generally written as

$$\partial_t U + \partial_x(v_x U) = J(t,x). \tag{5.2.1}$$

If we consider for example equation (4.1.19) then the conserved quantity U corresponds to E and the source term J corresponds to $J^t - \partial_x(pv_x)$. The transported and diffused, uncorrected solution $\tilde{U}$ in the explicit SHASTA method [140] is given by

$$\tilde{U}_i = \frac{1}{2}(Q_+^2\Delta_i - Q_-^2\Delta_{i-1}) + (Q_+ - Q_-)U_i^n + \Delta t J_i. \tag{5.2.2}$$

Here, we defined

$$\Delta_i = U_{i+1}^n - U_i^n, \tag{5.2.3}$$

$$Q_\pm = \frac{1/(2\lambda) \pm v_i^n}{1/\lambda \pm (v_{i\pm1}^n - v_i^n)}, \tag{5.2.4}$$

where $\lambda = \Delta t/\Delta x$ is the Courant number which in SHASTA is restricted to values $\lambda \leq 1/2$ to assure causality. The final time-advanced quantities are calculated by subtracting so-called antidiffusion fluxes, $\tilde{A}$, from the transported and diffused solution

$$U_i^{n+1} = \tilde{U}_i - \tilde{A}_i + \tilde{A}_{i-1}, \tag{5.2.5}$$

where the flux-corrected antidiffusion flux is

$$\tilde{A}_i = \sigma_i \max(0, \min(\sigma_i\tilde{\Delta}_{i+1}, |A_i|, \sigma_i\tilde{\Delta}_{i-1})). \tag{5.2.6}$$

The difference of primary variables in adjacent cells is denoted by $\tilde{\Delta}_i = \tilde{U}_{i+1} - \tilde{U}_i$, while the explicit antidiffusion flux is

$$A_i = A_{ad}\tilde{\Delta}_i/8, \tag{5.2.7}$$

$$\sigma_i = \mathrm{sgn}(A_i). \tag{5.2.8}$$

In SHASTA, $A_{ad} = 1$ is the default value of the so-called mask coefficient [147]. This is a multiplicative constant which can be set to lower values to reduce the amount of antidiffusion. Second-order accuracy in time is obtained by applying SHASTA twice. First we calculate the velocity and source terms at time step $n + 1/2$. In the second step, these half-step velocity and source terms are used to calculate the final time-advanced quantity U_i^{n+1}. In a given cell, this can be summarized in formulas as

$$U^{n+1/2} = U^n(U^n, v^n, J^n, \Delta t/2, \Delta x), \tag{5.2.9}$$

$$U^{n+1} = U^n(U^n, v^{n+1/2}, J^{n+1/2}, \Delta t, \Delta x). \tag{5.2.10}$$

5.2.1 Three-dimensional application of SHASTA algorithm

Provided that we want to calculate with realistic hydrodynamic model we need to extend one-dimensional SHASTA algorithm into three dimensions. Thus (3+1)-dimensional conservation equations can be written as

$$\partial_t U + \partial_x(v_x U) + \partial_y(v_y U) + \partial_z(v_z U) = J(t,x,y,z). \tag{5.2.11}$$

The cell-averaged conserved variable $U(t,x,y,z)$ is denoted by $U^n_{i,j,k}$. A standard approach to solve such equations is to apply the dimensional or operator splitting method, which splits the original multidimensional equation into a sequence of (1+1)–dimensional problems [148]. A slightly different but more efficient approach [139] is used in this work. The low-order transport solution is calculated separately in the x, y and z directions by using the (1+1)–dimensional SHASTA without the source term. Thus, the x-transported quantity $\tilde{U}^x_{i,j,k}$ is given as

$$\tilde{U}^x_{i,j,k} = \frac{1}{2}[(Q^x_+)^2\Delta^x_{i,j,k} - (Q^x_-)^2\Delta^x_{i-1,j,k}] + (Q^x_-)U^n_{i,j,k}, \tag{5.2.12}$$

$$Q^x_\pm = \frac{1/(2\lambda^x) \mp (v_x)^n_{i,j,k}}{1/\lambda^x \pm [(v_x)^n_{i\pm1,j,k} - (v_x)^n_{i,j,k}]}, \tag{5.2.13}$$

where $\Delta^x_{i,j,k} = U^n_{i+1,j,k} - U^n_{i,j,k}$ and $\lambda^x = \Delta x/\Delta t \leq 1/2$ is the Courant number in the x-direction. A similar formula, with v_x replaced by v_y or v_z and all cell differences taken in y- or z-direction, holds for the y- or z-transported quantity $\tilde{U}^y_{i,j,k}$ or $\tilde{U}^z_{i,j,k}$. The transported and diffused solution is then

$$\tilde{U}_{i,j,k} = \tilde{U}^x_{i,j,k} + \tilde{U}^y_{i,j,k} + \tilde{U}^z_{i,j,k} - 2U^n_{i,j,k} + \Delta t J_{i,j,k}. \tag{5.2.14}$$

The advantage of this method is that it keeps the symmetry between any two directions of the system without the need to permute the directions in which the grid is updated. In this case it is also possible to implement a multidimensional flux correction in the FCT algorithm which avoids some numerical problems and leads to slightly smoother results compared to the dimensional splitting method for the same mask coefficient. To obtain second order accuracy, the method by DeVore [149] is used. The full solution is given by

$$U^{n+1}_{i,j,k} = \tilde{U}_{i,j,k} - \hat{A}^x_{i,j,k} - \hat{A}^y_{i,j,k} - \hat{A}^z_{i,j,k} + \hat{A}^x_{i-1,j,k} + \hat{A}^y_{i,j-1,k} + \hat{A}^z_{i,j,k-1}, \tag{5.2.15}$$

where the $\hat{A}$'s are the limited antidiffusion fluxes given in Equations (5.2.29, 5.2.30) and (5.2.31) below. In our implementation, the updates are computed in such a way that the conserved quantity U does not depend on order of directional updates. (Directional updates are computed separately and finally added together.) As in the (1+1)–dimensional case the antidiffusion fluxes in x, y and z directions are given by

$$\begin{aligned} A^x_{i,j,k} &= A^x_{ad}\tilde{\Delta}^x_{i,j,k}/8, \\ A^y_{i,j,k} &= A^y_{ad}\tilde{\Delta}^y_{i,j,k}/8, \\ A^z_{i,j,k} &= A^z_{ad}\tilde{\Delta}^z_{i,j,k}/8, \end{aligned} \tag{5.2.16}$$

where $A^x_{ad}, A^y_{ad}, A^z_{ad}$ are the antidiffusive mask coefficients, similarly to the (1+1)-dimensional case. Furthermore,

$$\tilde{\Delta}^x_{i,j,k} = \tilde{U}_{i+1,j,k} - \tilde{U}_{i,j,k}, \tag{5.2.17}$$

$$\tilde{\Delta}^y_{i,j,k} = \tilde{U}_{i,j+1,k} - \tilde{U}_{i,j,k}, \tag{5.2.18}$$

$$\tilde{\Delta}^z_{i,j,k} = \tilde{U}_{i,j,k+1} - \tilde{U}_{i,j,k}. \tag{5.2.19}$$

In the DeVore scheme, the antidiffusion fluxes in x, y and z directions are first limited as in the (1+1)–dimensional case,

$$\tilde{A}^x_{i,j,k} = \sigma^x_{i,j,k} \max[0, \min(\sigma^x_{i,j,k}\tilde{\Delta}^x_{i+1,j,k}, |A^x_{i,j,k}|, \sigma^x_{i,j,k}\tilde{\Delta}^x_{i-1,j,k})], \tag{5.2.20}$$

$$\tilde{A}^y_{i,j,k} = \sigma^y_{i,j,k} \max[0, \min(\sigma^y_{i,j,k}\tilde{\Delta}^y_{i,j+1,k}, |A^y_{i,j,k}|, \sigma^y_{i,j,k}\tilde{\Delta}^y_{i,j-1,k})], \tag{5.2.21}$$

$$\tilde{A}^z_{i,j,k} = \sigma^z_{i,j,k} \max[0, \min(\sigma^z_{i,j,k}\tilde{\Delta}^z_{i,j,k+1}, |A^z_{i,j,k}|, \sigma^z_{i,j,k}\tilde{\Delta}^z_{i,j,k-1})], \tag{5.2.22}$$

where $\sigma^x_{i,j,k} = \mathrm{sgn}(A^x_{i,j,k})$, $\sigma^y_{i,j,k} = \mathrm{sgn}(A^y_{i,j,k})$ and $\sigma^z_{i,j,k} = \mathrm{sgn}(A^z_{i,j,k})$. The allowed values for $U^{n+1}_{i,j,k}$ after the antidiffusion stage are between

$$\begin{aligned} \tilde{U}^{min}_{i,j,k} = \min(&\tilde{U}_{i-1,j,k}, \tilde{U}_{i,j-1,k}, \tilde{U}_{i,j,k-1}, \tilde{U}_{i,j,k}, \\ &\tilde{U}_{i+1,j,k}, \tilde{U}_{i,j+1,k}, \tilde{U}_{i,j,k+1}), \end{aligned} \tag{5.2.23}$$

$$\begin{aligned} \tilde{U}^{max}_{i,j,k} = \max(&\tilde{U}_{i-1,j,k}, \tilde{U}_{i,j-1,k}, \tilde{U}_{i,j,k-1}, \tilde{U}_{i,j,k}, \\ &\tilde{U}_{i+1,j,k}, \tilde{U}_{i,j+1,k}, \tilde{U}_{i,j,k+1}). \end{aligned} \tag{5.2.24}$$

The total incoming and outgoing antidiffusive fluxes in cell (i, j, k) are calculated as

$$\begin{aligned} A^{in}_{i,j,k} = &\max(0, \tilde{A}^x_{i-1,j,k}) - \min(0, \tilde{A}^x_{i,j,k}) + \max(0, \tilde{A}^y_{i,j-1,k}) - \\ &\min(0, \tilde{A}^y_{i,j,k}) + \max(0, \tilde{A}^z_{i,j,k-1}) - \min(0, \tilde{A}^z_{i,j,k}), \end{aligned} \tag{5.2.25}$$

$$\begin{aligned} A^{out}_{i,j,k} = &\max(0, \tilde{A}^x_{i,j,k}) - \min(0, \tilde{A}^x_{i-1,j,k}) + \max(0, \tilde{A}^y_{i,j,k}) - \\ &\min(0, \tilde{A}^y_{i,j-1,k}) + \max(0, \tilde{A}^z_{i,j,k}) - \min(0, \tilde{A}^z_{i,j,k-1}). \end{aligned} \tag{5.2.26}$$

This information is then used to determine the fractions of the incoming and outgoing fluxes,

$$F^{in}_{i,j,k} = (\tilde{U}^{max}_{i,j,k} - \tilde{U}_{i,j,k})/A^{in}_{i,j,k}, \tag{5.2.27}$$

$$F^{out}_{i,j,k} = (\tilde{U}_{i,j,k} - \tilde{U}^{min}_{i,j,k})/A^{out}_{i,j,k}, \tag{5.2.28}$$

which is subsequently limited so that it creates no undershoot or overshoot in the cell, from which it is leaving or which is entering. Thus, the new antidiffusive fluxes are given as

$$\hat{A}^x_{i,j,k} = \tilde{A}^x_{i,j,k} \times \begin{cases} \min(1, F^{in}_{i+1,j,k}, F^{out}_{i,j,k}) & \text{if } \tilde{A}^x_{i,j,k} \geq 0, \\ \min(1, F^{in}_{i,j,k}, F^{out}_{i+1,j,k}) & \text{if } \tilde{A}^x_{i,j,k} < 0, \end{cases} \tag{5.2.29}$$

$$\hat{A}^y_{i,j,k} = \tilde{A}^y_{i,j,k} \times \begin{cases} \min(1, F^{in}_{i,j+1,k}, F^{out}_{i,j,k}) & \text{if } \tilde{A}^y_{i,j,k} \geq 0, \\ \min(1, F^{in}_{i,j,k}, F^{out}_{i,j+1,k}) & \text{if } \tilde{A}^y_{i,j,k} < 0, \end{cases} \tag{5.2.30}$$

and

$$\hat{A}^z_{i,j,k} = \tilde{A}^z_{i,j,k} \times \begin{cases} \min(1, F^{in}_{i,j,k+1}, F^{out}_{i,j,k}) & \text{if } \tilde{A}^z_{i,j,k} \geq 0, \\ \min(1, F^{in}_{i,j,k}, F^{out}_{i,j,k+1}) & \text{if } \tilde{A}^z_{i,j,k} < 0. \end{cases} \tag{5.2.31}$$

5.3 Numerical tests of implemented algorithm

In the previous section we have built the theory how to solve numerically hydrodynamic equations. In 3 + 1 dimensions, given arbitrary initial conditions and a general EoS, the

only way to solve the equations of relativistic fluid dynamics is by means of numerical methods. Any numerical method requires an algorithm that has to be tested in order to asses its validity for solving the underlying equations. Therefore, we implemented 3+1 dimensional SHASTA algorithm described previously and made various tests. The tests consist of two parts. One part concerns easier tests for static medium, the second one expanding medium. The second part will be presented in Subsection 6.3 because we need to introduce initial conditions needed to do the tests.

5.3.1 Static tests

Testing algorithms to solve relativistic dissipative fluid dynamics is made difficult by the fact that there is only a rather limited number of test cases with analytical solutions. One of them is the expansion of baryon-free matter into vacuum. That means that equation (4.1.4) was not taken into account. Such a test was used also in [150]. The following initial conditions at $t = 0$ were employed:

$$\epsilon(x,0) = \begin{cases} \epsilon_0 & x \leq 0 \\ 0 & x > 0, \end{cases} \tag{5.3.1}$$

$$v(x,0) = \begin{cases} 0 & x \leq 0 \\ c & x > 0, \end{cases} \tag{5.3.2}$$

The choice $v = c$ in the vacuum is purely conventional, but it guarantees a continuous hydrodynamic solution at the boundary to the vacuum, since in the limit of infinite dilution the velocity of matter approaches unity. In multi-dimensional applications due to the isotropy of the vacuum it is not possible to assign to it a directed, finite velocity. The only possible choice is then $v = 0$ [150].

This setup describes so called Riemann problem which is defined as the initial value problem when the initial data consists of two constant states separated by a membrane and jump discontinuity at $x = 0$. The matter is initially at rest. At $t = 0$ the membrane is removed and left and right states are connected with a rarefaction wave. For such a case an analytic solution exists. This analytic solution was compared with the results from hydrodynamic numeric code. Considering a simple EoS

$$p(\epsilon) = c_s^2 \epsilon, \qquad\qquad c_s^2 = const., \tag{5.3.3}$$

the analytic solution for the energy density can be written as [150]:

$$\epsilon(x,t) = \epsilon_0 \cdot \begin{cases} \left[\frac{1-c_s}{1+c_s}\frac{1-x/t}{1+x/t}\right]^{\frac{1+c_s^2}{2c_s}} & -c_s < x/t \leq 1, \\ 1 & -1 \leq x/t \leq -c_s, \end{cases} \tag{5.3.4}$$

where c_s is the speed of sound in the medium, for ideal ultrarelativistic gas ($\epsilon = 3p$) it is equal to $c_s = \sqrt{\frac{1}{3}}$. The velocity profile as a function of energy density can be expressed as

$$v(\epsilon) = \tanh\left[-\frac{c_s}{1+c_s^2}\ln(\epsilon/\epsilon_0)\right] = \frac{1-(\epsilon/\epsilon_0)^{2c_s/(1+c_s^2)}}{1+(\epsilon/\epsilon_0)^{2c_s/(1+c_s^2)}}. \tag{5.3.5}$$

The pressure can be inferred from the EoS and using thermodynamic relation $dp = sdT = (\epsilon + p)dT/T$ and the EoS we get the temperature $T/T_0 = (\epsilon/\epsilon_0)^{c_s^2/(1+c_s^2)}$.

Our results are compared to the analytic solution of the energy density in one dimension at the time t =5 fm/c for one-dimensional algorithm in Fig. 5.1. It is not surprising that the finer grids lead to a result closer to analytic than coarse ones. We also investigate Riemann problem in two or three dimensions in the next figures.

To confirm that there is no dependence of the simulations on the grid direction (rotational invariance), we rotate the initial discontinuity by 45 degrees in the $x - y$ plane and consider the same rarefaction wave profile propagating in diagonal direction. The results are presented in the Fig. 5.2 together with analytic result and the one-dimensional one.

In a simulation, Courant-Friedrichs-Lewy condition is a necessary condition for the convergence of numerical solution while solving certain partial differential equations. For one-dimensional case it has the following form:

$$C = \frac{u\Delta t}{\Delta x} \leq C_{max}, \tag{5.3.6}$$

where the dimensionless number C is called the Courant number and u is the magnitude of the velocity, usually it is the maximum possible velocity, i.e. speed of light in our case. The value of C_{max} changes with method used to solve discretised equation. In case of SHASTA the Courant number must be less than $C_{max} = 1/2$ to guarantee reasonable results. The comparison of the influence of various Courant numbers onto the result is shown in Fig. 5.3. It can be seen that the more Courant number approaches Courant-Friedrichs-Lewy condition the more accurate the solution will be.

Finally, analytic and numeric velocity profiles are shown in Fig. 5.4 for the relativistic Riemann problem on a one-dimensional grid.

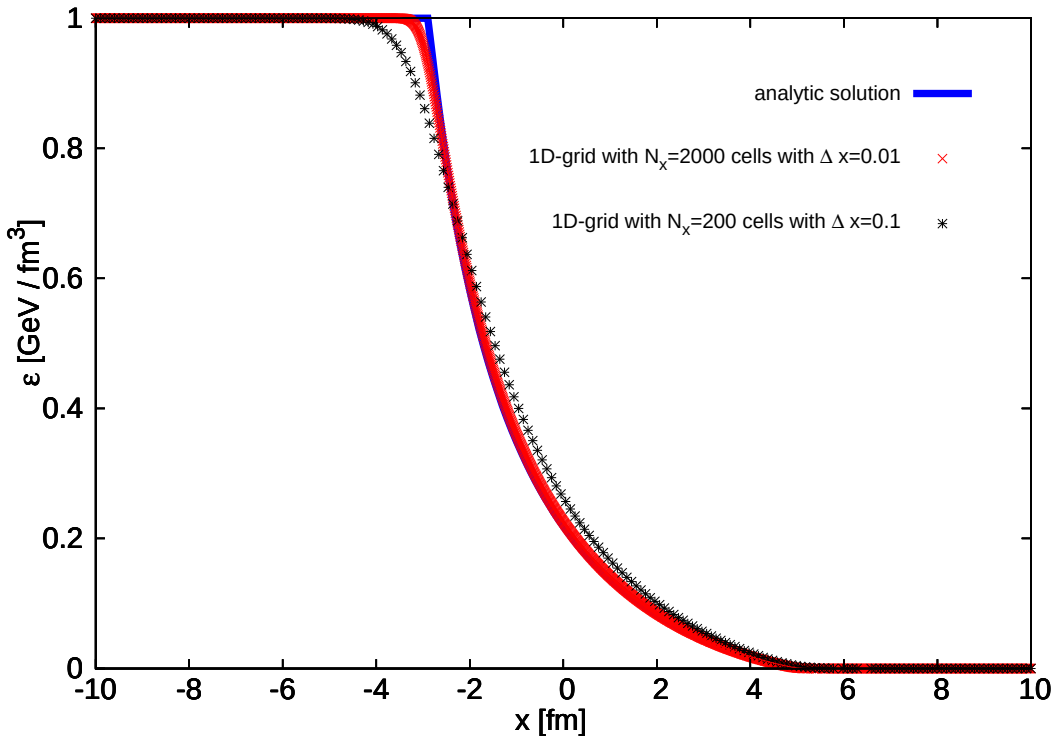

Figure 5.1: Solution of the relativistic Riemann problem on a 1D-grid. Energy density profile at the time t =5 fm/c. Blue squares correspond to analytic solution. Black stars correspond to numerical solution with SHASTA algorithm for 1D-grid with $N_x = 200$ cells with $\Delta x = 0.1$ after $N_t = 125$ time steps. Red line corresponds to numerical solution with SHASTA algorithm for 1D-grid with $N_x = 2000$ cells with $\Delta x = 0.01$ after $N_t = 1250$ time steps.

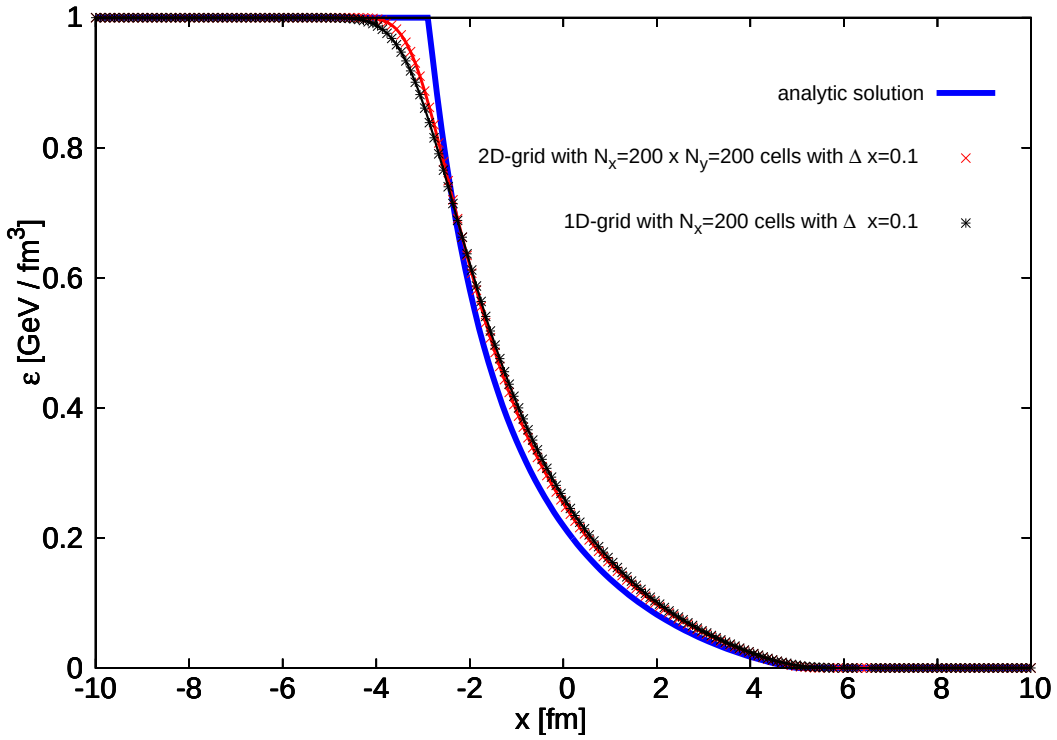

Figure 5.2: Solution of the relativistic Riemann problem on various grids. Energy density profile at the time t =5 fm/c. This figure compares solutions for various space orienations of the Riemann problem. Blue squares correspond to analytic solution. Red line corresponds to numerical solution with SHASTA algorithm for 2D-grid with $N_x = 200 \times N_y = 200$ cells with $\Delta x = 0.1$ after $N_t = 125$ time steps. The original shock front orientation was rotated by 45 degrees. Black stars correspond to numerical solution with SHASTA algorithm for 1D-grid with $N_x = 200$ cells with $\Delta x = 0.1$ after $N_t = 125$ time steps.

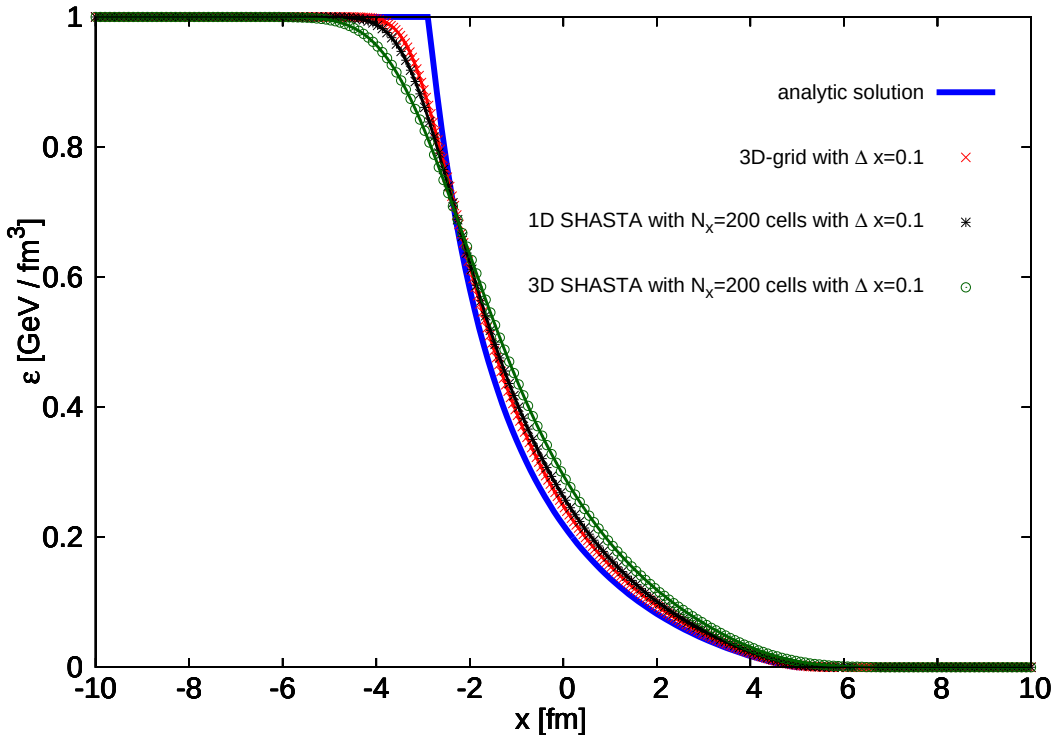

Figure 5.3: Solution of the relativistic Riemann problem on various grids. Energy density profile at the time t =5 fm/c. Comparison of various $\Delta t/\Delta x$ ratios. Blue squares correspond to analytic solution. Black stars corresponds to numerical solution with one-dimensional SHASTA algorithm with $N_x = 200$ cells with $\Delta x = 0.1$ after $N_t = 125$ time steps, $\Delta t/\Delta x = \frac{1}{5}$. Red line correspond to numerical solution with SHASTA algorithm for 3D-grid with $\Delta x = 0.1$ after $N_t = 125$ time steps $\Delta t/\Delta x = \frac{2}{5}$. Green circles, same parameters as black line but calculation was done for 3D-grid.

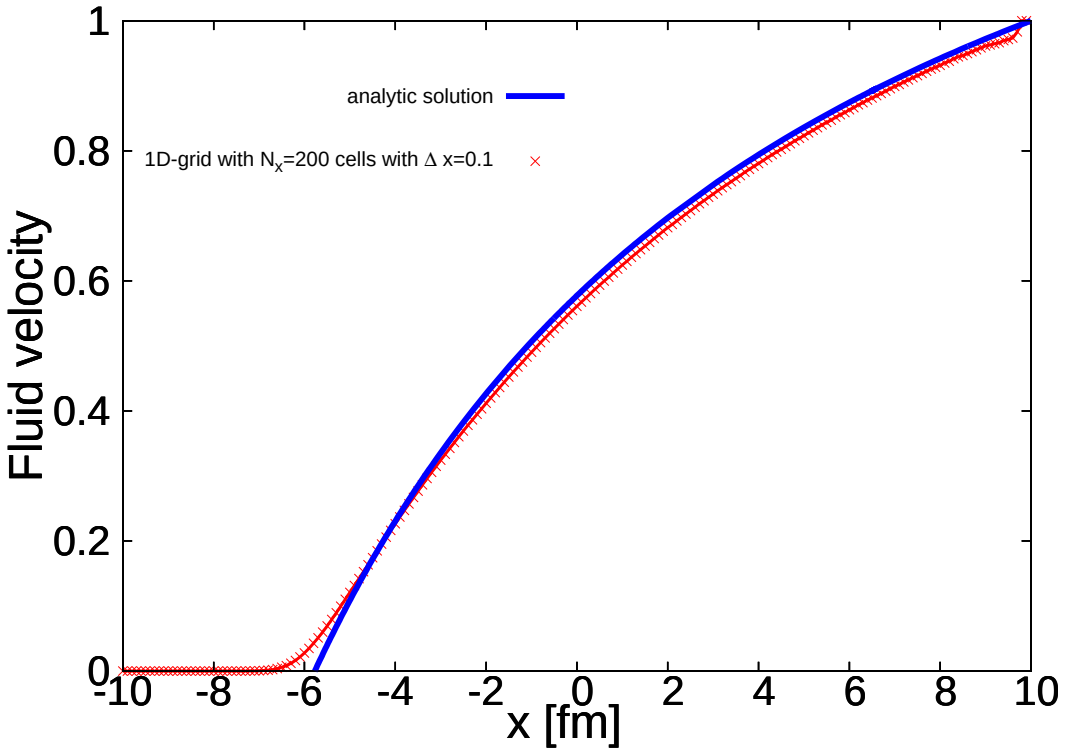

Figure 5.4: Solution of the relativistic Riemann problem on a 1D-grid with $N_x = 200$ cells with $\Delta x = 0.1$. Velocity profile at the time $t = 10$ fm/c after $N_t = 250$ time steps. Blue squares correspond to analytic solution. Red line corresponds to numerical solution with SHASTA algorithm. Courant number used in simulation was set to 0.4.

Chapter 6

Initial conditions for hydrodynamics

Hydrodynamic simulations describe the evolution of strongly interacting system given by initial conditions for the energy-momentum tensor. The hydrodynamic equations of motion require inputs of initial conditions for all their dynamic variables, which are then evolved forward in time. These initial conditions are outside of the framework of hydrodynamic models and have to be determined by other means. Physically, they are determined by the processes during the initial collision of the nuclei and the succeeding stage that makes the system approach to local equilibrium, which is eventually reached at the time τ_0. The equilibration time is a parameter here, since the equilibration mechanisms are still under debate and the first principle determination of the initial conditions of the equilibrated plasma phase has not been achieved [151]. The accurate determination of the initial state of a heavy ion collision is crucial for the determination of bulk properties from a comparison with experimental data.

The initial geometry of the interaction region and its fluctuations strongly affect the generation of flow and the values of all v_n. It is therefore crucial to have a reliable theoretical model for them. Important constraints on the initial-state model can be obtained by comparing all computed v_n coefficients to experimental data simultaneously and studying the event-by-event fluctuations of the flow harmonics.

Different models exist that can generate initial conditions for hydrodynamic simulations. One of the most commonly used models is the Glauber Monte-Carlo model [152]. In this approach the spatial make-up of the nucleus, or its density profile, is modelled by a discrete distribution of nucleons sampled randomly from the charge density distribution function. Two nuclei generated in this way can be separated by a random impact parameter b and the interaction probabilities between the constituent nucleons can be evaluated using the inelastic nucleon cross-section. Nuclear collision in the Glauber Monte-Carlo approach provides in this way not only the size, i.e. the numbers of the participating nucleons and the total number of interactions (each participating nucleon is allowed to interact more than once), but also the shape of the interaction region as the coordinates of the participants are known.

Colour-glass-condensate-inspired initial conditions are becoming increasingly popular. They feature larger eccentricities of the initial energy density profile than Glauber-based models, which has significant implications on elliptic flow [153]. In these models addi-

tional dissipation during the early quark-gluon plasma stage is needed in order to achieve agreement with experiments [153, 154].

This effective theory approximates the description of the fast partons in the wavefunction of a hadron by exploiting the fact that their dynamics is slowed down by Lorentz time dilation, and provides a way to track the evolution of energy of the multigluon states that are relevant in the dense regime. This framework has been applied to a range of reactions at high energy: deep inelastic scattering, proton-nucleus collisions and nucleus-nucleus collisions. At leading order, these calculations correspond to a classical field description of the system. In nucleus-nucleus collisions, this classical field remains coherent for a brief amount of time after the collision, forming a state known as the Glasma. Central question in heavy ion collisions is to understand how these classical fields lose their coherence in order to form a plasma of quarks and gluons in local thermal equilibrium [155].

One of the commonly used colour-glass condensate framework initial state model is the MC-KLN (Monte-Carlo Kharzeev-Levin-Nardi) model [156, 157]. Within this framework, one takes into account the feature of QCD that at small Bjorken-x, a novel regime governed by large gluon densities and non-linear coherence phenomena takes over [158]. The MC-KLN model computes the initial energy-density distributions of the two colliding nuclei, after sampling nucleon positions in a way similar to the MC Glauber model, it needs additional negative binomial fluctuations of multiplicities for a given number of participants in order to be able to describe the measured multiplicity distributions [159].

Other colour-glass condensate models include the string rope model [160] and the pQCD + saturation model [161]. In the latter, the initial time τ_0 is given by the inverse of the saturation scale, which is very small, i.e., $\tau = 0.18$ (0.10) fm/c at RHIC (LHC). Recently, there is a push to implement effects of event-by-event fluctuations in the initial conditions. In the NEXSPHERIO hydro model each event is created by the event generator NeXuS [162]. First, they found that the existence of fluctuations in initial conditions improves the behavior of the elliptic flow as a function of the rapidity in hydrodynamic calculations [163]. They showed that two artificial bumps in the elliptic flow as a function of the rapidity [164] disappear if they take into account initial fluctuations.

Nowadays, most successful initial conditions model is the Colour-Glass-Condensate framework with the impact parameter dependent saturation model combined with the classical Yang-Mills description of initial Glasma fields [165]. The IP-Glasma model is impact parameter dependent saturation model describing transition state between initial quantum state and QGP.

Apart from MC-Glauber and CGC based frameworks, there are several parton- and hadron-cascade models that are being used to determine fluctuating initial conditions. These are for example UrQMD [166] and EPOS [167] all using Monte-Carlo techniques to compute initial particle production and then converting the soft part of the spectrum into the bulk energy density distribution used in hydrodynamic simulations. They also provide initial flow and in principle the full stress-energy tensor including viscous corrections.

In our simulations we have decided to implement simple initial conditions, i.e. smooth optical Glauber model [152] described in the next section. These smooth initial conditions can be advantageous for easy recognition of influence of added fluctuations induced by source terms during the hydrodynamic evolution.

6.1 Optical Glauber model for heavy-ion collisions

In the optical Glauber model it is assumed that at sufficiently high energies, the nucleons will carry sufficient momentum so that they will be undeflected as the nuclei pass through each other. Furthermore, it assumes that the nucleons move independently in the nucleus and also that the size of the nucleus is large compared to the nucleon-nucleon force. The optical form of the Glauber theory does not locate nucleons at specific spatial coordinates. It is based on continuous nucleon density distributions. Before the collision, the density distribution of the two nuclei with mass number A is described by a Woods-Saxon parametrization

$$\rho_A(r) = \frac{\rho_0}{\exp(\frac{r-R_A}{\zeta}) + 1}, \tag{6.1.1}$$

with $R_A = (1.12A^{1/3} - 0.86A^{-1/3})$ fm. In the following we focus on Pb+Pb collisions with $A = 208$ and $\zeta = 0.546$ fm for the surface diffuseness [168]. The normalization factor ρ_0 is set to give $\int d^3r\rho_A(r) = A$. With these parameters we have $\rho_0 = 0.17$ fm^{-3}. The relevant quantity for the following considerations is the nuclear thickness function, which integrates the nuclear density over the longitudinal coordinate z:

$$T_A(x, y) = \int_{-\infty}^{+\infty} dz\rho_A(x, y, z). \tag{6.1.2}$$

The opacity of the nucleus is obtained simply by multiplying the thickness function with the total inelastic cross-section σ_0 of a nucleon-nucleon collision. At $\sqrt{s_{NN}} = 2.76$ TeV we use $\sigma_0 = 62$ mb [169]. Participants are nucleons that interact at least once in the collision.

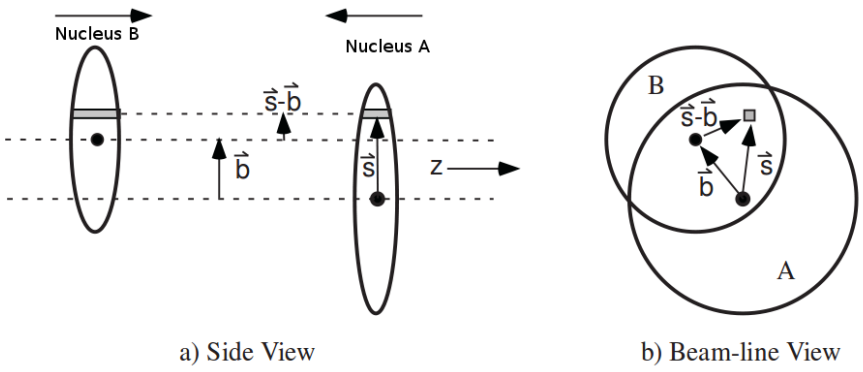

Figure 6.1: Schematic representation of the Optical Glauber Model geometry, with transverse (a) and longitudinal (b) views [152].

Wounded nucleons are those nucleons that interact inelastically. At high energies total cross-section is almost inelastic so number of participants is roughly equal to number of wounded nucleons. Wounded nucleons number is of special interest, as they are thought to be responsible for the bulk of soft particle production and energy deposition in nuclear collisions.

Experiments at SPS found that the number of final state particles scales with the number of wounded nucleons. Deviations from the scaling are observed at RHIC and LHC.

The particle production per wounded nucleon is a function increasing with centrality. This is attributed to a significant contribution from hard processes, scaling with the number of binary collisions. Statistical considerations allow to express the density of wounded nucleons in the transverse plane in terms of the nuclear thickness function of one nucleus multiplied with a combinatorial factor involving the nuclear thickness function of its collision partner. This factor gives the probability that the nucleon interacts at least once [170]. For noncentral collisions of nuclei with mass numbers A and B at impact parameter b, the mean number of wounded nucleons per transverse area is given by [171]

$$n_{WN}(x,y,b) = T_A\left(x+\frac{b}{2},y\right)\left[1-\left(1-\frac{\sigma_0 T_B(x-\frac{b}{2},y)}{B}\right)^B\right] + \\ +T_B\left(x-\frac{b}{2},y\right)\left[1-\left(1-\frac{\sigma_0 T_A(x+\frac{b}{2},y)}{A}\right)^A\right]. \quad (6.1.3)$$

Integrating the above expression over the transverse plane yields the total number of wounded nucleons (participants) as a function of the impact parameter. In reality fluctuations occur, collisions at a certain impact parameter sometimes produce more and sometimes less wounded nucleons as a result of quantum fluctuations - each NN collision ends up differently [172]. In this sense the numbers evaluated in this Glauber formulation [173, 174] can be seen as average numbers of wounded nucleons at fixed impact parameter.

At high energies the density of binary collisions becomes of interest. After suffering their first collision, the partons travel on through the nuclear medium and are eligible for further (hard) collisions with other partons. This leads to the idea that one has to count the binary collisions. The density of their occurence in the transverse plane is simply expressed by the product of the thickness function of one nucleus with the encountered opacity of the other nucleus, leading to

$$n_{BC}(x,y,b) = \sigma_0 T_A(x+b/2,y)T_B(x-b/2,y). \quad (6.1.4)$$

The total number of binary collisions shows a stronger dependence on the impact parameter than does the number of wounded nucleons.

6.2 LHC inspired initial conditions

We assume that the initial state of matter in the transverse plane is governed entirely by the physics of 'soft' and 'hard' processes represented in terms of the densities of wounded nucleons and binary collisions, respectively. Shadowing effects by the spectators do not play a role at LHC energies because the spectators leave the transverse plane at $z = 0$ on a timescale of less than 1 fm/c. We parametrize the shape of the initial energy density distribution in the transverse plane as

$$W(x,y,b) = (1-\alpha)n_{WN}(x,y,b) + \alpha n_{BC}(x,y,b), \quad (6.2.1)$$

where α determines the fraction of the contribution from binary collisions. The α parameter in our simulations was set to 0.16 for LHC. By choosing a smooth transverse

profile with no event-by-event fluctuations we can later be sure that any anisotropic flow in addition to the event-averaged one is due to the contribution of hard partons. We can thus better estimate their contribution. For the longitudinal profile the prescription used in [102, 175, 176, 177, 178, 179, 180] was employed. It is composed of two parts, a flat region around $\eta_s = 0$ and half a Gaussian in the forward and backward direction:

$$H(\eta_s) = \exp\left[-\frac{(|\eta_s| - \eta_{flat}/2)^2}{2\sigma_\eta^2}\theta(|\eta_s| - \eta_{flat}/2)\right]. \tag{6.2.2}$$

We chose $\eta_{flat} = 10$ [181] and σ_η =0.5. The full energy density distribution is then given by:

$$\epsilon(x, y, \eta_s, b) = \epsilon_0 H(\eta_s) W(x, y, b)/W(0, 0, 0). \tag{6.2.3}$$

The energy density in the center was chosen as $\epsilon_0 = 60$ GeV/fm^3 and the initial longitudinal proper time $\tau = 0.55$ fm/c. These parameters and equations suffice only to generate initial conditions for smooth fireball.

This paragraph will describe how hard partons are initiated in our hydrodynamic model. The differential cross-section for gluon production in one nucleon–nucleon collision σ_{NN} was parametrized [182] as

$$E\frac{d\sigma_{NN}}{dp^3} = \frac{1}{2\pi}\frac{1}{p_t}\frac{d\sigma_{NN}}{dp_t dy} = \frac{B}{(1 + p_t/p_0)^n}, \tag{6.2.4}$$

where p_0, B and n are parameters, σ_{NN} is cross-section corresponding to one nucleon-nucleon collision. The parametrization works fine in the p_t interval from 2.5 to 12 GeV/c. Calculated spectra deviate from this parametrization for higher p_t. Note, however, that production of jets at such high p_t is rare and thus does not contribute much to the total yield and can be assumed to have small effect on the bulk when the large number of collisions is analysed. For a simulation at LHC energies we choose $B = 14.7$ mbarn/GeV^2, $p_0 = 6$ GeV, and $n = 9.5$ [182]. The cross-section in a non-central symmetric collision of two nuclei with mass numbers A at the impact parameter b ($b = |b|$) for the production of the leading particle with p_t larger than p_m is then obtained by integrating equation Eq. (6.2.4)

$$\sigma(p_m) = \int_{p_m}^{\infty}\int_{y_{min}}^{y_{max}} \frac{d\sigma_{NN}}{dp_t dy} dp_t dy. \tag{6.2.5}$$

The mean total number of leading particles with $p_t > p_m$ is then

$$N_j(p_m, b) = \frac{A^2 T_{AA}(b)\sigma(p_m)}{1 - (1 - T_{AA}(b)\sigma(p_m))^{A^2}}. \tag{6.2.6}$$

For central collisions of Pb-Pb at 5.5 TeV in center of mass system the mean number of hard partons in simulations was 10. In the last equation we introduced the overlap function

$$T_{AA}(b) = \int_{overlap} T_A(\vec{r}) T_A(\vec{r} - \vec{b}) d^2 r, \qquad T_A(\vec{r}) = 2\rho_0\sqrt{R_A^2 - r^2}, \tag{6.2.7}$$

where the nuclear thickness function $T_A(x)$ is defined in simpler way than in Eq. (6.1.2). The radius of the nucleus is R_A and for the sake of our estimates we have assumed a very simple profile with a constant nuclear density ρ_0.

Jets are produced in pairs which are back to back in the transverse plane (but not longitudinally) so that the total transverse momentum vanishes. The transverse positions at which the jets start moving are distributed according to the density of binary nucleon–nucleon collisions:

$$\rho_b(\vec{r}) = T_A(\vec{r})T_b(\vec{r} - \vec{b}). \tag{6.2.8}$$

Thus, it is more likely to produce a leading parton at the center of the overlapping zone than at its edges. For the presented results only dijet pairs with p_t above 3 GeV were generated.

6.3 Tests for expanding medium

Section 5.3.1 summarized the tests for static medium. This section summarizes tests of our code for expanding medium. In contrast to static case, expanding medium equations were solved in Milne coordinates, Eq. (4.4.14). In all presented cases baryon-free matter is considered. The initial conditions employed were smooth and calculated with the optical Glauber model with LHC-inspired energy density, without any added fluctuations, for details see Chapter 6.2. Unfortunately, for expanding medium with this energy density profile, there is no test case which has an analytic solution. Therefore all existing tests are only numerical. The executed tests follow code verification suggestions in [183] and [184]. Although, the obtained results are EoS dependent, this dependence is weak for state-of-the-art ones because there are little diferences among the results.

The first test examines energy density time evolution of fireball for peripheral collision with impact parameter $b = 7$ fm. Figures 6.2 and 6.3 show energy density profiles in $\eta = 0$ slices for various timesteps. The initial energy density profile in $\eta - x$ plane in $y = 0$ slice together with profile after 4 fm/c of hydrodynamic evolution is shown in Fig. 6.4. For both cases as time follows the energy density in central region is decreasing because the fireball is expanding. The place with the highest energy density is always in the center of the fireball.

In Fig. 6.5 we plot the space-time evolution of isothermal hypersurfaces in $x - \tau$ space for three different temperatures ($T = 120, 150, 164$ MeV) for peripheral collision with impact parameter $b = 7$ fm. As fireball expands, it gradually cools down as plotted. The time evolution of the radial velocity v_t calculated as an average over the transverse plane with the Lorentz contracted energy density $\gamma_t\epsilon$ as weight function is ploted in Fig. 6.6. It can be seen that at later times, the rise of radial velocity slows down. The time evolution of momentum and spatial anisotropies for peripheral event with impact parameter b =7 fm is shown in Fig. 6.7 and Fig. 6.8. The momentum anisotropy ϵ_p, as defined in Eq.(6.4.3), measures the anisotropy of the transverse momentum density due to anisotropies in the collective flow pattern. The effects of pressure gradient anisotropies are reflected in the initial growth rate of the flow-induced momentum anisotropy ϵ_p. At later times the buildup of momentum eccentricity slows down. Spatial anisotropy ϵ_x as defined in Eq.(6.4.1) is calculated by averaging over the transverse plane with the energy density ϵ as weight function. If $\epsilon_x > 0$, the energy density drops more quickly in the x-direction than in the y-direction because the overlap region is shaped elliptically. Using

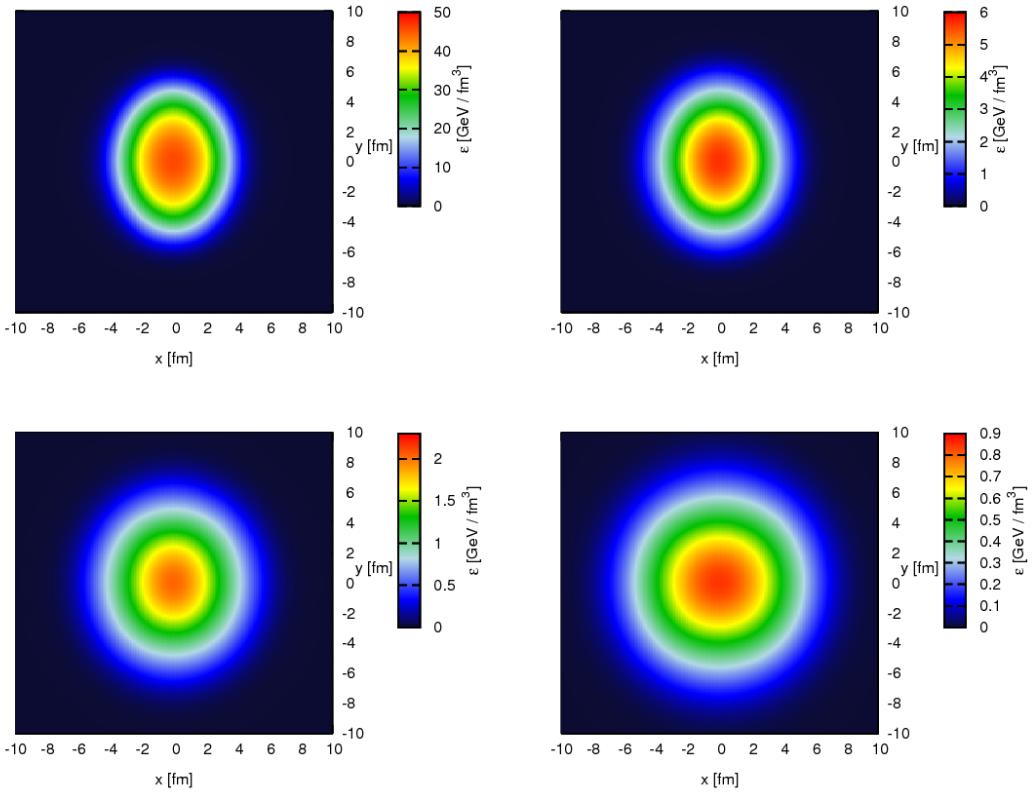

Figure 6.2: Hydrodynamic evolution of event with impact parameter $b = 7$ fm. Energy density transverse slices are shown for rapidity $\eta = 0$. First profile is taken after time $t = 0.55$ fm/c. Each other profile is taken after time $\Delta t = 2$ fm/c from previous profile. Initial conditions were calculated using optical Glauber model with rapidity density given by Eq.(6.2.2). Initial energy density ϵ was set to $\epsilon(0, 0, 0)$=60.0 GeV/fm^3. Note that colour scales are different in each time step. Also note that Figure hydrodynamic evolution continues in Fig. 6.3.

an EoS $p = p(\epsilon)$, this implies that the mean pressure gradients are unequal, $\partial_x p > \partial_y p$, and according to the hydrodynamic equations one expects a larger fluid velocity to build up in the x-direction than in the y-direction. At later times the change of decrease of spatial anisotropy ϵ_x slows down. The spatial anisotropy even becomes negative as in scenario presented in [185].

Figure 6.9 shows deviation from the Bjorken scaling [186] (2+1-dimensional boost-invariant hydrodynamics) for our numerical code. Due to the transverse expansion, calculated energy density (red crosses) falls faster than Bjorken scaling solution (blue line). For comparison we show also the energy density evolution at the fireball periphery (black squares). It can be concluded that all of our results testing hydrodynamic evolution are not in contradiction with numerical results presented in [183] and [184].

Finally, we discuss our results for measurable observables after freeze-out process. Figure 6.10 shows p_T spectra for various charged particles for LHC inspired IC at impact parameter b=0 fm. Similarly, Figure 6.11 shows pseudorapidity distribution of various charged species for LHC inspired IC at impact parameter b=0 fm. The number of charged

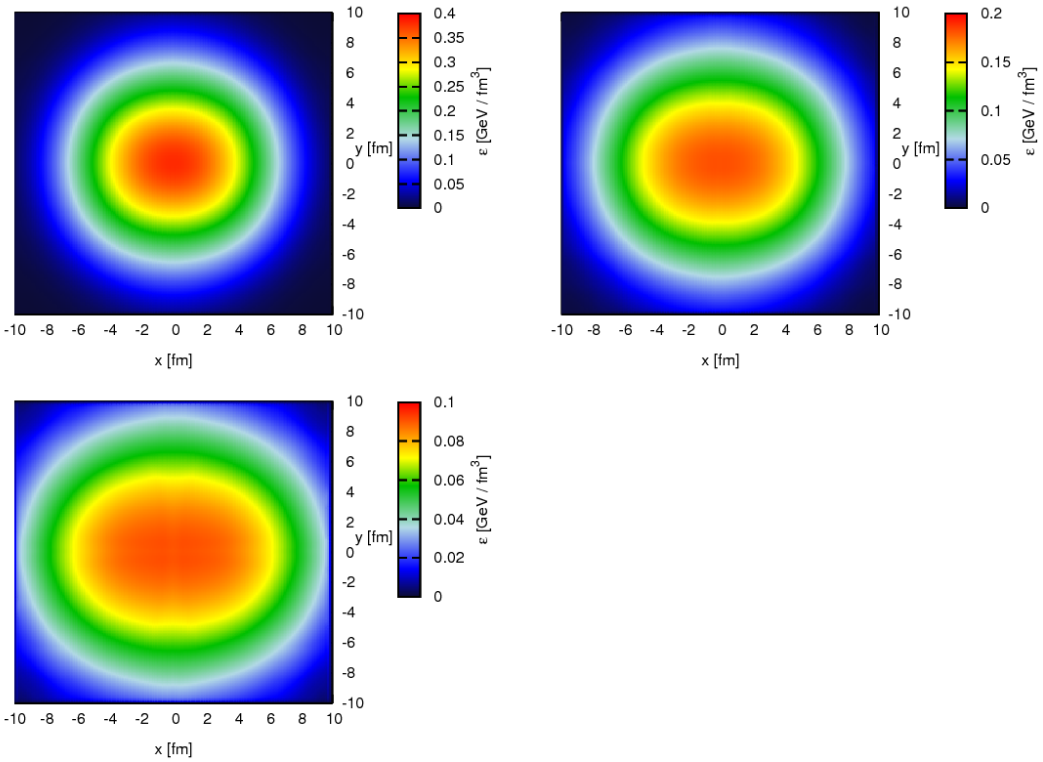

Figure 6.3: Continuation of previous Figure 6.2.

particles can be varied by changing the value of ϵ_0. Higher ϵ_0 gives higher charged particle multiplicity and vice versa. By tuning of hydrodynamic simulation parameters, one can achieve multiplicities and p_T spectra similar to those at LHC and compare results of anisotropic flow obtained with tuned parameters. However, we do not compare our results with LHC results since our goal is only to illustrate that our scenario works and can significantly contribute to the anisotropic flow. Since LHC results are also influenced by fluctuations and dissipation, disentangling the exact effect of our model would not be possible.

6.4 Initial fluctuation characterization

The physics of the initial stages of a heavy-ion collision is currently one of the biggest open questions, and is one of the largest contributions of uncertainty for many observables. The fundamental question is how the initial state of two ultrarelativistic nuclei before the collision evolves into a system that can eventually be described by hydrodynamics. Reliable first-principles calculations from non-equilibrium quantum chromodynamics are not yet possible, so the current state-of-the-art is to construct models, based on what we know about the relevant physics, and constrained by agreement with data after subsequent fluid / transport evolution. For many years, most of hydrodynamic calculations used smooth and symmetric initial density profiles to simulate an average collision. In reality, there are quantum fluctuations in the earliest stages of the collision, that come from

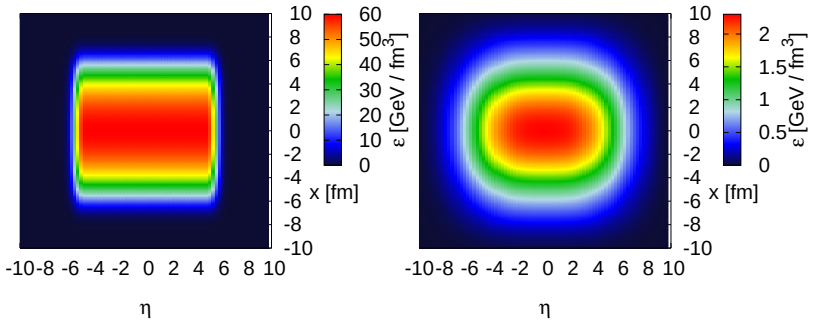

Figure 6.4: Energy density slices for ultracentral event are shown in $\eta - x$ plane under the condition $y = 0$. First profile is taken after time $t = 0.55$ fm/c. Second profile is taken after time $\Delta t = 4$ fm/c from previous profile. Initial conditions were calculated using optical Glauber model. Initial energy density ϵ was set to $\epsilon(0, 0, 0)$=60.0 GeV/fm^3.

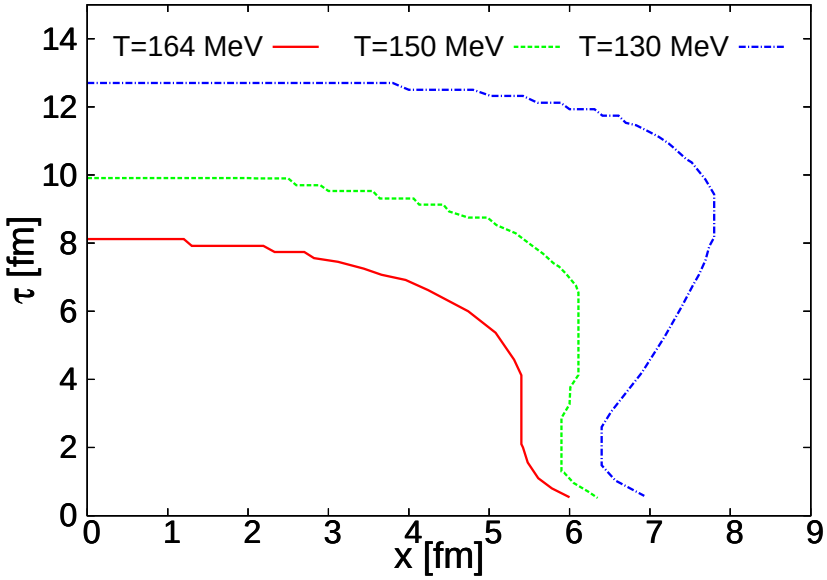

Figure 6.5: Contours of constant temperature $T = 130$ MeV (blue x's), T=150 MeV (red triangles) and T=164 MeV (black crosses) in the $x-\tau$ plane at (y,η) = (0,0) for peripheral collision with impact parameter $b = 7$ fm.

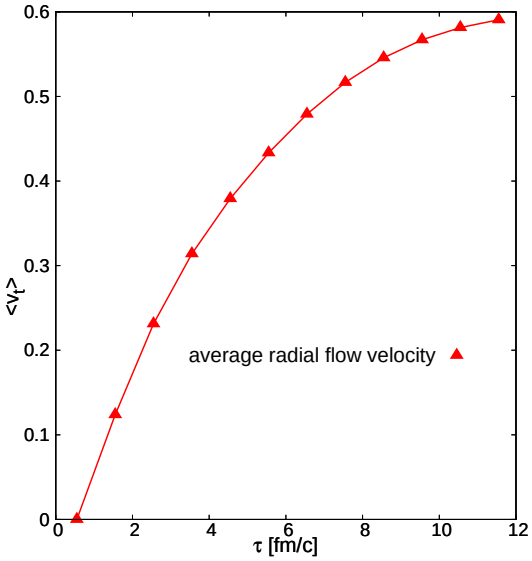

Figure 6.6: Time evolution of the average radial flow velocity $\langle v_t \rangle$ in event with impact parameter $b = 7$ fm.

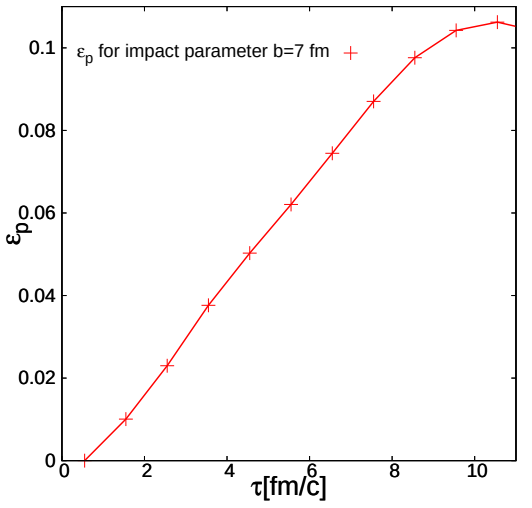

Figure 6.7: Time evolution of the momentum anisotropy ϵ_p, as defined in (6.4.3), in event with impact parameter $b = 7$ fm.

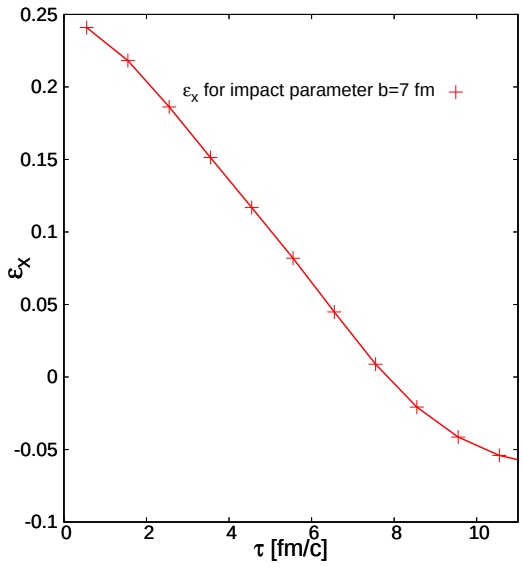

Figure 6.8: Time evolution for the spatial eccentricity ϵ_x, as defined in (6.4.1), calculated for event with impact parameter $b = 7$ fm.

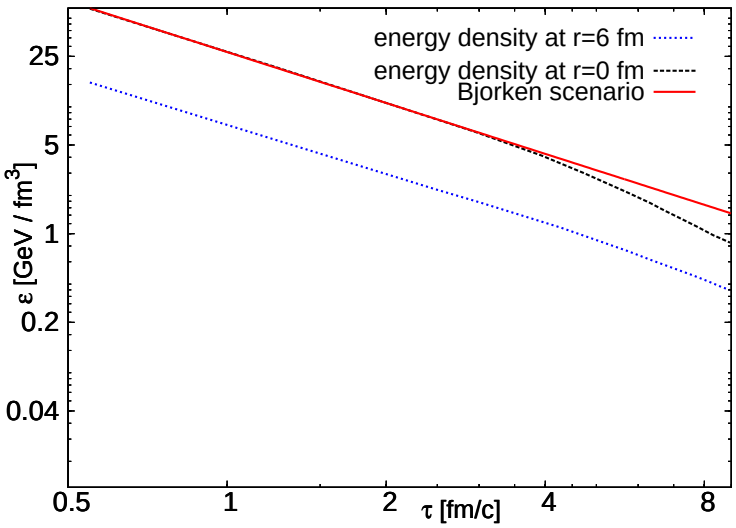

Figure 6.9: Time evolution of the energy density in central event on log-log scale. Red crosses correspond to the calculated energy density for the center of the fireball ($r = 0$ fm). Black squares corespond to the calculated energy density for the edge of the fireball ($r = 6$ fm). Blue line corresponds to Bjorken scaling solution for the center of the fireball.

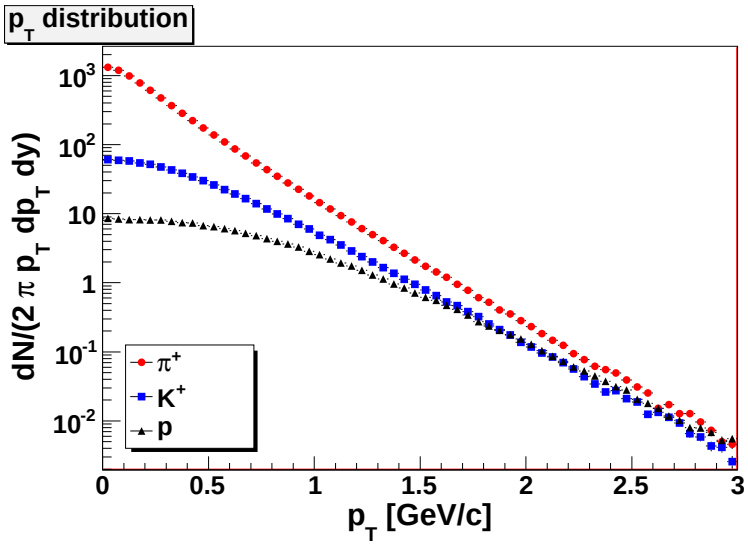

Figure 6.10: p_t distribution of various charged species for LHC inspired IC at b=0 fm.

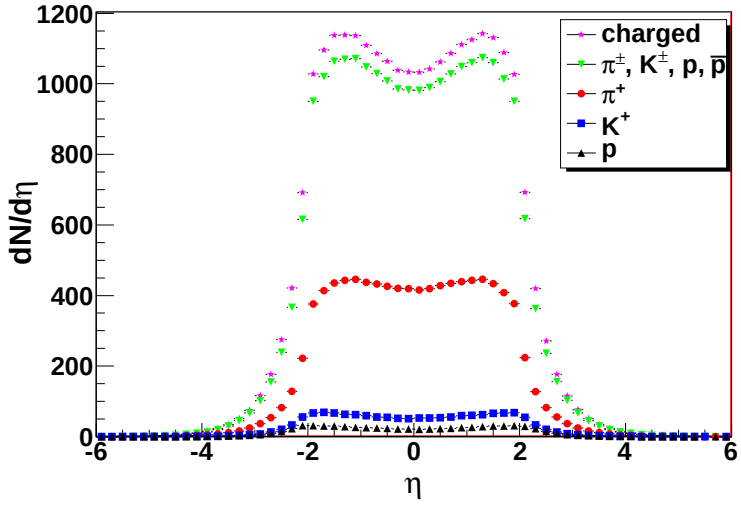

Figure 6.11: Pseudorapidity distribution of various charged species for LHC inspired IC at impact parameter b=0 fm.

sources as nucleonic structure of the nucleus. This causes the energy density at early times to be lumpy and asymmetric, and to fluctuate from one collision event to the next, even for nuclei colliding at a fixed impact parameter.

In peripheral collisions the overlap region in the plane transverse to the beam direction has an ellipsoidal shape. This spatial anisotropy can be quantified by the spatial eccentricity [187]

$$\epsilon_x = \frac{\{y^2 - x^2\}}{\{y^2 + x^2\}}, \tag{6.4.1}$$

where curly brackets indicate an average over the energy density ϵ of the system at an early stage of the collision

$$\{...\} = \frac{\int d^3x \epsilon(x)...}{\int d^3x \epsilon(x)}. \tag{6.4.2}$$

Momentum anisotropy of the system is defined as

$$\epsilon_p = \frac{\langle T^{xx} - T^{yy} \rangle}{\langle T^{xx} + T^{yy} \rangle}, \tag{6.4.3}$$

where T^{xx} and T^{yy} are the diagonal transverse components of the energy-momentum tensor and the averaging is over the transverse plane. This initial coordinate anisotropy is converted to a final state momentum space anisotropy, if large enough collective pressure gradients drive the evolution of the system.

In 2005, collisions of smaller nuclei Cu+Cu were carried out at RHIC. Using the standard definitions given above for the elliptic flow and the eccentricity, the ratio of v_2/ϵ_2 was surprisingly much higher than previously observed in Au+Au collisions, and the elliptic flow did not appear to vanish as the collisions became more central. The resolution of this puzzle was that fluctuations in the initial state geometry are important, and are naturally more pronounced in smaller systems such as the Cu+Cu collision system and for central collisions, where the average standard eccentricity is small. Further, the relevant spatial eccentricity that drives elliptic flow is not the standard eccentricity above, which is defined with respect to the impact parameter of the incoming nuclei, but an eccentricity with respect to a plane defined by the participating nucleons (the "participant plane"), which can be rotated in a different direction. By using a new generalized definition of the participant eccentricity given by the expression

$$\epsilon_{part} = \frac{\sqrt{(\{y^2\} - \{x^2\})^2 + 4\{xy\}^2}}{\{y^2\} + \{x^2\}}, \tag{6.4.4}$$

defined with respect to a coordinate system where $\{x\} = \{y\} = 0$, it became clear that the elliptic flow results in Cu+Cu collisions were completely consistent with the previous larger systems in a hydrodynamic picture [188]. This was the first piece of direct evidence of initial state fluctuations.

Nowadays, it is common to characterize initial transverse density profiles with generalizations of the participant eccentricity (6.4.4), with strength ϵ_n and orientation Φ_n that

can be compactly written as the magnitude and phase of a complex number:

$$\epsilon_n e^{in\Phi_n} \equiv -\frac{\{r^n e^{in\Phi}\}}{\{r^n\}}; n \geq 2 \tag{6.4.5}$$

$$\epsilon_1 e^{i\Phi_1} \equiv -\frac{\{r^3 e^{i\Phi}\}}{\{r^3\}}, n = 1, \tag{6.4.6}$$

where r and Φ are the polar coordinates in the transverse plane and the curly brackets average over the initial transverse energy density.

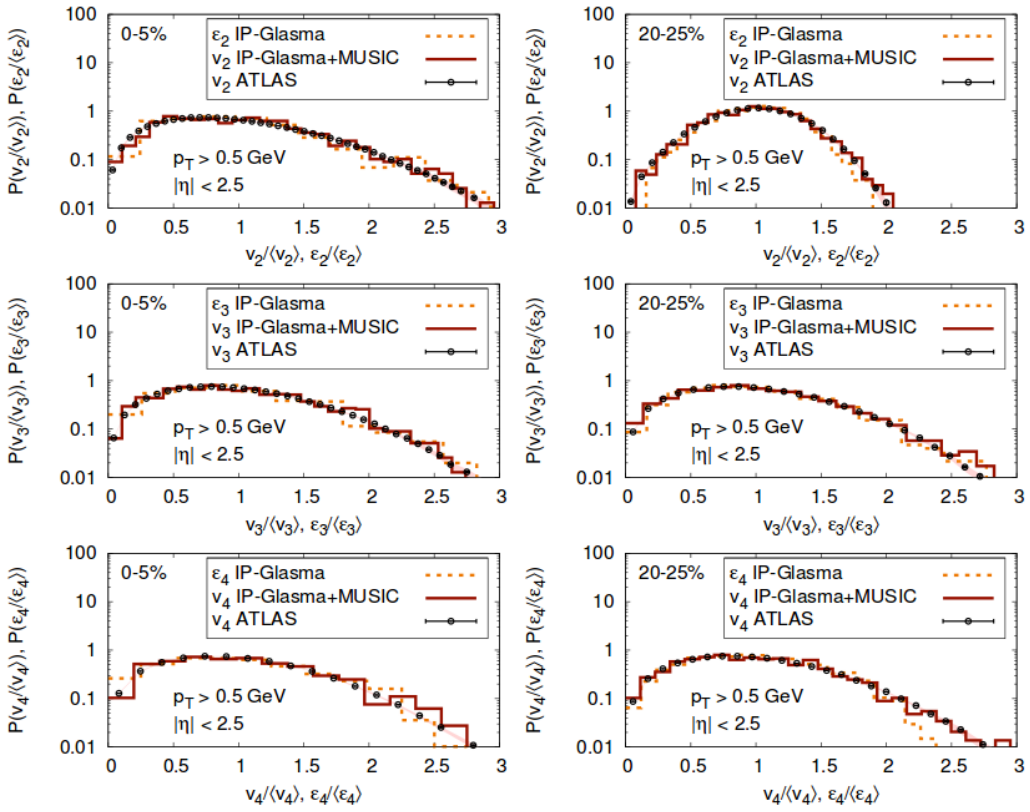

Figure 6.12: Scaled distributions of v_2, v_3 and v_4 from hydrodynamic simulations using IP-Glasma model [65] initial conditions as well as ϵ_2, ϵ_3 and ϵ_4 from the IP-Glasma model [65] compared to experimental data from the ATLAS collaboration [189, 190]. There were 750 (0-5%) and 1300 (20-25%) events in theoretical simulation. Bands are systematic experimental errors. Figure taken from [65].

It is known that the event-averaged v_2 and the eccentricity of the averaged initial state, ϵ_2 are approximately linearly related. Similar relation has been found for ϵ_3 and the average v_3 but not for ϵ_4 and v_4 [191] and [192]. In addition, we can study similar relations event-by-event by evaluating the linear correlation between the harmonics v_n and ϵ_n. It reveals that the second and third Fourier coefficients have a strong linear correlation to the initial geometry of the collision. While the event-averaged Fourier coefficients, $\langle v_n \rangle_{ev}, n = 2, 3$, and 4, are sensitive to the details of the fluid-dynamical evolution, their relative fluctuations, $\delta v_n = (v_n - \langle v_n \rangle_{ev})$, are determined solely by the

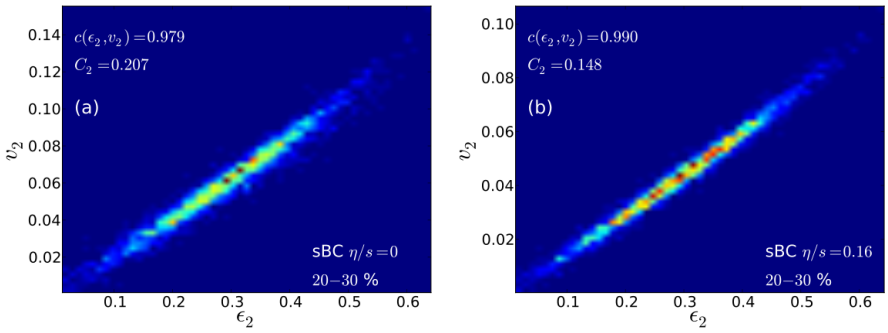

Figure 6.13: 2D histogram of event-by-event values of v_2 and ϵ_2, showing strong correlation between the two quantities, which increases with viscosity (taken from [45]).

fluctuations of the corresponding initial state anisotropy coefficients, with basically no sensitivity to the viscosity of the fluid. This makes the distribution of δv_n, a direct probe of the initial condition of a heavy-ion collision, providing a direct and clean measurement of the distribution of the relative fluctuations of the initial anisotropy,

$$P(\delta v_n) \approx P(\delta \epsilon_n), n = 2, 3, 4. \tag{6.4.7}$$

This relation is true even for the relative fluctuations of v_4, even though v_4 itself is not linearly correlated to ϵ_4 [45]. Figure 6.13 shows 2D histogram of event-by-event values of v_2 and ϵ_2 in the 0-5 % centrality class from hydrodynamic simulations [45].

At the least, the study of ultra-central collisions can constrain the possible fluctuations implemented in different models by comparison to experimental data. A way to constrain initial state models with fluctuations is the study of event-by-event distributions of flow harmonics v_n, which have recently been determined experimentally [190]. It was found [45] that these distributions are almost independent of the details of the hydrodynamic evolution, like the shear viscosity to entropy density ratio. In fact, the distributions of initial eccentricities provide already an excellent approximation of the measured v_n distributions when scaled by the mean value. This allows for an almost model independent determination of the initial state and the transport properties of the evolving system. As shown in Fig. 6.12 the IP-Glasma model provides a very good description of these probability distributions [65] and differences between the ϵ_n and v_n distributions are only visible in the tail where nonlinear effects in the hydrodynamic evolution are potentially more important. They also found that $< v_n >$ scales with participant eccentricity strength $< \epsilon_n >$ and even that this scaling is valid for whole distributions of $< v_n >$ and $< \epsilon_n >$.

In comparison to the results in the literature, the simulations presented in this thesis show that the anisotropy can rise during the hydrodynamic evolution, thus our mechanism can break this linear correlation.

Despite the large effort that is made in understanding the initial conditions in terms of parametrizations and dynamical models, it is important to concentrate on the goal to quantify the amount of initial state fluctuations that is associated with the early stage non-equilibrium QCD evolution of two colliding nuclei. Even though the hydrodynamic description of the hot and dense stage of heavy ion collisions seems to work very well,

one of the big open questions in the field is how the system thermalizes rapidly. Whatever the process for thermalization actually is, it is likely that it will have an impact on initial state fluctuations. Initial non-trivial flow velocity fields have not yet been studied in a comprehensive fashion. There are certainly non-zero initial angular momentum and vorticity in the system, but how they should be treated and what impact they have on observables is not obvious. The intrinsic relationship between space and momentum in quantum physics through the uncertainty principle has potential implications for momentum anisotropy in heavy-ion collisions. Using a harmonic oscillator potential the calculated elliptic anisotropy was found to be sizeable compared to elliptic flow measurements in nuclear collisions [139]. These results question the validity of the completely hydrodynamic interpretation of anisotropic flow data, and highlight the importance of including quantum physics in hydrodynamic calculations which has largely been neglected so far.

6.5 State-of-the-art initial conditions

Although not included in our simulations, for broader overview this section is dedicated to the two most used state-of-the-art approaches in generating initial conditions. The first part concerns often used Glauber Monte Carlo approach. The second part includes a description of the fluctuating glasma initial conditions which is the newest approach.

6.5.1 Glauber Monte Carlo approach

The advantages of the Monte Carlo approach for the calculation of geometry related quantities like $\langle N_{part} \rangle$ and $\langle N_{coll} \rangle$ are: its simplicity and ability to include various fluctuations and correlations. Moreover, it is possible to simulate experimentally observable quantities like the charged particle multiplicity and to apply similar centrality cuts as in the analysis of real data. In the Monte Carlo ansatz the two colliding nuclei are assembled in the computer by distributing the A nucleons of nucleus A and B nucleons of nucleus B in three-dimensional coordinate system according to the respective nuclear density distribution. A random impact parameter b is then drawn from the distribution $d\sigma/db \sim 2\pi b$. A nucleus-nucleus collision is in simplest approach treated as a sequence of independent binary nucleon-nucleon collisions, i.e., the nucleons travel on straight-line trajectories and the inelastic nucleon-nucleon cross-section is assumed to be independent of the number of collisions a nucleon underwent before [152]. In the simplest version of the Monte Carlo approach a nucleon-nucleon collision takes place if their distance d in the plane orthogonal to the beam axis satisfies

$$d \leq \sqrt{\sigma_{inel}^{NN}/\pi}, \tag{6.5.1}$$

where σ_{inel}^{NN} is the total inelastic nucleon-nucleon cross-section at a given collision energy.

Instead of the hard-sphere method, one may use a smooth Gaussian function to determine the probability distribution of wounded nucleons or a binary collision.

6.5.2 Fluctuating glasma initial conditions

A more recent improved colour-glass-condensate based approach is the IP-Glasma model [193, 194], which combines the IP-Sat (Impact Parameter dependent Saturation Model) model [195, 196] of high energy nucleon (and nuclear) wavefunctions with the classical Yang-Mills (CYM) dynamics of the glasma fields produced in a heavy-ion collision [197, 198, 199, 200, 201, 202]. After fixing the free parameters of the IP-Sat model by fits to small x HERA deeply inelastic scattering (DIS) data of protons and fixed target nuclear DIS data [203, 204], the IP-Sat model provides an excellent description of these data. The IP-Glasma model includes fluctuations of nucleon positions as well as sub-nucleonic fluctuations of colour charges, a feature missing in most other initial state models. Another advantage is that the model does not rely on k_T-factorization, which is strictly valid only when at least one of the sources is dilute (as in $p + p$ and $p + A$ collisions). Furthermore, IP-Glasma includes non-linear pre-equilibrium evolution of the initial gluon fields. This leads to the build-up of initial flow and an independence from the exact time when one switches to hydrodynamics [65].

The early stage dynamics is however not fully included. Instabilities triggered by quantum fluctuations, and subsequent strong scattering of over-occupied fields, may lead to rapid isotropization and quenching of viscous stress tensor $\Pi^{\mu\nu}$ to reasonable values justifying the use of viscous hydrodynamics already at early times. This unstable dynamics requires a full 3+1 dimensional simulation including realistic description of quantum fluctuations, which has not yet been fully achieved. However, significant progress is being made [206, 207, 208, 209] and the IP-Glasma model can be extended to include these important effects. Matching of the full stress-energy tensor, including viscous corrections and flow, to the hydrodynamic simulation will then be possible.

In Fig. 6.14 there is a comparison of initial energy densities from an MC-Glauber, the MC-KLN and the IP-Glasma model using the same distribution of nucleons in the incoming nuclei. In the MC-Glauber model every wounded nucleon was assigned a two-dimensional Gaussian energy density with a width of σ_0=0.4 fm. The MC-KLN result was obtained using the publicly available code MCKLN-3.52 [211]. IP-Glasma results are shown for two different times, $\tau = 0.01$ fm/c and $\tau = 0.2$ fm/c after Yang-Mills evolution. The evolution smoothens the initially very distinct structures noticeably. Because of the additional subnucleonic fluctuations, the IP-Glasma model produces the finest granularity, typically leading to larger fluctuation driven odd eccentricities [193, 194]. Simulations using the IP-Glasma initial state model have been particularly successful in describing both the p_T dependent and integrated v_n at both RHIC and LHC energies [65]. The agreement with experimental results from the LHC shown in Figures 6.15, 6.16 and 6.17 is particularly striking. This agreement indicates that initial state fluctuations in the deposited energy density, translated by hydrodynamic evolution into anisotropies in the particle production, are the main ingredient to explain the measured flow coefficients. This is also indicated by correlation of initial state anisotropy with anisotropy of hadron distribution. However, our mechanism can generate anisotropies during hydrodynamic evolution. This implies that we would need different initial conditions to explain measured flow coefficients.

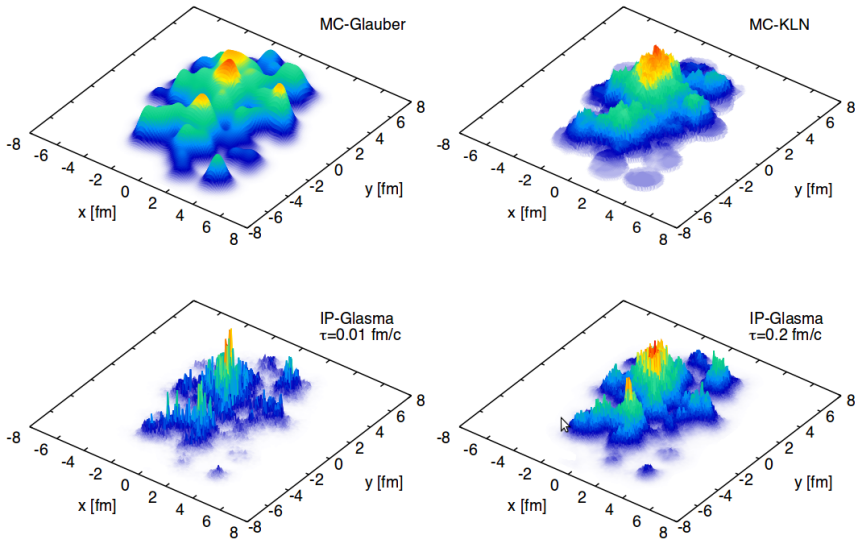

Figure 6.14: Comparison of the initial energy density profiles (arbitrary units) produced by the MC-Glauber, MC-KLN and IP-Glasma models. All events have the same configuration of nucleons and impact parameter $b = 4$ fm to emphasize how different model descriptions affect the structure of the energy density. The spikiest structure is obtained in the IP-Glasma model, which includes subnucleonic colour charge fluctuations. Yang-Mills evolution to $\tau = 0.2$ fm/c smoothens this structure before it enters a hydrodynamic simulation [193, 205]. Still it is interesting that IP-Glasma yields the spikiest profile even after this time. Energy density is in arbitrary units.

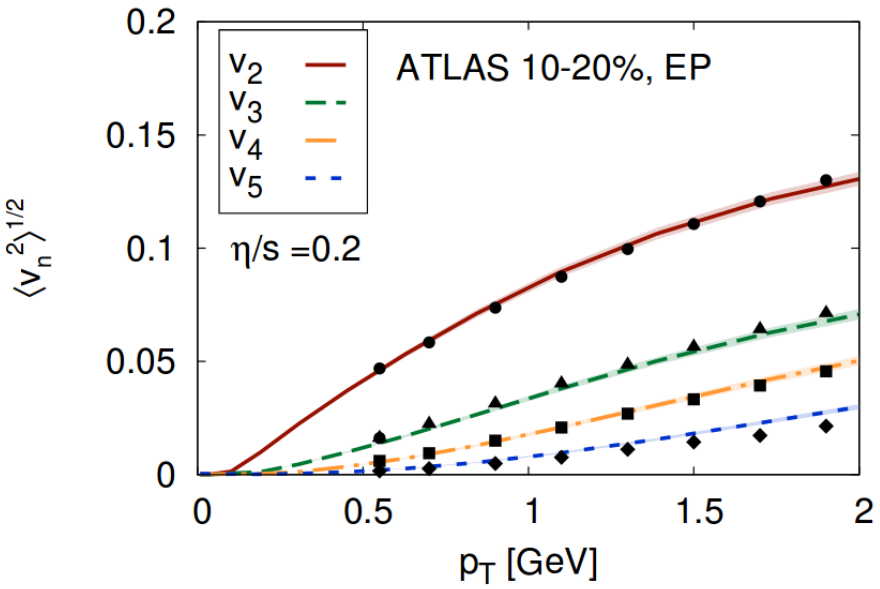

Figure 6.15: Root-mean-square anisotropic flow coefficients $< v_n^2 >^{1/2}$ as functions of transverse momentum, compared to experimental data by the ATLAS collaboration using the event plane (EP) method [210] (points). Bands indicate statistical errors. Experimental error bars are smaller than the size of the points. Lines represent results from hydrodynamic simulations with IP-glasma initial conditions [65]. Figure taken from [65].

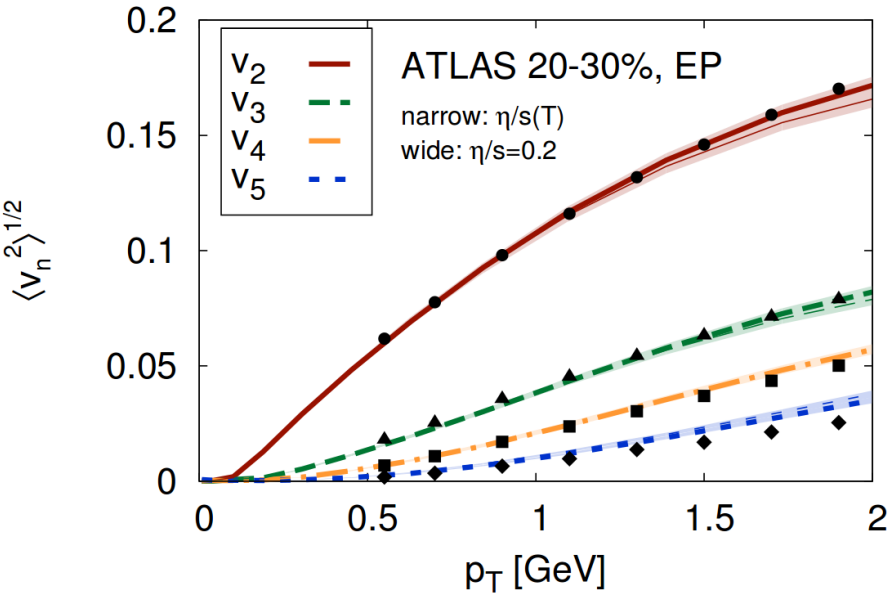

Figure 6.16: Comparison of $v_n(p_t)$ using constant $\eta/s = 0.2$ and a temperature dependent $\eta/s(T)$ as parametrized in [212]. Experimental data by the ATLAS collaboration using the event-plane (EP) method [210] (points). Bands indicate statistical errors. Lines represent results from hydrodynamic simulations with IP-glasma initial conditions [65]. Figure taken from [65].

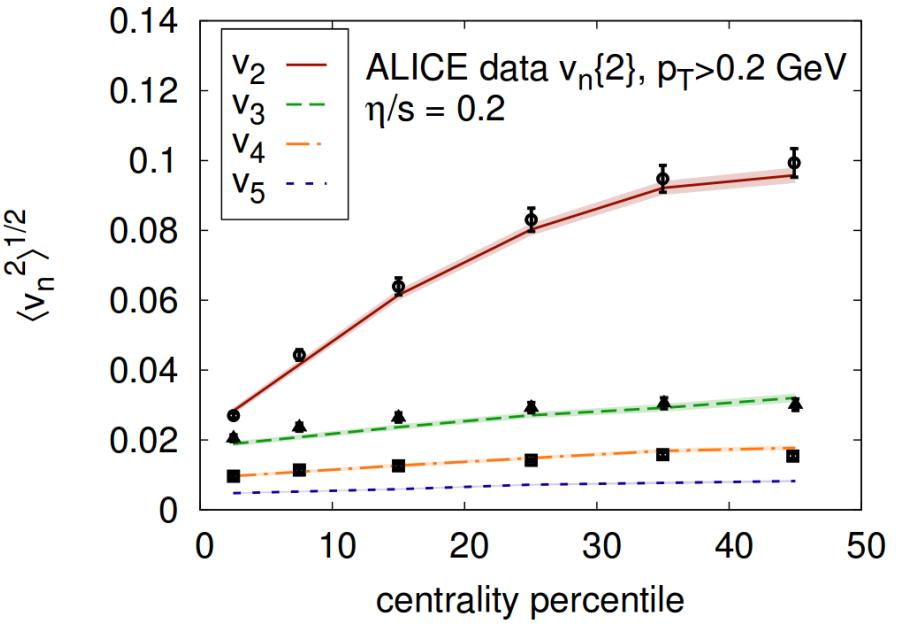

Figure 6.17: Root-mean-square anisotropic flow coefficients $< v_n^2 >^{1/2}$, computed as a function of centrality, compared to experimental data of $v_n\{2\}, n \in \{2, 3, 4\}$, by the ALICE collaboration [213] (points). Lines represent results from hydrodynamic simulations with IP-glasma initial conditions [65]. Hydrodynamic results are calculated with 200 events per centrality, with bands indicating statistical errors [65]. Figure taken from [65].

Chapter 7

Jet energy loss

A fast moving hard parton interacts with the medium while moving through the plasma and loses energy. Generally, the mechanism by which this energy is lost as well as the amount of energy deposited depends on the particle and matter properties. This provides fundamental information about the medium itself. Therefore such jet-medium interactions are significant for the study of a parton moving through plasma, the evolution of jets and its impact on the measured particle distributions. The crucial part for the study of the evolution of jets in heavy-ion collisions is the source term describing the energy and momentum lost by the hard partons which thermalize in the medium. A lot of interesting experimental results which suggest the existence of very large jet energy loss are reported [214, 215]. To explain these results interaction between jets and medium needs to be understood. The leading particle emits a significant number of partons which promptly evolve via multiple branching and thus degrade into a myriad of soft gluons, with energies of the order of the medium temperature T. Via elastic collisions with the medium constituents, these soft gluons relax to local thermal equilibrium with the plasma over a time scale which is considerably shorter than the typical lifetime of a mini-jet. The thermalized gluons form a tail which lags behind the hard components of the jet. Together with the background QGP, they behave hydrodynamically [216].

Four major phenomenological approaches have been developed to connect the QCD energy loss calculations with the experimental observables. Important is the fact that they examine the evolution of the jet, not plasma, which is crucial for us. These are based on perturbative QCD approaches: the higher twist (HT) formalism [217], the AMY (Arnold-Moore-Yaffe) formalism [218], the GLV (Gyulassy-Levai-Vitev) formalism [219] and BDMPS (Baier-Dokshitzer-Mueller-Peigne-Schiff) formalism [220] / ASW (Armesto-Salgado-Wiedemann) formalism [221]. Despite the large amount of effort put into the development of perturbative description of the hadron production in heavy-ion collisions, there are uncertainties remaining about the exact nature of jet-medium interactions in the kinematic and temperature regimes relevant at RHIC or LHC. As a whole, the above four approaches describe RHIC data well, but they offer very different quantitative conclusions about the quenching strength. This does not come as a big surprise since the approaches differ in some of their basic assumptions, and there are large uncertainties in modeling hard probes beyond the calculation of the energy loss rate for a quark or gluon. The nuclear modification factor R_{AA} measured at the Large Hadron Collider (LHC) [34, 33] indicates

that the jet-medium coupling is reduced as compared to fixed-coupling extrapolations [222] based on the data from RHIC [223]. Thus, those models constrained to RHIC data [222] tend to overquench at LHC energies, leading to a larger jet suppression than measured.

Recently, attempts to reformulate parton energy loss as a medium modification of the perturbative evolution of the fragmentation functions have been implemented in Monte Carlo models [224, 225]. Such MC approaches allow one to address more detailed experimental observables such as the particle and the energy flows within a jet. The following section describes basic introduction to QCD based approaches mentioned in the previous paragraph. The next section concerns the implementation of the energy loss in three-dimensional relativistic hydrodynamics.

7.1 Basics of perturbative QCD based approaches

The use of fast partons as calibrated tomographic probes of hot and dense QCD matter in heavy-ion collisions relies on the possibility to compute theoretically their perturbative production cross sections and their modifications suffered while propagating through a strongly interacting medium. The energy loss formalisms discussed above can be roughly divided into two groups: those calculating the radiated gluon spectrum, i.e. the energy lost by the initial parton (GLV and BDMPS/ASW) and those determining directly the change in the final distribution of the traversing partons (HT and AMY).

All schemes utilize a factorized approach where the final cross section σ to produce a hadron h with transverse momentum p_t (within rapidity y and $y + dy$) may be expressed as a convolution of initial nuclear structure functions to produce partons with momentum fractions x_a, x_b, $(G_a^A(x_a), G_b^B(x_b))$, a hard partonic cross section to produce a high transverse momentum parton c with a transverse momentum $\hat{p}$ and a medium modified fragmentation function for the final hadron $(\bar{D}_c^h(z))$,

$$\frac{d^2\sigma^h}{dyd^2p_t} = \frac{1}{\pi}\int dx_a \int dx_b G_a^A(x_a) G_b^B(x_b) \times \frac{d\sigma_{ab\to cX}}{d\hat{t}} \frac{\bar{D}_c^h(z)}{z}. \tag{7.1.1}$$

In the vicinity of midrapidity applies $z = p_t/\hat{p}$ and $\hat{t} = (\hat{p} - x_a P)^2$, where P is the average incoming momentum of a nucleon in nucleus A.

The origin of the higher twist approximation scheme lies in the calculations of medium enhanced higher twist corrections to the total cross section in Deep-Inelastic Scattering off large nuclei [226]. One re-sums power corrections to the leading twist cross sections, which, though suppressed by powers of the hard scale Q^2, are enhanced by the length of the medium. This technology of identifying and isolating power corrections is used to compute the n-hadron inclusive cross-section. One assumes a hierarchy of scales $E \gg Q \gg \mu$, where μ is momentum scale of the medium, and applies this to the computation of multiple Feynman diagrams. A disadvantage of this approach is the negligence of the quark structure function in the medium: as a result, collisions with the medium may not change the flavor of the jet parton. Another disadvantage is the restriction to single scattering followed by single radiation in the medium, which makes this formalism more appropriate to thin media.

In finite temperature field theory formalism, often referred to as the AMY approach, the energy loss of hard jets is considered in an extended medium in equilibrium at asymptotically high temperature $T \to \infty$. Owing to asymptotic freedom the coupling constant $g \to 0$ at such high tempeatures, and a power counting scheme emerges from the ability to identify a hierarchy of parametrically separated scales $T \gg gT \gg g^2T$.... In this limit, it then becomes possible to construct an effective field theory of soft modes, $p \sim gT$, by summing contributions from hard loops with $p \sim T$, into effective propagators and vertices [227].

In the ASW/BDMPS approach, one incorporates the effect of multiple scattering of the incoming and outgoing partons in terms of a path integral over a path ordered Wilson line [228]. This formalism assumes a model for the medium as an assembly of Debye screened heavy scattering centers which are well separated in the sense that the mean free path of a jet $\lambda \gg 1/\mu$, the colour screening length of the medium [229]. The opacity of the medium $\tilde{n}$ quantifies the number of scattering centers seen by a jet as it passes through the medium, i.e. $\tilde{n} = L/\lambda$, where L is the thickness of the medium. The inclusion of the zero opacity term makes this the only formalism, to date, which includes interference between vacuum radiation and radiation induced by multiple soft scatterings in the medium. It suffers from the disadvantage of having approximated the medium in terms of heavy static scattering centers. As a result, elastic energy loss is vanishing in this scheme. As the formalism is setup to calculate the energy loss probability of the leading hard parton, estimation of the change in the distribution of final associated (sub-leading) hadrons or partons is not straightforward.

GLV scheme inorporates reaction operator approach to the opacity expansion [219]. It considers the limit of a thin quark-gluon plasma consisting of heavy static scattering centers with Yukawa-like potentials where the number of rescatterings of the jet and gluons is small.

All four schemes have independently made successful comparisons to the available data [230, 231]. The quantitative consistency of the different schemes has been investigated within a 3-dimensional hydrodynamics approach [231] linking the various medium properties via thermodynamical relations and using the same space–time evolution.

7.2 Implemented jet energy loss

Apart of technically difficult QCD-based schemes in our work we focus on simpler approach mainly because those schemes do not examine the evolution of plasma.

Energetic back-to-back partons produced in the early stages of a heavy-ion collision can travel through the medium and deposit energy and momentum along their path in a way that depends on the physics behind the interaction between the parton and the underlying medium. In the case where one of the partons is produced near the surface (trigger jet), the other supersonic away-side parton moves through the medium and excites a Mach wave as well as a diffusion wake. In general, a fast moving parton will lose a certain amount of its energy and momentum along its path through the medium and thus decelerate. It acts as a source to the medium. Therefore, depending on its energy

the parton will either punch through the medium and fragment in the vacuum or it will be severely quenched until it cannot be distinguished from the other thermal partons in the plasma. We assume that the energy lost by the parton thermalizes locally and gives rise to a source term J^ν in the energy–momentum conservation equations (4.1.5). It parametrises the deposition of energy and momentum into the medium. With the same term one can describe extraction of energy and momentum from the medium, but this case will not be elaborated here. The form of source term which describes the interaction of the jet with QGP is not known yet exactly, though some groups made progress on this topic [232, 233, 234, 235, 236, 237].

We first consider simple scenario with hard partons moving through the medium with an initial velocity $v_0 = 0.9999$, which corresponds to initial rapidity y_0=4.95. The source term in covariant notation is given by [59, 238, 239]

$$J^\nu(x) = \sum_i \int_{\tau_{i,i}}^{\tau_{f,i}} d\tau \frac{dP_i^\nu}{d\tau} \delta^4(x^\mu - x^\mu_{jet,i}), \tag{7.2.1}$$

where $\tau_{f,i} - \tau_{i,i}$ denotes the proper time interval associated with the evolution of the i-th hard parton, $\vec{x}_{jet,i}$ describes its position, and $dP_i^\nu/d\tau$ is its energy-momentum loss rate along its trajectory $x^\mu_{jet,i}(\tau) = x^\mu_{0,i} + u^\mu_{jet,i}\tau$. If $dP_i^\nu/d\tau$ would be the change of parton's energy it would have a negative sign, but we take $dP_i^\nu/d\tau$ as the change of QGP's energy so it has positive sign. Summation runs over all hard partons in the system. In numerical simulation we assume that the jet deposits its energy and momentum over some region characterized by a three-dimensional Gaussian profile. Then, in non-covariant notation, the source term that we use is [59]

$$J^\nu(x) = \sum_i \frac{1}{(\sqrt{2\pi}\sigma)^3} \exp\left(-\frac{[\vec{x} - \vec{x}_{jet,i}(t)]^2}{2\sigma^2}\right) \left(\frac{dE_i}{dt}, \frac{d\vec{P}_i}{dt}\right), \tag{7.2.2}$$

where it is chosen that $\sigma = 0.3$ fm. Partons are assumed to have the mass of 0.3 GeV when momentum loss is determined from the energy loss. Energy deposition and momentum deposition in the direction of the moving jet are denoted dE/dt and dP/dt, respectively. Parton energy loss depends on the density of the medium. The exact form of this dependence is not known, yet [236, 240]. Here we assume that it scales with entropy density s [241]. The scaling relation is thus

$$\frac{dE}{dx} = \left.\frac{dE}{dx}\right|_0 \frac{s}{s_0} \tag{7.2.3}$$

with s_0 corresponding to energy density 20.0 GeV/fm^3 ($T = 324$ MeV and $s = 78.2$ fm^{-3}). We have run our simulations with $dE/dx|_0$ set to 4 GeV/fm and 7 GeV/fm. They will be discussed in Chapter 9.

In case of static medium only, the energy loss was modelled according to simplified Bethe-Bloch prescription [59] with an explosive burst of energy and momentum (Bragg peak) at the end of parton trajectory. Due to its interaction with the plasma, the parton will decelerate and its energy and momentum loss will change. The hard partons deposit

energy and also momentum in the direction of their motion. The momentum loss is given as

$$\frac{dP}{dx} = \frac{1}{v_{parton}} \frac{dE}{dx} = a \frac{1}{v_{parton}^2}, \tag{7.2.4}$$

where $v_{parton} = \operatorname{artanh} y_{parton}$ is the parton velocity and a determines the absolute scale of the parton stopping. This equation shows that when the parton decelerates the energy-momentum deposition increases and has a peak for $v_{parton} \to 0$. In order to determine the actual velocity of the parton one can introduce parton rapidity

$$y_{parton} = \frac{1}{2} \ln \frac{1 + v_{parton}}{1 - v_{parton}}, \tag{7.2.5}$$

and then use the ansatz (7.2.4) and the identity $dP/dy_{parton} = m \cosh y_{parton}$, to derive the dependence of the time on parton rapidity [59]

$$t(y_{parton}) = \frac{m}{a} \left[\sinh y_{parton} - \sinh y_0 - \arccos \frac{1}{\cosh y_{parton}} + \arccos \frac{1}{\cosh y_0} \right], \tag{7.2.6}$$

where y_0 is the initial rapidity of the parton. The initial energy loss rate was set to $a = -4.148$ GeV/fm. This value is driven by the requirement that in our simulations parton stops exactly after $\Delta\tau = 5.0$ fm/c. The dependence of the time on the parton rapidity is plotted in the Fig. 7.1. The main difference between the ansatz described here

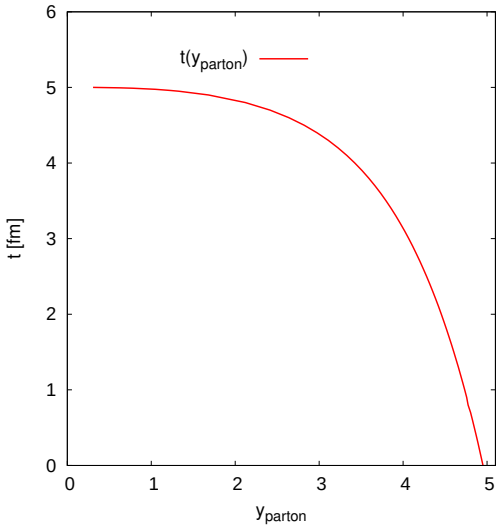

Figure 7.1: Graph of function $t(y_{parton})$ according to Eq.(7.2.6).

and the Bethe-Bloch equation is that the momentum deposition is longitudinal rather than transverse. Results of simulations which use this ansatz are presented in chapter 9.1.

Chapter 8

Anisotropic flow analysis methods

Now we describe the methods which are used experimentally to extract anisotropic flow coefficients from data. There are several often used flow analysis methods. Most of them are based either on the reaction plane reconstruction (the event plane method) [242] or on two-particle azimuthal correlations [243]. They rely on the assumption that the only correlations are those stemming from the existence of the reaction plane. Nonflow correlations, such as small-angle correlations due to final state interactions and quantum statistical effects [244], correlations due to resonance decays [245] and mini-jet production [246] are neglected.

In recent years, several alternative techniques were introduced, in which nonflow correlations can be disentangled. The cumulant method is based on a cumulant expansion of multiparticle (typically four-particle) correlations [247], which eliminates most nonflow correlations. It has been applied at ultrarelativistic energies at the LHC [248]. More recently, a new method based on an analogy with the Lee–Yang theory of phase transitions [249], where flow is extracted directly from the genuine correlation between a large number of particles, has been proposed [250, 251, 252]. This method is expected to provide the cleanest separation between flow and nonflow effects. Section 8.1 presents the event plane method. Section 8.2 is dedicated to particle cumulants method.

8.1 The event plane method

This is the most intuitive and the easiest method to implement. The problem is that the n-th harmonics reaction plane angle Ψ_r from Eq. (2.2.2) is not known experimentally. It is necessary to estimate it in some way. The event plane can be determined by [253]

$$\Psi_n = \frac{1}{n} \tan^{-1} \left(\frac{\sum_i w_i \sin(n\phi_i)}{\sum_i w_i \cos(n\phi_i)} \right), \tag{8.1.1}$$

where n is the Fourier order, the summation is over all particles in an event and w_i is a particle weight, like p_t or rapidity. Each type of anisotropy can be defined with its own symmetry plane, the so-called participant plane Ψ_n. Therefore the complete anisotropic flow analysis requires in the most general case the measurement of both v_n

and its symmetry plane Ψ_n. Then, the observed v_n can be easily calculated from Eq. (2.2.3). To take care of the fact that the event plane does not exactly match the reaction plane, a correction factor known as the event plane resolution is applied. The event plane resolution is $\langle\cos[n(\Psi_n - \Psi_r)]\rangle$, which again introduces the unknown reaction plane angle Ψ_r. Fortunately, this can be calculated for example by dividing the event into three sub-events a, b and c. In this case it is given by

$$\langle\cos[n(\Psi_n^a - \Psi_r)]\rangle = \sqrt{\frac{\langle\cos[n(\Psi_n^a - \Psi_n^b)]\rangle\langle\cos[n(\Psi_n^a - \Psi_n^c)]\rangle}{\langle\cos[n(\Psi_n^b - \Psi_n^c)]\rangle}}. \tag{8.1.2}$$

The n'th moment is then:

$$v_n = \frac{\langle\cos[n(\phi - \Psi_n)]\rangle}{\langle\cos[n(\Psi_n^a - \Psi_r)]\rangle}. \tag{8.1.3}$$

With that it is in principle possible to measure any flow moment [254]. Originally it was believed that the event plane did not have to be measured for the same Fourier moment as the flow moment of interest. But with the discovery of the significance of higher odd moments (v_3 and v_5), and their couplings to flow fluctuations it is now necessary to be more careful. In the case of even moments, there is still no problem as they are all usually correlated to the same event plane. But since the odd moments arise from fluctuations in the initial medium, the event planes found with these techniques do not align with those from even moments.

8.2 Particle cumulants

In our work we implemented the two-particle cumulant method. Specifically the approach developed by Ante Bilandzic [56] is used here. As input data we employed particles generated by THERMINATOR2 package [97].

This widely used method for measuring flow makes use of particle cumulants or multi-particle azimuthal correlations. The cumulants methods have two advantages; it is not required to know the event plane and it can be extended to multiparticle correlations. Multiparticle correlations have the advantage that non-flow does not affect them. Although cumulant methods do not need the event plane, they need a different kind of reference, which is called reference flow. The approach is to calculate flow over a large part of phase space, and then use that as a reference for the differential flow measurement of interest in the analysis. For anisotropic flow analysis it is customary to compute even number particle correlations. In practice only the two- and four-particle cumulants are computed, but in principle one could also compute six-particle cumulants or more. However, it is not believed that there is reason to do so, as the six-particle cumulant should give the same result as the four-particle cumulant, only requiring more statistics. Following subsections give details about the way of calculation in our implementation.

8.2.1 Reference flow

As mentioned before, the first step in calculation is to compute so-called reference flow. The flow is measured over a large part of phace space, however, it does not have to be the same in the entire region of phase space. The two- and four-particle azimuthal correlation functions are defined as:

$$\langle 2\rangle \equiv \langle \exp(in(\phi_1 - \phi_2))\rangle = \frac{1}{\binom{M}{2}2!} \sum_{\substack{i,j=1,\\(i\neq j)}}^{M} \exp(in(\phi_i - \phi_j)),$$

$$\langle 4\rangle \equiv \langle \exp(in(\phi_1 + \phi_2 - \phi_3 - \phi_4))\rangle = \frac{1}{\binom{M}{4}4!} \times$$

$$\sum_{i,j,k,l=1,(i\neq j\neq k\neq l)}^{M} \exp(in(\phi_i + \phi_j - \phi_k - \phi_l)), \tag{8.2.1}$$

where the summations are over all particles, ϕ_n is the azimuthal angle of n-th particle and M is the multiplicity within the chosen window. The four-particle cumulant method requires a huge amount of computing power. Generally, the four-particle equations are in general more complicated than two-particles ones, but their form is the same. In the following text, we omit the description of four-particle correlations because they were not used in our calculations. The introduction of Q_n-vectors saves computing time. The Q_n-vector is defined as:

$$Q_n \equiv \sum_{i=1}^{M} \exp(in\phi_i). \tag{8.2.2}$$

Two-particle reference flow

For practical computation of reference flow, it is advantageous to express Q_n-vector as

$$Q_n Q_n^* = |Q_n|^2 = \sum_{i,j=1}^{M} \exp(in(\phi_i - \phi_j)) = M + \sum_{\substack{i,j=1,\\(i\neq j)}}^{M} \exp(in(\phi_i - \phi_j)), \tag{8.2.3}$$

thus $\langle 2\rangle$ can be simply expressed as

$$\langle 2\rangle = \frac{|Q_n|^2 - M}{M(M-1)}. \tag{8.2.4}$$

The next step is to average $\langle 2\rangle$ over N events:

$$\langle\langle 2\rangle\rangle \equiv \langle\langle \exp(in(\phi_1 - \phi_2))\rangle\rangle = \frac{\sum_{i=1}^{N}(W_{\langle 2\rangle})_i \langle 2\rangle_i}{\sum_{i=1}^{N}(W_{\langle 2\rangle})_i}, \tag{8.2.5}$$

where $W_{\langle 2\rangle}$ is an event weight defined as

$$W_{\langle 2\rangle} \equiv M(M-1). \tag{8.2.6}$$

The second order cumulant is then

$$c_n\{2\} = \langle\langle 2\rangle\rangle, \tag{8.2.7}$$

in case of uniform azimuthal coverage. The n'th flow moment is then [56]

$$v_n\{2\} = \sqrt{c_n\{2\}}. \tag{8.2.8}$$

8.2.2 Differential flow

The differential flow is calculated for several bins of the observable of interest, in our case p_t. The differential flow calculations with Q_n-vectors are a bit more complicated than those of the reference flow. Particles used for the reference flow calculations are marked as Reference Particles (RFPs), there is a total of M of these. Particles used for the differential flow calculations are marked as Particles of Interest (POIs), in total there are m_p particles of interest in an event. It is possible to have an overlap between the RFPs and the POIs, i.e., a particle can be marked both as POI and RFP. Generally, there are m_q of these particles in an event. The two-particle correlations for differential flow are then:

$$\langle 2'\rangle \equiv \langle \exp(in(\Psi_1 - \phi_2))\rangle = \frac{1}{m_p M - m_q}\sum_{i=1}^{m_p}\sum_{j=1}^{M}\exp(in(\Psi_i - \phi_j)), \tag{8.2.9}$$

where Ψ_i denotes the azimuthal angle of the i'th POI. These calculations can be simplified by introducing the p_n-vector:

$$p_n \equiv \sum_{i=1}^{m_p}\exp(in\Psi_i), \tag{8.2.10}$$

Two-particle differential flow

Using p_n- and Q_n-vectors it can be shown that [56]

$$\langle 2'\rangle = \frac{p_n Q_n^*}{m_p M - m_q}. \tag{8.2.11}$$

Again this can be averaged over N events as for the reference flow

$$\langle\langle 2'\rangle\rangle = \frac{\sum_{i=1}^{N}(w_{\langle 2'\rangle})_i\langle 2'\rangle_i}{\sum_{i=1}^{N}(w_{\langle 2'\rangle})_i}, \tag{8.2.12}$$

where the event weight $w_{\langle 2'\rangle}$ is defined as:

$$w_{\langle 2'\rangle} \equiv m_p M - m_q. \tag{8.2.13}$$

The second order differential Q_n-vector for uniform azimuthal acceptance is then:

$$d_n\{2\} = \langle\langle 2'\rangle\rangle. \tag{8.2.14}$$

Finally, the quantity of interest, the differential flow v_n' for using two-particle cumulants can be expressed as [56]

$$v_n'\{2\} = \frac{d_n\{2\}}{\sqrt{c_n\{2\}}}. \tag{8.2.15}$$

Chapter 9

Results

Previous chapters summarized the state-of-the-art and mentioned necessary tools with which we were able to succesfully address the question of hard partons contribution to anisotropic flow.

The starting point for this work was the paper [182] which suggested possible contribution of hard partons to the anisotropic flow at the LHC. At the LHC hard partons are copious and deposit energy and momentum to the medium, where they can induce and influence collective flow. However, the cited paper lacked hydrodynamic simulation to confirm this scenario. It used only a toy model to find the contribution of hard partons at a level of a few percent. The influence of one hard parton moving through static medium was under investigation in 3+1-dimensional relativistic hydrodynamics in [59]. However, the interaction of streams induced by hard partons remained unknown there. So we started to investigate the interaction of two or more hard partons in static medium for the first time. Simulation of static medium was done first also due to the fact, that it is simpler than expanding medium simulation and the results for one hard parton could be qualitatively checked against [59]. Our results [255] confirmed the scenario that the assumption about merging of the streams in [182] was reasonable.

The next step of our investigation was to do similar simulations for expanding fireball with evolving hard partons. Our hydrodynamic model works with the assumption that momentum and energy are deposited locally in the vicinity of moving hard parton. These hard partons deposit energy and momentum during their whole existence. The exact way of implementation was described in Section 7.2. The initial conditions were inspired by those at the LHC, for details please see Chapter 6.2. Number, directions and total energy of each hard parton in each event were simulated using the approach presented in [182]. This approach is new. Although, there are related simulations in the literature, they either use boost-invariant hydrodynamics [256] or use only one hard parton with huge energy [257]. Using only one hard parton cannot lead to the alignment of the flow anisotropy with the geometry because the alignment is caused by merging of the induced streams. Finally, in [258, 259] the authors only study the influence of hard partons on radial flow and did not mention flow anisotropies. Simulation in 3+1-dimensions is a necessity for both static and expanding medium to capture all important effects. Hard partons moving in expanding medium break boost-invariance and thus 2+1-dimensional

simulation is inapplicable. Thanks to our full 3+1-dimensional hydrodynamic simulation with hard partons, we found that inhomogeneities induced by hard partons survive until the end of hydrodynamic simulation and contribute significantly to anisotropic flow for each simulated centrality class. This is the most important finding presented in this thesis.

This section is divided into two parts. At first we start with static medium results which are dealt with in section 9.1. After that, the Section 9.2 describes expanding medium results in 3+1-dimensional ideal hydrodynamics.

9.1 Static medium results

In this Section we focus on the interaction of streams induced by two hard partons penetrating through a static medium in different ways.

First case to investigate was the excitation of QGP by one hard parton moving along the x-axis. Results of this case can be directly compared to results of paper [59], although in [59] the situation was simulated for lower energy densities and energy deposition since the paper was focussed more at RHIC energy region. In [59] the authors used energy-momentum deposition with $dE/dx = 1.5$ GeV/fm and static QGP with temperature $T_0 = 200$ MeV. The difference is also in the implemented equation of state: we use the lattice QCD inspired parametrisation of [90] instead of the relativistic ideal gas equation of state of [59].

In our implementation of one parton scenario, hard parton moves from left to the right at initial speed $v = 0.9999$ and deposits energy and momentum into static medium with unperturbed energy density $\epsilon_0 = 20$ GeV/fm^3. The velocity of jet is decreasing during the evolution according to description in Section 7.2. At the end of evolution there is a Bragg peak in momentum and energy deposition. The value of unperturbed energy density $\epsilon_0 = 20$ GeV/fm^3 was used throughout all our implemented static medium cases. Profiles of the energy density are shown for various times in Fig. 9.1. The spot with highest energy density is observed at the position where parton deposits energy. The increase of the energy density spreads in a Mach-cone-like structure. There is a wake with a drop in the energy density profile just behind the parton. The energy spreads and streams flow even after the parton is fully stopped. Same simulation using the ultrarelativistic equation of state ($\epsilon = 3p$) leads to no significantly different results. The reason is that typical energy densities in the simulation are far above the transition from quarks to hadrons, where the sensitivity to different equation of state is strongest. Especially, the explosive burst of energy and momentum deposited by the parton immediately before it is fully quenched does not stop the strong flow behind the parton (the diffusion wake). This evolution of the parton is in qualitative agreement with results presented in [59] as one can compare in Fig. 9.2.

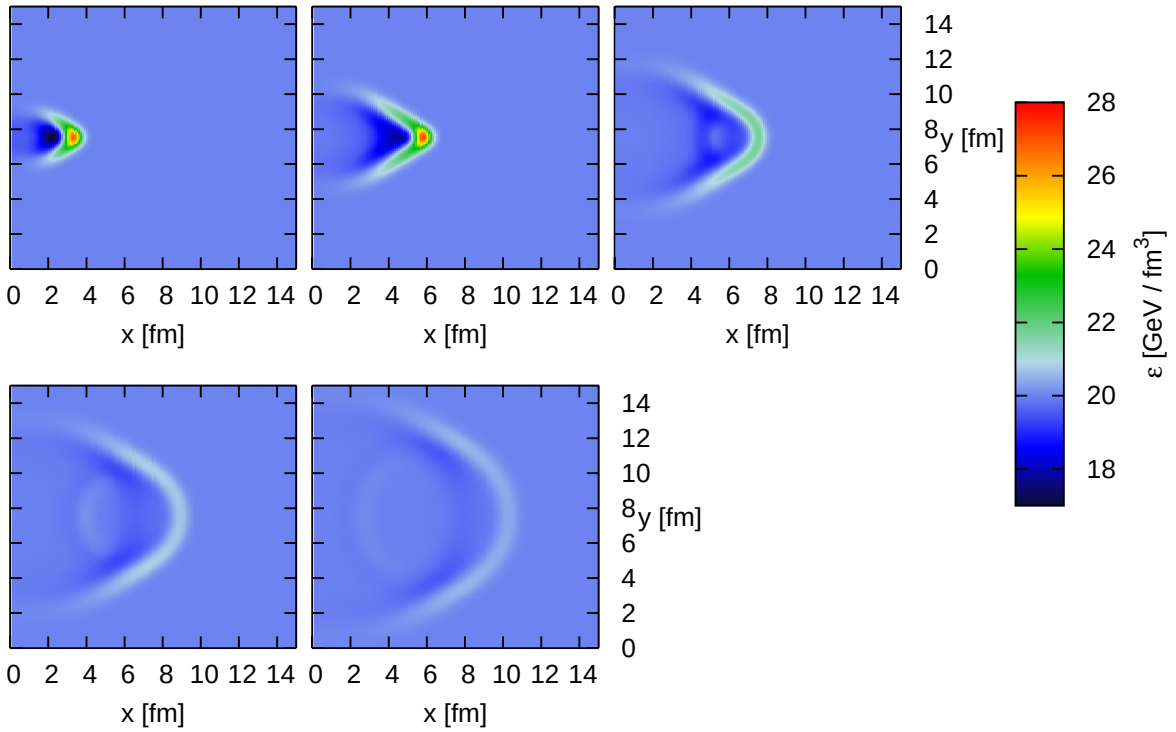

Figure 9.1: Sequence of energy density profiles during hydrodynamic evolution. One hard parton deposits energy and momentum into static medium. It enters from the left. First profile is taken after time delay $t = 2.5$ fm/c. Each of the following profiles is taken after a time period $\Delta t = 2.5$ fm/c after the previous profile. The energy of the parton is fully deposited after 5 fm/c. The initial energy loss is $dE/dx = -4.148$ GeV/fm, initial velocity of the parton is $v_{parton} = 0.9999$, and unperturbed static energy density is $\epsilon_0 = 20$ GeV/fm^3.

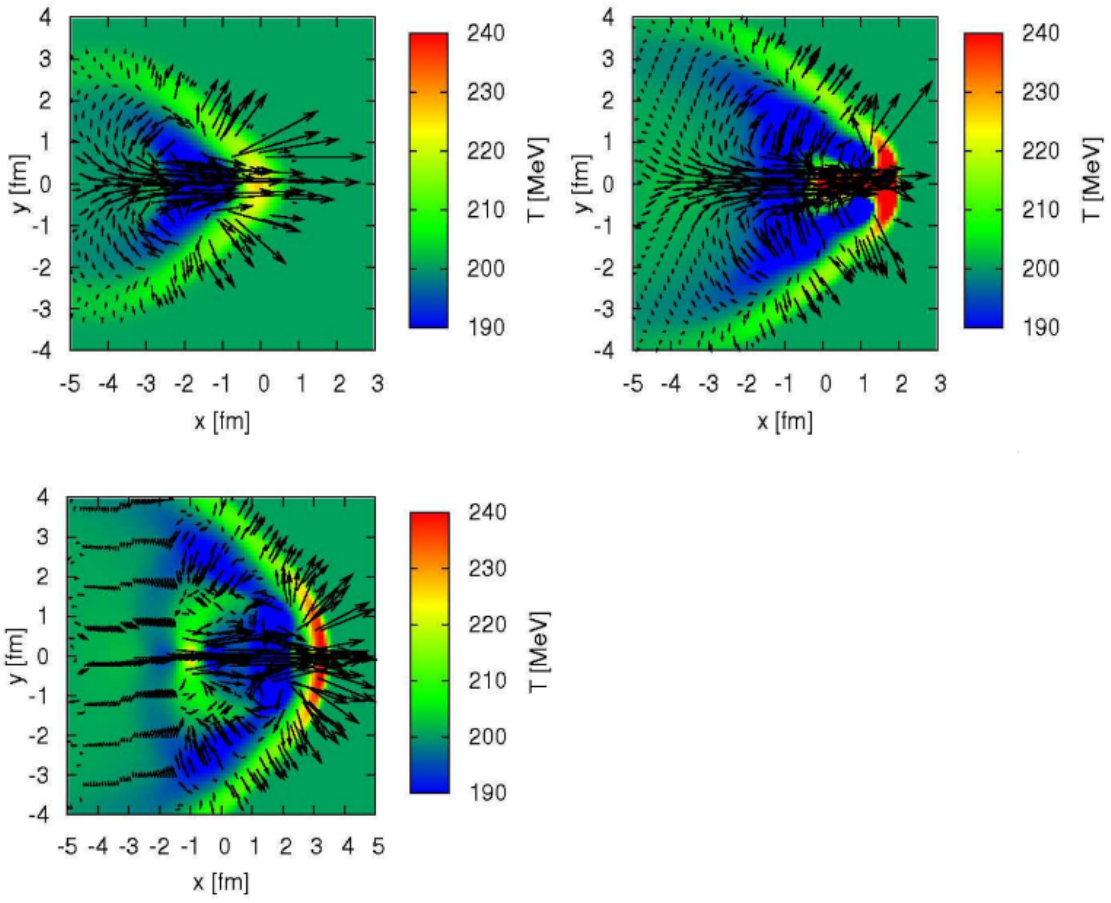

Figure 9.2: Temperature pattern and flow velocity profile (arrows) after a hydrodynamical evolution of $t = 4.5$ fm/c (left panel), $t = 6.5$ fm/c (middle panel) and $t = 8.5$ fm/c (right panel) for a parton which decelerates according to the Bethe–Bloch formula and stops after $\Delta x = 4.5$ fm. The parton' initial velocity is $v_{parton} = 0.999$, it corresponds to y_{parton}=3.8. The momentum loss is related to the energy loss by Eq. (7.2.4). Figure taken from [59].

We checked that the deposited momentum is almost fully contained in the diffusion wake. This was done by dividing the space into three regions: region I is the tube with diameter 1.5 fm around the parton trajectory up to the shock front of the Mach wave, region II is the rest of the matter behind the cone, and region III is the region ahead of the shock front in which no energy was deposited. At the moment of parton extinction region I contains 92% of all parton momentum. After next 2.5 fm/c this value drops just a little to 87%. The rest of the momentum is diffused into region II. This demonstrates our claim that deposited momentum shows up in form of the hot medium streams.

Momentum density in the surroundings of a moving parton shows the vortex structures similar to those in [59]. Close to the position of the depositing parton there is flow velocity in the direction of the parton and closely beside it flow velocity turns into the other direction. This is the vortex where matter flows backwards from the Mach cone in to the wake where the energy density is lower than in the unperturbed medium. Illustration of this vortex structure can be clearly seen the Fig. 9.3. In ideal hydrodynamics this vortex structure can be explained via vorticity conservation. If energy-momentum deposition of the parton into medium is sufficient then vorticity dominated diffusion wake is always present in the ideal fluid, whether the source of vorticity has been quenched or not [59]. The only way this vorticity can disappear is by means of viscous dissipation.

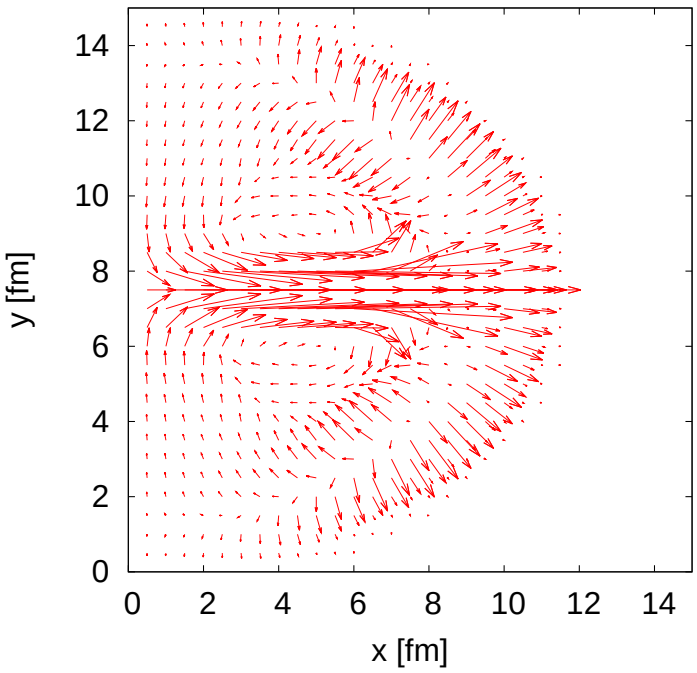

Figure 9.3: The vortex structure is created by one moving parton as shown. The direction and length of arrows correspond to the direction and magnitude of local momentum density, respectively.

Next, we investigate various scenarios including two hard partons moving in various directions. Figure 9.4 shows hydrodynamic evolution stimulated by two hard partons

moving in opposite directions against each other. Both loose the same amount of energy. All energy is deposited into plasma before the two partons would meet. Hence, only the diffusion wakes meet and the two streams of plasma hit each other. Both partons stop after time $t = 5$ fm/c. At this time their distance is 3 fm. The cone structures from both

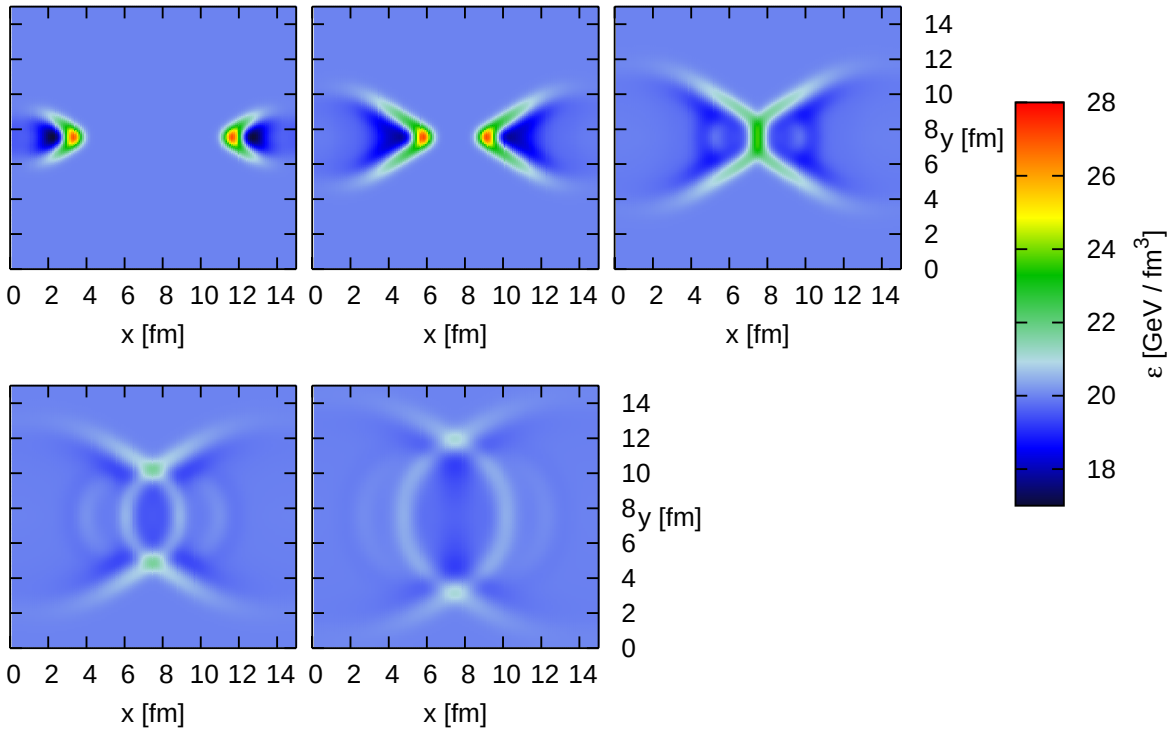

Figure 9.4: Sequence of energy density profiles during hydrodynamic evolution. Two hard partons deposit energy and momentum into static medium. They enter from the left and from the right and move against each other. The first profile is taken after time delay $t = 2.5$ fm/c. Following profiles are taken with subsequent delays of $\Delta t = 2.5$ fm/c. Partons are fully stopped after 5 fm/c. Initial energy loss is $dE/dx = -4.148$ GeV/fm, initial velocities are $v_{parton} = 0.9999$, and unperturbed static energy density is $\epsilon_0 = 20$ GeV/fm^3.

hard partons evolve like in previous case with just one hard parton. Momentum deposited from the partons is transferred into the diffusion wake where the matter streams in the direction of the original parton. The two streams meet and stop.

Deposited momentum for various scenarios with partons aiming in opposite directions is shown in Fig. 9.5. This figure confirms that the momentum density does not overrun to the other side even if one parton deposits more momentum than the other (blue dashed line).

In real situation, parton-induced streams will come together under various angles. In order to see how they may interact we examine a situation where the two partons move perpendicularly. In Fig. 9.6 two hard partons, one entering from the left and the other from the bottom in the same plane, deposit energy and momentum into static medium.

Partons are fully stopped 1.5 fm/c before they would meet. We can see that the conical structures of higher energy density look like a superposition of the two Mach cones that propagate also after the full quenching of the partons. The merging of diffusion wakes is also demonstrated in Fig. 9.7. Both panels display momentum density in the direction diagonal to the two partons against the diagonal coordinate for various perpendicular partons scenarios.

Although the parton source terms vanish before the wakes make contact, the merged wakes continue to evolve. Momentum density also exhibits double peak structure.

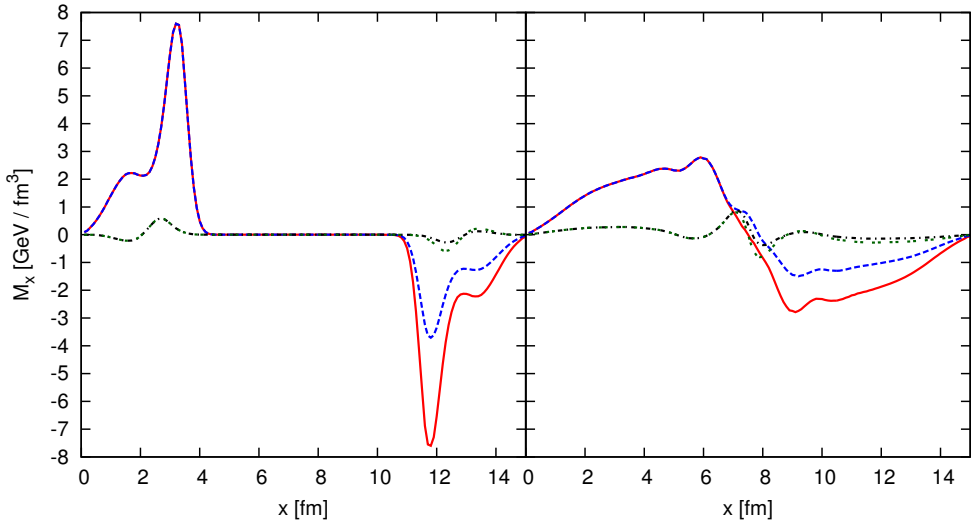

Figure 9.5: Situation from Fig. 9.4. Momentum density along the trajectory of the partons in opposite directions. Left panel: momentum density at the moment of extinction. Right panel: momentum density after another 2.5 fm/c. Red solid line: pair of partons with equal energy. Blue dashed line: pair of partons where parton on the right has originally a half of the other parton's energy. Green double dashed line: pair of partons in opposite directions, parton on the right is moving along the x-axis in the axial distance of 2 fm from the other parton's trajectory; momentum density distribution is taken along the line in center between the two partons. Black dash and dotted line: same as previous case but parton entering from right has originally a half of the other parton's energy.

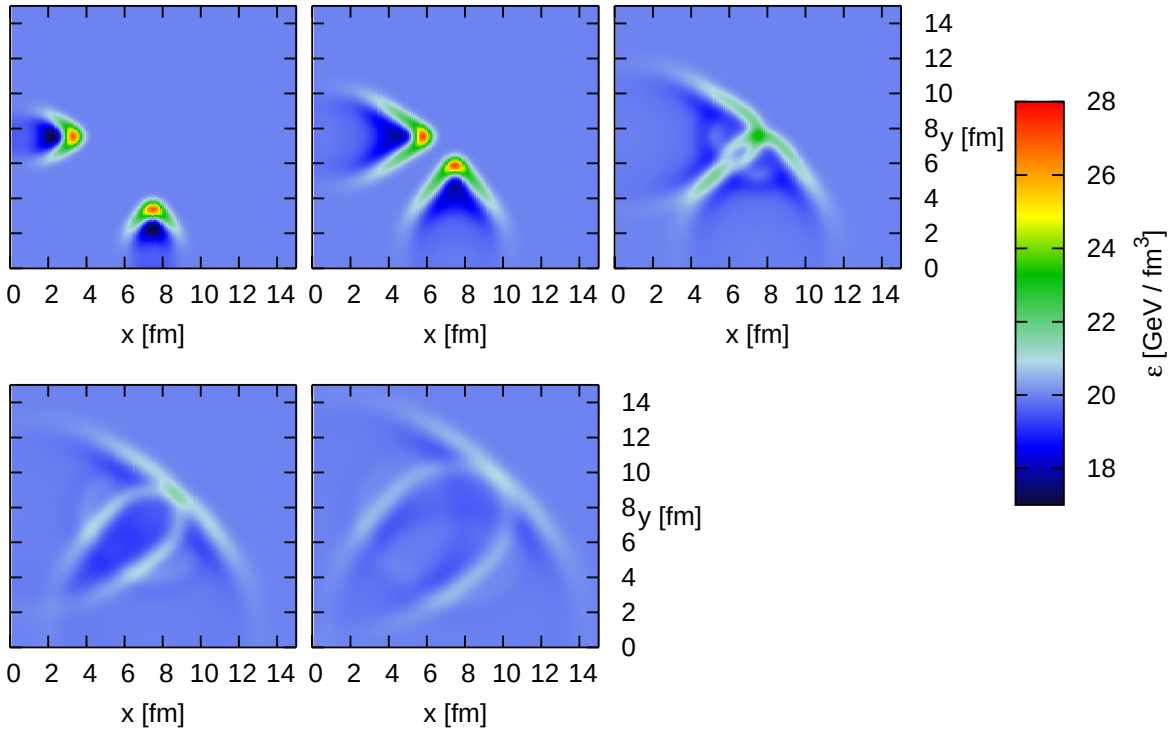

Figure 9.6: Sequence of energy density profiles during hydrodynamic evolution. Two hard partons deposit energy and momentum into static medium. One enters from the left, one enters from the bottom. First profile is taken after a delay of $t = 2.5$ fm/c, the subsequent after time steps $\Delta t = 2.5$ fm/c. Partons are fully quenched after 5 fm/c. The initial energy loss is $dE/dx = -4.148$ GeV/fm, initial velocity is $v_{parton} = 0.9999$, unperturbed static energy density is $\epsilon_0 = 20$ GeV/fm^3.

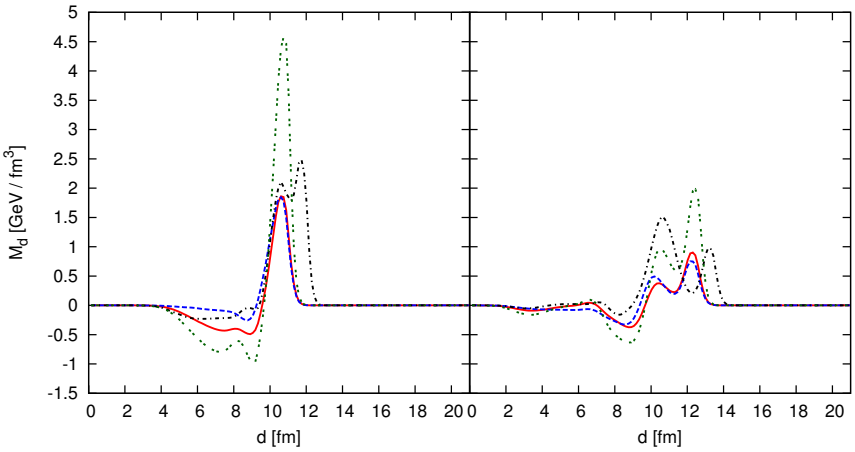

Figure 9.7: Situation from Fig. 9.6. Momentum density in diagonal direction during hydrodynamic evolution as a function of the diagonal coordinate. Partons move perpendicularly to each other and source terms vanish at $t = 5$ fm/c, which is 1.5 fm/c before they would meet, unless stated othewise. Left panel: profile at $t = 7.5$ fm/c, right panel: $t = 10.0$ fm/c. Red solid line: perpendicular partons scenario, both partons have equal energy. Blue dashed line: same scenario as before but the lower side parton has a half of the other parton's energy. Green double dashed line: each parton deposits two times more energy than in the first case. Black dash and dotted line: partons source terms vanish only 0.5 fm/c before partons would meet.

Behind the merged wakes the momentum density turns negative, it points backwards. This is a part of the vortices that are built up on the sides around the parton. We observed that the lower unperturbed energy density or higher energy-momentum deposition induce higher momentum density on the diagonal when wakes merge, as expected. The peaks in momentum density corresponding to merging of two wakes with equal and also with unequal energy seem qualitatively similar.

However, it is very rare that two partons would be aimed so precisely that their wakes meet exactly as it was assumed so far. Therefore, we examined a situation with velocities perpendicular to each other but the distance of closest approach of their extrapolated trajectories is 2 fm. The evolution of the energy density on the plane in the middle between the two trajectories is shown in Fig. 9.8. We investigate also the plots of velocity and momentum densities. The evolution of mometum density profile is plotted in Fig. 9.9. The wake streams and their merging is less visible in such a distance from the original partons. On the other hand, one better sees the vortices that are built at the two sides behind the parton which survive after the partons are quenched. Diagonal dependences of the momentum density look in this case qualitatively similarly as in Fig. 9.7, only the size of momentum densities is typically lower.

In conclusion, when two streams meet and even are not being stimulated anymore

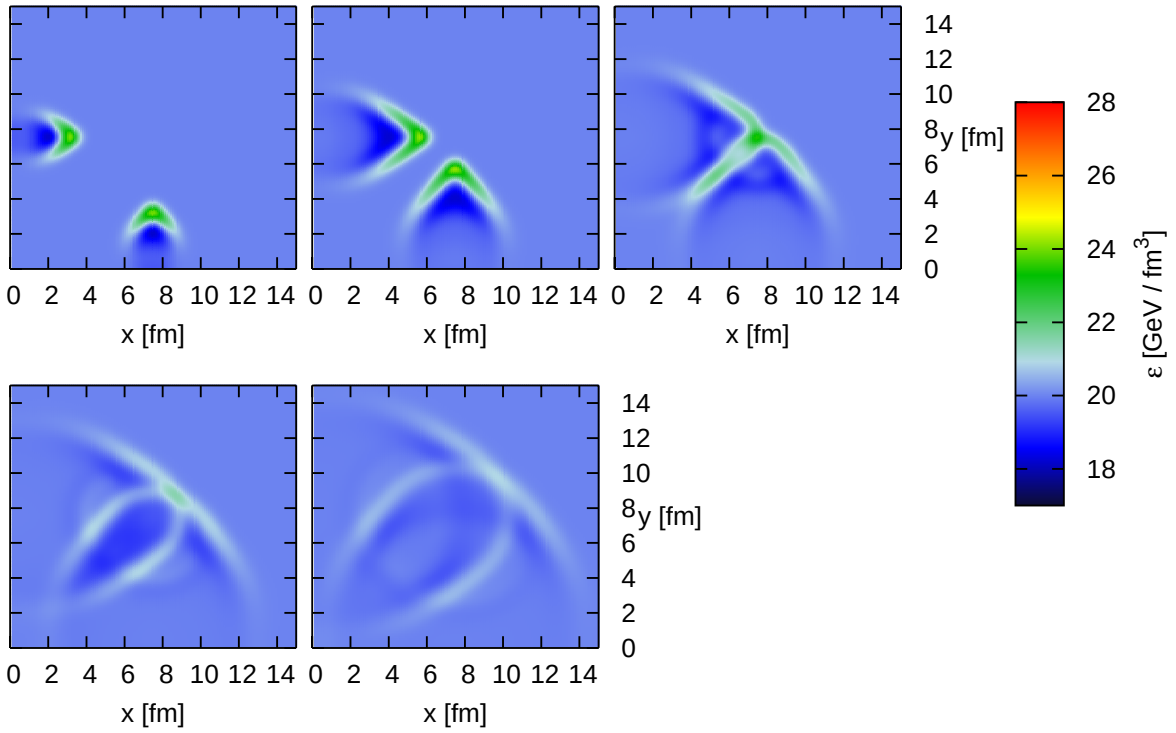

Figure 9.8: Sequence of energy density profiles during a hydrodynamic evolution. Two hard partons deposit energy and momentum into static medium. One enters from the left, one enters from the bottom. Distance of closest approach of extrapolated trajectories is 2 fm. Profiles are taken on the plane in the middle of both trajectories. First profile is taken after $t = 2.5$ fm/c. All other profiles are taken with subsequent delays $\Delta t = 2.5$ fm/c. Partons are quenched after 5 fm/c, i.e. in the second figure. The initial energy loss is $dE/dx = -4.148$ GeV/fm, initial velocity is $v_{parton} = 0.9999$, unperturbed static energy density is $\epsilon_0 = 20$ GeV/fm^3.

by a hard parton, they merge into one stream which continues until it is suppressed by diffusion. This model simulation verifies that the streams which are generated in the wakes indeed carry the deposited momentum. It also confirms the scenario suggested in [182]. That paper concluded that in heavy ion collisions, isotropically produced hard partons generate interacting wakes which can lead to collective motion that exhibits elliptic flow correlated with the direction of the reaction plane. However, it remains to be studied, how big the effect is in realistic simulations reproducing the dynamics of the fireball. This issue is the subject of next section.

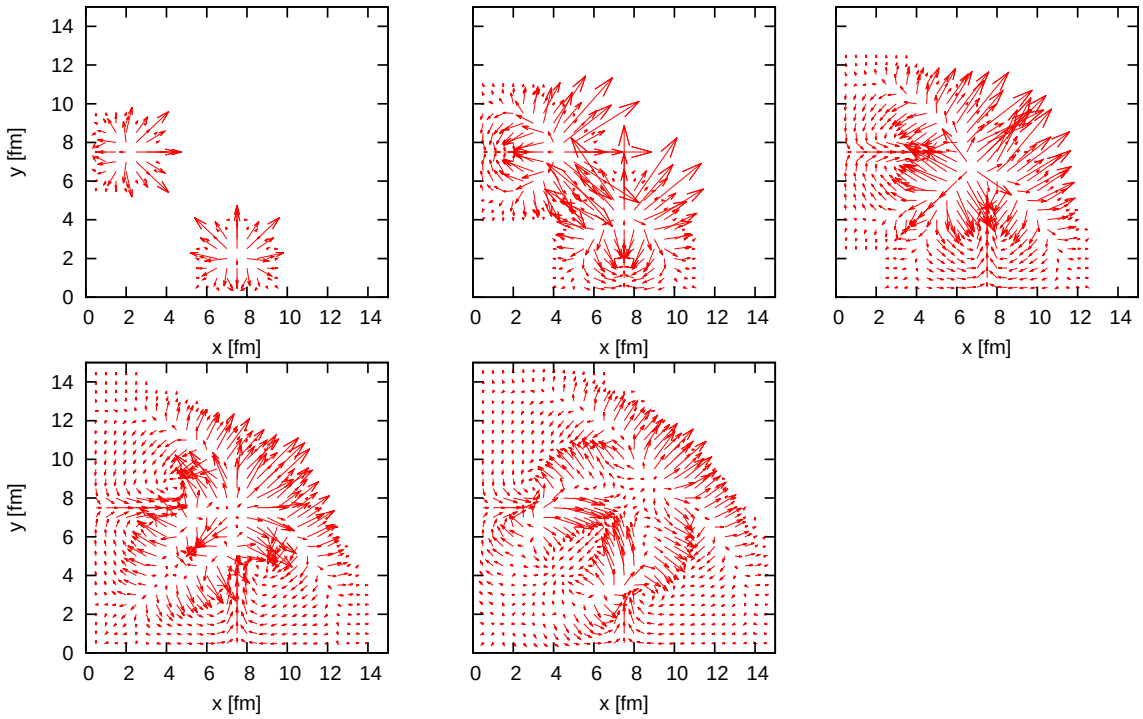

Figure 9.9: Situation from Fig. 9.8, but the direction and length of arrows correspond to the direction and magnitude of local momentum density, respectively.

9.2 Expanding medium results

For simulations with expanding medium we perform hydrodynamic simulations with LHC inspired conditions, for details on initial conditions see section 6.2. We aim to simulate Pb+Pb collisions at full LHC energy $\sqrt{s_{NN}} = 5.5$ TeV. Different sets of events in three centrality classes were simulated to recognize the effect of anisotropic flow caused by hard partons. The centrality classes employed in simulations were: ultracentral set of events (impact parameter $b = 0$), set of central events (centrality class 0-2.5%, impact parameter $b = 0 - 1$ fm) and set of peripheral events (centrality class 30-40%, impact parameter $b = 6 - 7$ fm). Each set contained 100 different hydrodynamic events. On top of that we run on each obtained freeze-out hypersurface five times the THERMINATOR2 freeze-out procedure and thus the number of events in the analysis was quintupled. Resonance decays were included. The anisotropic flow parameters v_1, v_2, v_3 and v_4 were obtained for charged hadrons by the two-particle cumulant method. As RFPs, pions in rapidity (-0.9,0.9) and in whole p_t range were used in the analysis. POIs for differential flow are all charged hadrons. The extracted anisotropic flow coefficents were then compared among different types of scenarios.

First scenario as a benchmark test we simulate events with no hard partons and no fluctuations, e.g. with only smooth initial conditions. It is easy to distinguish contribution from hard partons by comparison with this scenario. Second scenario is a simulation with hot spots where there is energy anisotropy included in the initial conditions and not released over the finite time interval, no momentum is deposited. These are regions where the same amount of energy is deposited that a hard parton would carry if it was produced there. Also their number corresponds to number in simulation with hard partons and their size corresponds to size of hard partons at the beginning of the hydrodynamic evolution. Third one is the hot-spots-with-momentum scenario refers to the case where energy as well as momentum are superimposed onto the initial conditions. Basically, it is the same scenario as hotspots but the momentum of same amount as energy is deposited in initial conditions. The last scenario is our proposal, e.g. momentum and energy is deposited *during* the hydrodynamic evolution. It is in contrast to the common hydrodynamic scenarios which take into account only fluctuations in initial energy or energy and momentum density profiles where all features unique for a given event are specified in their initial conditions from which hydrodynamics based on energy-momentum conservation is started.

We start with the investigation of the generated anisotropy of momentum distribution in ultra-central collisions ($b = 0$) for various scenarios. Results are shown in Figure 9.10 and Fig. 9.11. Comparison in Fig. 9.10 shows the importance of momentum deposition *during* the hydrodynamic evolution. It is shown that the hot-spots simulation does not produce the same amount of momentum anisotropy as generated by wakes with streams induced by hard partons. Results for simulations without any fluctuations are consistent with 0 as expected. In Fig. 9.11 it is somewhat puzzling why there is no difference in results between the two scenarios which differ in the value of the energy loss. Note that the total amount of the energy deposited into plasma is the same in both cases. They differ by how fast this process runs. Hence, it was interesting to investigate the limit case where $dE/dx|_0 \to \infty$. It corresponds to the case where momentum and energy is deposited

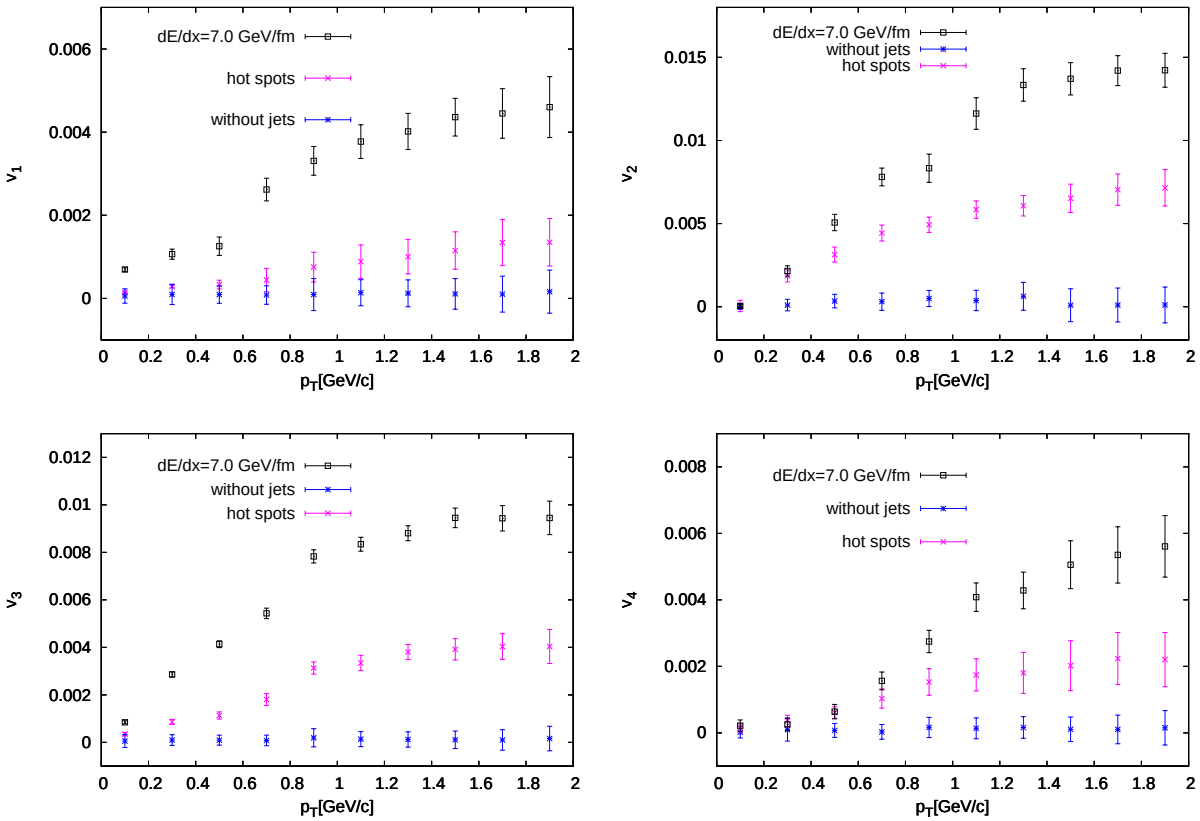

Figure 9.10: Parameters v_n from collisions at $b = 0$ for charged hadrons. Different symbols represent: energy loss of hard parton $dE/dx|_0 = 7$ GeV/fm (black $\square$), scenario with only hot spots in initial conditions (purple $\times$), and scenario with smooth initial conditions (blue *).

in initial conditions. Exploration of this limiting case is important. If it leads to the same results as the simulations with finite dE/dx, then all inhomogeneities in energy and momentum density can be put into initial conditions. It can be seen that it is not the case. Neither fluctuations with momentum deposition in the initial conditions by themselves are able to generate the same flow anisotropies. The opposite limit $dE/dx|_0 \to 0$ represented by simulations with $dE/dx|_0 = 0.1$ GeV/fm leads to results consistent with 0 for all anisotropic flow coefficients as expected.

The CMS collaboration has found a strong dependence of p_T averaged v_2 and v_3 on centrality even for central collisions [260] as shown in Fig. 9.12. The observation consists in fact that anisotropic flow coefficients v_2 and v_3 steeply rise as we go from central collisions to peripheral. Currently no hydrodynamic model can correctly simultaneously describe centrality dependence of both elliptic and triangular flow for ultracentral CMS events. The non-zero harmonics for ultracentral collisions are predominantly induced by fluctuations. All orders of v_n saturate around 0.0-0.2 % centrality. Although here we only want to get an educated estimate on the size of the effect that our mechanism can generate, it is tempting now to look how our v_n's would change if we go to centrality class 0-2.5%. In Fig. 9.13 we present the integrated v_n's as functions of centrality. We see that

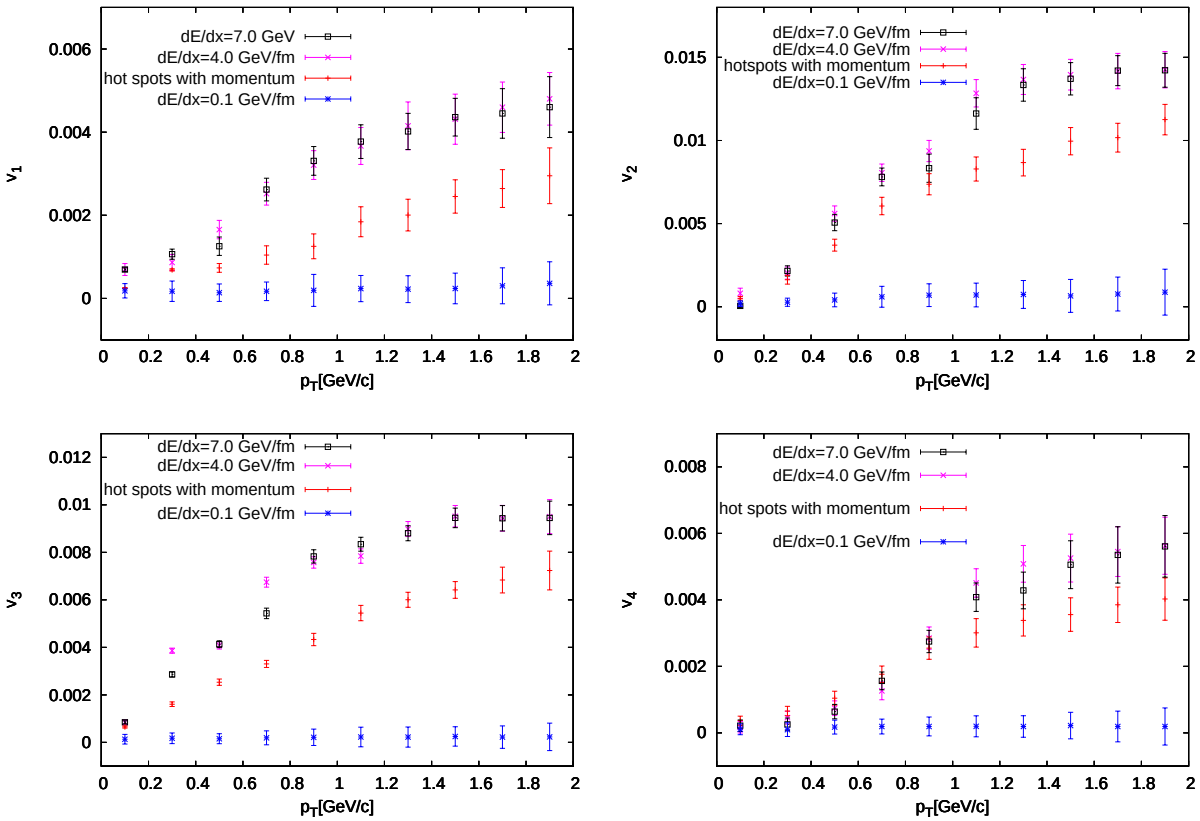

Figure 9.11: Parameters v_n from collisions at $b = 0$ for charged hadrons. Different symbols represent: energy loss of hard parton $dE/dx|_0 = 7$ GeV/fm (black □), scenario with hot spots with momentum deposition in initial conditions (red –), scenario with energy loss of hard parton $dE/dx|_0 = 4$ GeV/fm (purple ×), and scenario with energy loss of hard parton $dE/dx|_0 = 0.1$ GeV/fm (blue *).

going from $b = 0$ fm to 0-2.5% centrality there is no dramatic increase in v_n's. If such effect is present in data, it must be caused by a different mechanism.

Next, we move further in centrality and simulate sets of events within centrality class 30–40% ($b = 6$–7 fm). Again here, we investigate whether the effect of energy-momentum deposition from hard partons can be represented by appropriate choice of the initial conditions. We show results of simulations with energy *and momentum* superposition onto the smooth profile of the initial conditions in Figs. 9.14 and 9.15. Also here, the amount and distribution of energy and momentum is the same as would be carried by hard partons if they were integrated into the simulation. We observe that even the inclusion of hot spots with momentum into the initial state cannot account for the whole effect on anisotropy which is generated by momentum deposition from hard partons during the evolution of the hydrodynamic bulk. The results of v_2 demonstrate that the flow anisotropy generated by hard partons is correlated with the reaction plane. If it was not true, the contribution to anisotropic flow would cancel and we would not see any increase. This is a consequence of the mechanism where two streams of the fluid in the wakes merge when they are close. Then they continue flowing in the direction given by momenta of the

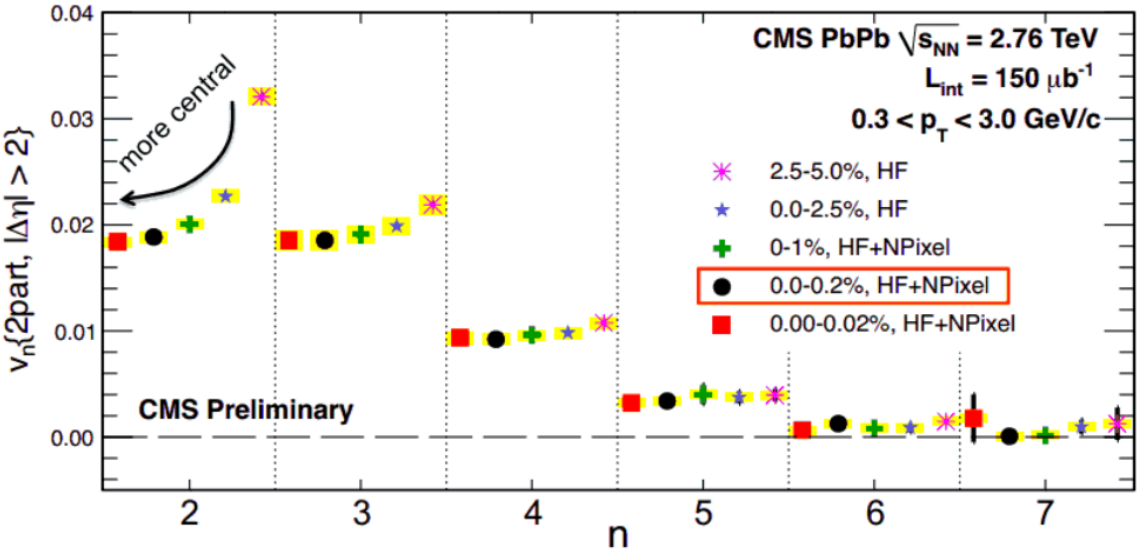

Figure 9.12: CMS anisotropic flow results for (ultra)-central collisions [260].

two streams [182], [255]. With hard partons added, v_2 grows by about 50% with respect to simulation with smooth initial conditions and no hard partons. Of course, v_3 vanishes in the absence of hard partons or hot spots due to the lack of third order anisotropy within the bulk matter.

Our results show that the momentum deposition during fireball evolution must be included in a realistic hydrodynamic simulation. As a consequence, the linear relation between initial state anisotropies ϵ_n and v_n's may not be fully justified because in our suggested mechanism the anisotropy can rise during the fireball evolution. This is most clearly apparent in our results for ultra-central collisions (Fig. 9.10). Initial state anisotropies of all orders vanish in those simulations. A related question is then posed: can one find a relevant measure of spatial fireball anisotropy which is then translated into final-state momentum anisotropy? Perhaps the evolution of anisotropy decomposition into orthogonal terms [46, 47] may provide some insights here. Figures 9.14 and 9.15 confirm the results obtained from ultra-central sets of events, that the interplay of many hard-partons-induced streams causes significant contribution to the azimuthal anisotropies. This cannot be replaced by initial-state-generated flow anisotropies.

It remains to explore the influence of viscosity on anisotropic parameters for all presented scenarios. We try to estimate this effect somehow. In case of viscosity, in viscous fluid, the deposited momentum is spread to larger volume than in case of ideal fluid. This is confirmed by simulation of Mach cones in viscous 3+1-dimensional hydrodynamics in [261]. Thus surprisingly, the viscosity can even strenghten the momentum anisotropy observed.

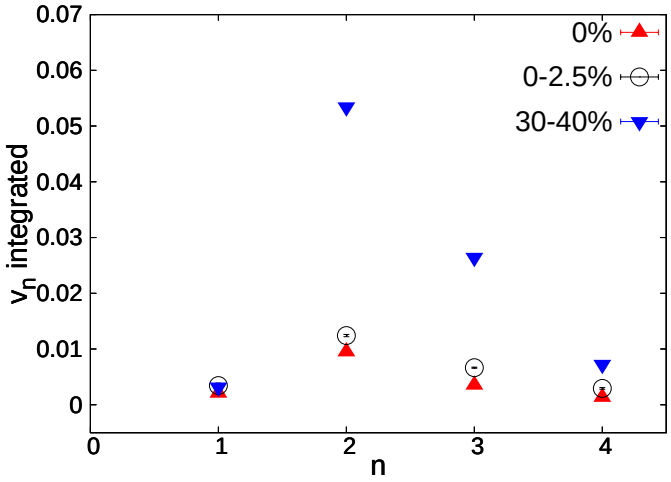

Figure 9.13: Anisotropy parameters v_n for charged hadrons integrated over p_t for different centralities. The energy loss of hard partons is given by $dE/dx|_0 = 4$ GeV/fm.

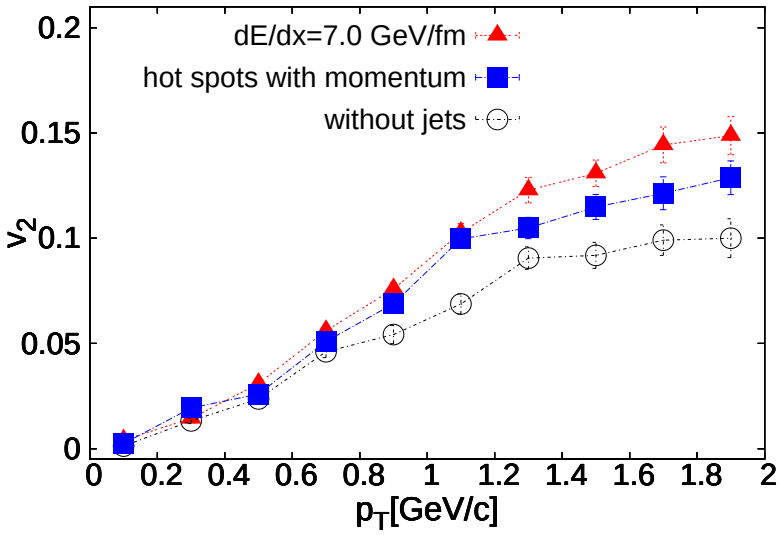

Figure 9.14: Anisotropy parameters v_2 for charged hadrons as functions of p_t from collisions within centrality class 30-40%. The energy loss of hard partons is given by $dE/dx|_0 = 7$ GeV/fm, other scenarios as in Fig. 9.10.

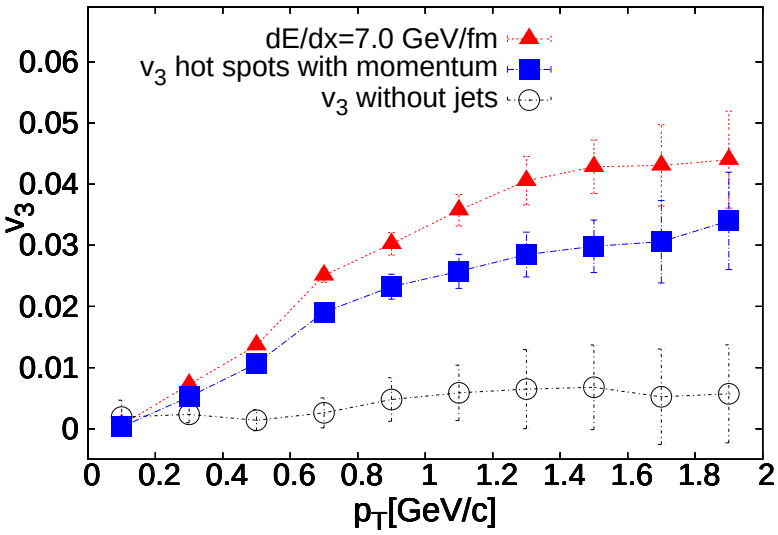

Figure 9.15: Anisotropy parameters v_3 for charged hadrons as functions of p_t from collisions within centrality class 30-40%. The energy loss of hard partons is given by $dE/dx|_0 = 7$ GeV/fm, other curves as in Fig. 9.10.

Chapter 10

Conclusions

Energy and momentum deposition from hard partons into hot deconfined matter and the response of the matter have been investigated by means of three-dimensional ideal relativistic hydrodynamics in both static and expanding medium.

The most important fact which was found in this thesis is the finding that jets produce anisotropy. It confirms the assumption made in [182]; i.e. the wakes generated by hard partons interact and influence each other. Furthermore, when two streams meet and are not being stimulated anymore by a hard parton, they merge into one stream which continues until it is tamed by diffusion. Under such conditions in a heavy-ion collision isotropically produced hard partons generate interacting wakes which lead to collective motion that exhibits anisotropic flow correlated with the direction of the reaction plane.

Hydrodynamic simulations for expanding medium were set to resemble the collisions at the LHC. As the initial condition, optical Glauber model was used because it produces smooth IC. With optical Glauber model anisotropic flow cannot be explained since there is no anisotropy in the initial state in central collisions. However, this fact is an advantage in case of distinguishing the influence of hard partons onto anisotropic flow. All state-of-the-art hydrodynamic models take into account that the initial energy and momentum density profile for hydrodynamic simulation changes event-by-event. Thus all features unique for a given event are specified in the initial conditions from which hydrodynamic simulation is started. It is in contrast to our model, where energy and momentum is deposited into the medium *during* its evolution and not only at the beginning. Our results show that including only fluctuating initial conditions even with momentum density fluctuations is not sufficient to have substantial influence on momentum anisotropy. For non-central collisions the effect is correlated with event geometry therefore we indeed obtain positive contribution to the elliptic flow as shown before. The influence of hard partons on flow anisotropies will show itself in various orders of particle production anisotropies. Furthermore, the linear relation between initial state anisotropies ϵ_n and v_n's as advocated in literature may not be fully justified because in our suggested mechanism the anisotropy can rise during the fireball evolution and the relation is violated. The presented results clearly demonstrate the necessity to include this mechanism into realistic hydrodynamic simulations which aim at extracting the properties of quark matter.

In conclusion, we see that we have identified a mechanism which generates anisotropic

flow and consequently anisotropic particle production in ultrarelativistic nuclear collisions. More precise studies would require the inclusion of three-dimensional viscous hydrodynamic model and other sources of fluctuations. Nevertheless, clear distinction of fluctuation sources can be very hard. Furthermore, inclusion of viscosity may even enhance the influence of this effect. Quantitative details of the added mechanisms remain to be investigated.

List of publications

1. M. Schulc, B. Tomášik, The effect of momentum deposition during fireball evolution on flow anisotropy, arXiv:1512.06215, (2015)

2. B. Tomášik, M. Schulc, I. Melo, R. Kopečná, Observables of non-equilibrium phase transition, accepted in EPJ, contribution to NICA white paper, arXiv:1511.00034 (2015).

3. M. Schulc, M. Košťál, D. Harutyunyan, M. Švadlenková, V. Rypar, J. Milčák, A. Kolros, The effect of iron cross-section in thermal region on neutron transport in VVER-1000 mock-up in LR-0 reactor, will be published in Journal of Nuclear Engineering and Radiation Science.

4. M. Košťál, V. Rypar, F. Cvachovec, B. Jánský, D. Harutyunyan, M. Schulc, V. Juříček, J. Milčák, E. Novák and S. Zaritskyi, Neutron deep penetration through reactor baffle, barrel, pressure vessel and biological concrete shield of VVER-1000 Mock-Up in LR-0 reactor, will be published in Annals of Nuclear Energy.

5. M. Košťál, M. Schulc, V. Rypar, E. Novák and S. Zaritskyi, VVER-1000 Mock-up Physics Experiments Hexagonal Lattices (1.275 cm Pitch) of Low Enriched U(2.0, 3.0, 3.3 wt.% 235U)O2 Fuel Assemblies in Light Water with H3BO3, LR(0)-VVER-RESR-002, benchmark OECD, NEA (2015).

6. E. Novák, V. Rypar, M. Schulc, Vliv míry obohacení kyseliny borité izotopem B10 na kalibraci boroměru PN160/VKB, Research report, Research centre Řež, (2015).

7. M. Koleška, J. Milčák, J. Šoltes, M. Vinš, E. Losa, M. Košťál, M. Schulc, M. Šunka, S. Flíbor, Validace výpočetního kódu MCNP6/MCNP5/MCNPX, Research report, Research centre Řež, (2015).

8. E. Losa, M. Košťál, V. Rypar, M. Schulc, B. Jánský and E. Novák, Utilization of LR-0 Reactor in MSR Research, In Joint International Conference on Mathematics and Computation (MC), Supercomputing in Nuclear Applications (SNA) and the Monte Carlo (MC) Method Apr 19-23, 2015, proceedings.

9. M. Schulc and B. Tomášik, Flow anisotropies due to momentum deposition from hard partons, Acta Phys.Polon.Supp. 8, 433 (2015).

10. M. Schulc and B. Tomášik, Anisotropic flow generated by hard partons in medium, arXiv:1501.00788, Proceedings of International Workshop on Collectivity in Relativistic Heavy Ion Collisions, Kolymbari, Crete, 14-20.9.2014, (2015).

11. M. Schulc and B. Tomášik, Anisotropic flow from hard partons in ultra-relativistic nuclear collisions, arXiv:1410.8711, Proceedings of PANIC 2014 conference, Hamburg, Aug.2014, (2014).

12. M. Schulc and B. Tomášik, Anisotropic flow of the fireball fed by hard partons, Phys. Rev. C90 064910 (2014).

13. M. Schulc and B. Tomášik, Stimulation of static deconfined medium by multiple hard partons, J. Phys. G40 125104, (2013).

14. M. Schulc and B. Tomášik, Rapidity correlations of protons from a fragmented fireball, Eur. Phys. J. A45 91-97, (2010).

Presentations at international conferences

1. Neutron flux measurements and calculation behind VVER-1000 reactor pressure vessel simulator placed in LR-0 reactor, Joint International Conference on Mathematics and Computation, Supercomputing in Nuclear Applications and the Monte Carlo Method, Nashville TN, USA, poster, (2015).

2. Hydrodynamic evolution with energy and momentum feeding during the fireball expansion, Quark Matter 2014, Darmstadt, Germany, poster, (2014).

3. Stimulation of deconfined medium by multiple hard partons, 13th Zimanyi winter school on heavy ion physics, Budapest, Hungary, talk, (2013).

4. Response of QGP to two hard partons, Schladming Winter School 2013 - Extreme QCD in and out of equilibrium, Schladming, Austria, poster, (2013).

5. Response of Quark Gluon Plasma to two hard partons, Quark Matter 2012, Washington DC, USA, poster (2012).

6. The contribution of hard processes to elliptic flow, 8th Summer school on nuclear physics, Blagoevgrad, Bulgaria, talk, (2012).

7. Fireball fragmentation and rapidity correlations of protons, Quark Matter 2011, Annecy, France, poster (2011).

8. Fireball fragmentation and rapidity correlations of protons, 17th Conference of Czech and Slovak physics, Zilina, Slovakia, talk, proceedings, (2011).

9. Rapidity correlations of protons from fragmented fireball, 10th Zimanyi winter school on heavy ion physics, Budapest, Hungary, talk (2010).

10. Rapidity correlations of protons from fragmented fireball, TORIC workshop, Villasimius, Italy, talk, (2010).

Bibliography

[1] STAR collaboration, Nuclear Physics A Volume 757, Issues 1-2 , 8 August 2005, Pages 1-27 (BRAHMS), Pages 28-101 (PHOBOS), Pages 102-183 (STAR) and Pages 184-283 (PHENIX).

[2] B.R. Martin and G. Shaw, Particle Physics, Wiley, 2nd edition, 2005.

[3] J. C. Collins and M. J. Perry, Phys. Rev. Lett. 34, 1353 (1975).

[4] B. A. Freedman and L. D. McLerran, Phys. Rev. D 16, 1169 (1977).

[5] E. V. Shuryak, Theory Of Hadronic Plasma, Sov. Phys. JETP 47, 212 (1978).

[6] Y. Aoki, G. Endrodi, Z. Fodor, S. D. Katz, and K. K. Szabo, Nature 443, 675 (2006).

[7] Z. Fodor, S. D. Katz, and K. K. Szabo, Phys. Lett. B568, 73 (2003).

[8] Z. Fodor and S. D. Katz, JHEP 04, 050 (2004).

[9] R. V. Gavai and S. Gupta, Phys. Rev. D71, 114014 (2005).

[10] P. de Forcrand, S. Kim, and O. Philipsen, PoS LAT2007, 178 (2007).

[11] G. S. F. Stephans, J. Phys. G32, S447 (2006).

[12] R. A. Lacey *et al.*, Phys. Rev. Lett. 98, 092301 (2007).

[13] A. Laszlo *et al.*, [NA61 Collaboration], arXiv:0709.1867 [nucl-ex], (2007).

[14] D. H. Rischke, Prog. Part. Nucl. Phys. 52, 197 (2004).

[15] D. Bailin and A. Love, Phys. Rept. 107, 325 (1984).

[16] S. B. Ruster, V. Werth, M. Buballa, I. A. Shovkovy and D. H. Rischke, Phys. Rev. D72, 034004 (2005).

[17] D. H. Rischke, M. I. Gorenstein, A. Schafer, H. Stocker and W. Greiner, Phys. Lett. B278, 19 (1992).

[18] CBM Progress Report, publicly available at http://www.gsi.de/fair/experiments/CBM, (2009).

[19] http://www.quantumdiaries.org/wp-content/uploads/2011/02/FlowPr.jpg, (2015).

[20] http://www.phy.duke.edu/research/NPTheory/QGP/transport/evo.jpg, (2015).

[21] K. Aamodt (ALICE collaboration), Phys. Rev. Lett. vol.105, 252301, (2010).

[22] S. Mrowczynski, Phys. Lett. B 269, 383 (1991).

[23] M. Gyulassy and M. Plumer, Phys. Lett. B 243, 432 (1990).

[24] M. Gyulassy, I. Vitev, and X. N. Wang, Phys. Rev. Lett. 86, 2537 (2001).

[25] J. Adams *et al.*, [STAR Collaboration], Phys. Rev. Lett. 91, 172302 (2003).

[26] R. J. Fries and B. Muller, Eur. Phys. J. C34 S279 (2004).

[27] K. Aamodt *et al.*, (ALICE Collaboration), Phys. Lett. B 696, 30 (2011).

[28] B. Abelev *et*4 *al.*, (ALICE collaboration), Phys. Rev. Lett. 110 ,082302 (2013).

[29] J. W. Cronin *et al.*, Phys. Rev. D11, 3105 (1975).

[30] S. S. Adler *et al.*, Phys. Rev. Lett. 91, No. 7, 072303, (2003).

[31] S. S. Adler *et al.*, Phys. Rev. Lett., Vol. 94, 232301, (2005).

[32] B. Abelev *et*4 *al.*, (ALICE collaboration), JHEP 1403 (2014) 013.

[33] B. Abelev *et al.*, [ALICE Collaboration], Phys. Lett. B720, 52-62 (2013).

[34] S. Chatrchyan *et al.*, [CMS Collaboration], Eur. Phys. J. C72, 1945 (2012).

[35] G. Aad *et*4 *al.*, (ATLAS collaboration), Phys. Lett. B719 220 (2013).

[36] T. Sjostrand, S. Mrenna, and P. Skands, JHEP 05, 026 (2006).

[37] B. Abelev *et al*, (ALICE collaboration), Phys. Lett. B734, 314–327 (2014).

[38] A. Adare *et al.*, (PHENIX collaboration), Phys. Rev. C84, 054912 (2011).

[39] S. Digal, P. Petreczky and H. Satz, Phys. Rev. D64 094015 (2001).

[40] N. Filipovic, (CMS collaboration), J. Phys. Conf. Series 612 (2015).

[41] W. Reisdorf and H. G. Ritter, Ann. Rev. Nucl. Part. Sci.47, 663 (1997).

[42] S. Voloshin and Y. Zhang Z., Phys. C70, 665 (1996).

[43] L. X. Han, G. L. Ma, Y. G. Ma, X. Z. Cai, J. H. Chen, S. Zhang and C. Zhong, Phys. Rev. C84, 064907 (2011) .

[44] F. G. Gardim, F. Grassi, M. Luzum and J. Y. Ollitrault, Phys. Rev. C85, 024908 (2012).

[45] H. Niemi, G. S. Denicol, H. Holopainen and P. Huovinen Phys. Rev. C87, 054901 (2013).

[46] S. Floerchinger and U. A. Wiedemann, Phys. Rev. C88, 044906 (2013).

[47] S. Floerchinger and U. A. Wiedemann, Phys. Lett. B728, 407-411 (2014).

[48] U. W. Heinz, AIP Conf. Proc. 739, 163 (2005).

[49] Z. Xu, C. Greiner and H. Stocker, J. Phys. G35, 104016 (2008).

[50] A. Adare *et al.*, Phys. Rev. Lett. 98, 162301 (2007).

[51] A. Taranenko, J. Phys. G34, 1069–1072 (2007).

[52] S. A. Voloshin, Nucl.Phys. A715, 379–388 (2003).

[53] D. Molnar and S. A. Voloshin, Phys. Rev. Lett. 91, 092301 (2003).

[54] B. Abelev (ALICE collaboration), JHEP 1506 190 (2015).

[55] M. Miller and R. Snellings, 2003, arXiv:nucl-ex/0321008, (2003).

[56] A. Bilandzic, R. Snellings and S. A. Voloshin, Phys.Rev. C83, 044913 (2011) .

[57] M. Luzum and P. Romatschke, Phys. Rev. C78, 034915, (2008).

[58] C. Herold, M. Nahrgang, I. Mishustin, M. Bleicher, Phys. Rev. C87, 014907, (2013).

[59] B. Betz, J. Noronha, G. Torrieri, M. Gyulassy, I. Mishustin and D. H. Rischke, Phys. Rev. C79, 034902 (2009) .

[60] I. Arsene *et al.*, Nucl. Phys. A757, 1 (2005).

[61] K. Adcox *et al.*, Nucl. Phys. A757, 184 (2005).

[62] B. B. Back *et al.*, Nucl. Phys. A757,28 (2005).

[63] J. Adams *et al.*, Nucl. Phys. A757, 102 (2005).

[64] E. Shuryak, Prog. Part. Nucl. Phys. 53, 273 (2004).

[65] C. Gale, S. Jeon, B. Schenke, P. Tribedy and R. Venugopalan, Phys. Rev. Lett. 110, 012302 (2013).

[66] I. Muller, Z. Phys. 198, 329 (1967).

[67] W. Israel, Ann. Phys. (N.Y.) 100, 310 (1976).

[68] W. Israel and J. M. Stewart, Phys. Lett. A58, 213 (1976).

[69] W. Israel and J. M. Stewart, Ann. Phys. (N.Y.) **118** (1979), 341.

[70] M. Grmela and H. C. Ottinger, Phys. Rev. E**56** (1997), 6620.

[71] H. C. Ottinger and M. Grmela, Phys. Rev. E**56** (1997), 6633.

[72] H. C. Ottinger, Phys. Rev. E**57** (1998), 1416.

[73] D. A. Teaney, arXiv:0905.2433 [nucl-th], (2009).

[74] C. Eckart, Phys. Rev. 58, 919 (1940).

[75] L. D. Landau and E. M. Lifshitz, Fluid Dynamics, Second Edition, Butterworth-Heinemann (1987).

[76] S. R. de Groot, W. A. van Leeuwen, Ch. G. van Weert, Relativistic kinetic theory - Principles and applications (North-Holland, 1980).

[77] L. P. Csernai, Introduction to Relativistic Heavy Ion Collisions, Wiley (1994).

[78] J. M. Stewart, Lecture notes in Physics, 10, Springer-Verlag (1971).

[79] J. M. Stewart, Proc. Roy. Soc. A357, 59 (1977).

[80] P. Huovinen and D. Molnar, Phys. Rev. C79, 014906 (2009).

[81] L. D. Landau and E. M. Lifshitz, Fluid Mechanics, Vol.6 of Course of Theoretical Physics. Butterworth-Heinemann, 2nd ed., Jan., (1987).

[82] V. Schneider *et al.*, J. Comput. Phys. 105, 92 (1993).

[83] U. W. Heinz, H. Song and A. K. Chaudhuri, Phys. Rev. C73, 034904 (2006).

[84] A. K. Chaudhuri, arXiv:0704.0134 [nucl-th], (2007).

[85] A. K. Chaudhuri, arXiv:0801.3180 [nucl-th], (2008).

[86] A. Muronga, Phys. Rev. C76, 014909 (2007).

[87] Comput. Phys. Commun. 185, 3016-3027 (2014).

[88] P. Petreczky, P. Huovinen, Nucl.Phys. A837, 26-53 (2010).

[89] S. Borsanyi *et al.*, J. High Energy Phys. 1011, 077 (2010).

[90] M. Laine, Y Schroder, Phys. Rev. D73, 085009 (2006).

[91] G. Boyd, J. Engels, F. Karsch, E. Laermann, C. Legeland, M. Lutgemeier and B. Petersson, Nucl. Phys. B469, 419 (1996).

[92] A. Bazavov *et al.*, Phys. Rev. D80, 014504 (2009).

[93] F. Cooper and G. Frye, Phys. Rev. D10, 186 (1974).

[94] P. V. Ruuskanen, Acta Phys. Polon. B18, 551 (1987).

[95] D. H. Rischke and M. Gyulassy, Nucl. Phys. A608, 479–512 (1996).

[96] C.W. Misner, K.S. Thorne and J.A. Wheeler, (W.H. Freeman, San Francisco, 1279 p, (1973).

[97] M.Chojnacki *et al.*, Comput. Phys. Commun. 183, 746-773, (2012).

[98] S. R. de Groot, W. van Leeuwen, and C. G. van Weert, Relativistic kinetic theory, Principles and applications. North-Holland, Amsterdam, Jan., (1980).

[99] J. Adams *et al.*, [STAR Collaboration], Phys. Rev. Lett. 92, 112301 (2004).

[100] W. Broniowski and W. Florkowski, Phys. Rev. Lett. 87, 272302 (2001).

[101] V. Begun, W. Florkowski and M. Rybczynski, Phys. Rev. C 90, 014906 (2013).

[102] C. Nonaka and S. A. Bass, Phys. Rev. C75, 014902 (2007).

[103] S. A. Bass and A. Dumitru, Phys. Rev. C61, 064909 (2000).

[104] K. A. Bugaev and M. I. Gorenstein, nucl-th/9903072 (1999).

[105] K. A. Bugaev, Nucl. Phys. A606, 559 (1996).

[106] J.J. Neumann, B. Lavrenchuk, and G. Fai, Heavy Ion Physics 5, 27 (1997).

[107] L. P. Csernai, Z. Lázár, and D. Molnar, Heavy Ion Phys. 5, 467 (1997).

[108] Cs. Anderlik, L. P. Csernai, F. Grassi, Y. Hama, T. Kodama, Zs. Lázár and H. Stocker, Heavy Ion Phys. 9, 193 (1999).

[109] K. Tamosiunas and L.P. Csernai, Eur. Phys. J. A20, 269 (2004).

[110] P. Braun-Munzinger, K. Redlich and J. Stachel, nucl-th/0304013, (2003), Published in In Hwa, R.C. (ed.) *et al.*: Quark gluon plasma 491-599.

[111] W. Florkowski, W. Broniowski and M. Michalec, Acta Phys. Polon. B33 761 (2002).

[112] E. Schnedermann, J. Sollfrank and U.W. Heinz, Phys. Rev. C48, 2462 (1993).

[113] F. Retiere and M.A. Lisa, Phys. Rev. C70, 044907 (2004).

[114] J. Cleymans and K. Redlich, Phys. Rev. C60, 054908 (1999).

[115] F. Becattini *et al.*, Phys. Rev. C64, 024901 (2001).

[116] P. Braun-Munzinger *et al.*, Phys. Lett. B518, 41 (2001).

[117] W. Florkowski, W. Broniowski and P. Bozek, J. Phys. G30, S1321 (2004).

[118] W. Broniowski, A. Baran and W. Florkowski, AIP Conf. Proc. 660, 185 (2003).

[119] A. Kisiel, W. Florkowski and W. Broniowski, Phys. Rev. C73, 064902 (2006).

[120] W. Broniowski *et al.*, Phys. Rev. Lett. 101, 022301 (2008).

[121] R. Hagedorn, Nuovo Cim. Suppl. 3, 147 (1965).

[122] R. Hagedorn and J. Ranft, Nuovo Cim. Suppl. 6, 169 (1968).

[123] R. Hagedorn, Invited talk at NATO Advanced Study Workshop on Hot Hadronic Matter: Theory and Experiment, Divonne-les-Bains, France, 27 June - 1 July 1994.

[124] W. Broniowski and W. Florkowski, Phys. Lett. B490, 223 (2000).

[125] W. Broniowski, W. Florkowski and L.Y. Glozman, Phys. Rev. D70, 117503 (2004).

[126] M. Petran, J. Letessier, J. Rafelski, G. Torrieri, Comput. Phys. Commun. 185, 2056-2079 (2014).

[127] S. Wheaton and J. Cleymans, Comput. Phys. Commun. 180, 84-106 (2009).

[128] Karsch, F. *et al*. Eur. Phys. J. C29, (2003).

[129] J. Cleymans and H. Satz, Z. Phys. C57, 135 (1993).

[130] E. Suhonen and S. Sohlo, J. Phys. G13, 1487 (1987); D. H. Rischke, M. I. Gorenstein, H. Stocker and W. Greiner, Z. Phys. C51, 4 85 (1991).

[131] P. Braun-Munzinger, I. Heppe and J. Stachel, Phys. Lett. B465, 15 (1999).

[132] A. Kisiel, T Taluc, W. Broniowski, W. Florkowski, Comput. Phys. Commun. 174, 669-687 (2006).

[133] B. Tomasik, Comput. Phys. Commun. 180, 1642 (2009) .

[134] X.F. Luo *et al*., J. Phys. G37, 094061 (2010).

[135] P. Bozek and I. Wyskiel, Phys. Rev. C81, 054902 (2010).

[136] M. M. Aggarwal *et al*., (STAR collaboration), Phys. Rev. Lett. 105, 022302 (2010).

[137] R. Brun and F. Rademakers, Nucl. Instrum. Meth. A389, 81 (1997), (http://root.cern.ch).

[138] P. Bozek and I. Wyskiel, Phys. Rev. C79, 044916 (2009).

[139] E. Molnar, H. Niemi, D.H. Rischke, Eur. Phys. J. C65, 615-635 (2010).

[140] J. P. Boris and D. L. Book, J. Comput. Phys. 11, 38 (1973).

[141] Schneider, V., Katscher, V., Rischke, D.H., Waldhauser, B., Marhun, J.A., and Munz, C.-D.,J. Comput. Phys. 105, 92–107 (1993).

[142] A. Kurganov, E. Tadmor, Journal of Computational Physics 160, 241-282 (2000).

[143] Nessyahu, H. and E. Tadmor, J. Comp. Phys. 87, 408–463 (1990).

[144] J. P. Boris, Naval Research Laboratory, NRL Memorandum Report 3237 (1976).

[145] J. P. Boris, A. M. Landsberg, E. S. Oran, J. H. Gardner, Naval Research Laboratory, (1993).

[146] G. Toth and D. Odstrcil, J. Comput. Phys. 128, 82 (1996).

[147] D. L. Book, C. Li, G. Patnaik and F. F. Grinstein, J. Sci. Comput. 6, 323 (1991).

[148] D. L. Book, J. P. Boris and K. Hain, J. Comput. Phys. 18, 248 (1975).

[149] C. R. DeVore, J. Comput. Phys. 92, 142 (1991).

[150] D.H. Rischke, S. Bernard, J.A. Maruhn, Nucl. Phys. A595, 346 (1995).

[151] R. Baier, A. H. Mueller, D. Schiff and D. T. Son, Phys. Lett. B502, 51 (2001).

[152] M. L. Miller, K. Reygers, S. J. Sanders and P. Steinberg, Ann. Rev. Nucl. Part. Sci. 57, 205-243 (2007).

[153] T. Hirano and Y. NaraF, Nucl. Phys. A743, 305 (2004).

[154] T. Hirano, U. W. Heinz, D. Kharzeev, R. Lacey and Y. Nara, Phys. Lett. B636, 299 (2006).

[155] F. Gelis, Int.J.Mod.Phys. A28, 1330001 (2013).

[156] H. J. Drescher, A. Dumitru, A. Hayashigaki, Y. Nara, Phys. Rev. C74,044905 (2006).

[157] H. J. Drescher, Y. Nara, Phys. Rev. C76, 041903 (2007).

[158] E. Iancu, R. Venugopalan, arXiv:hep-ph/0303204, (2003).

[159] A. Dumitru, Y. Nara, Phys. Rev. C85, 034907, (2012).

[160] L. P. Csernai, Y. Cheng, S. Horvat, V. Magas, D. Strottman and M. Zetenyi, J. Phys. G36, 064032 (2009).

[161] K. J. Eskola, H. Honkanen, H. Niemi, P. V. Ruuskanen and S. S. Rasanen, Phys. Rev. C72, 044904 (2005).

[162] Y. Hama, T. Kodama and O. J. Socolowski, Braz. J. Phys. 35, 24 (2005).

[163] R. P. G. Andrade, F. Grassi, Y. Hama, T. Kodama and W. L. Qian, Phys. Rev. Lett. 101, 112301 (2008).

[164] T. Hirano and K. Tsuda, Phys. Rev. C66, 054905 (2002) .

[165] B. Schenke, S. Jeon and C. Gale, Phys. Rev. C85, 024901 (2011).

[166] H. Petersen, G.-Y. Qin, S. A. Bass and B. Muller, Phys. Rev. C82, 041901 (2010).

[167] K. Werner, I. Karpenko, M. Bleicher, T. Pierog and S. Porteboeuf-Houssais, Phys. Rev. C85, 064907 (2012).

[168] A. Bohr and B. R. Mottelson, "Nuclear structure", (Benjamin, New York, 1969).

[169] P.Petrov for the ALICE collaboration, Acta Phys. Polon. Supp. 5, 263-270 (2012).

[170] A. Bialas, M. Bleszynski and W. Czyz, Nucl. Phys. B111, 461 (1976).

[171] P. F. Kolb, U. W. Heinz, P. Huovinen, K. J. Eskola and K. Tuominen, Nucl. Phys. A696, 197 (2001).

[172] D. Kharzeev and N. Nardi, Phys. Lett. B507, 121 (2001).

[173] R. J. Glauber, in "Lectures on theoretical physics", Vol.1, W.E. Brittin, L.G. Dunham eds., Interscience, NY, 1959.

[174] C. Y. Wong, "Introduction to high-energy heavy-ion collisions", World Scientific, Singapore, 1994.

[175] T.Hirano, Phys. Rev., C65, 011901 .

[176] T. Hirano and K. Tsuda, Phys. Rev. C66, 054905 (2002).

[177] T. Hirano, K. Morita, S. Muroya, and C. Nonaka, Phys. Rev. C65, 061902 (2002).

[178] T. Ishii and S. Muroya, Phys. Rev. D46, 5156 (1992).

[179] K. Morita, S. Muroya, H. Nakamura, and C. Nonaka, Phys. Rev., C61, 034904 (2000).

[180] K. Morita, S. Muroya, C. Nonaka, and T. Hirano, Phys. Rev., C66, 054904 (2002).

[181] B. Schenke, S. Jeon and C. Gale, Phys.Lett. B702 59 (2011).

[182] B. Tomášik, P. Lévai, J. Phys. G38, 095101 (2011).

[183] H. Song and U. Heinz, Phys. Rev. C77, 064901 (2008) .

[184] "`https://wiki.bnl.gov/TECHQM/index.php/Code_checking_list_in_3D_ideal_fluid_dynamics`", "2016 (accessed January 15, 2016)"

[185] P. Kolb and U. Heinz, nucl-th/0305084, Published in In Hwa, R.C. (ed.) *et al.*: Quark gluon plasma 634-714.

[186] J. D. Bjorken, Phys. Rev. D 27, 140 (1983).

[187] H. Sorge, Phys. Rev. Lett. 82, 2048 (1999).

[188] B. Alver *et al.*, [PHOBOS Collaboration], Phys. Rev. Lett. 98, 242302 (2007).

[189] https://cdsweb.cern.ch/record/1472935 (2012).

[190] J. Jia *et al.*, (ATLAS Collaboration), Nucl.Phys. A904-905 421c-424c (2013).

[191] B. H. Alver, C. Gombeaud, M. Luzum and J. Y. Ollitrault, Phys. Rev. C82, 034913 (2010).

[192] Z. Qiu and U. W. Heinz, Phys. Rev. C84, 024911 (2011).

[193] B. Schenke, P. Tribedy, R. Venugopalan, Phys. Rev. Lett. 108, 252301 (2012).

[194] B. Schenke, P. Tribedy and R. Venugopalan, Phys. Rev. C86, 034908 (2012).

[195] J. Bartels, K. J. Golec-Biernat and H. Kowalski, Phys. Rev. D66, 014001 (2002).

[196] H. Kowalski and D. Teaney, Phys. Rev. D68, 114005 (2003).

[197] A. Kovner, L. D. McLerran and H. Weigert, Phys. Rev. D52, 6231 (1995).

[198] Y. V. Kovchegov and D. H. Rischke, Phys. Rev. C56, 1084 (1997).

[199] A. Krasnitz and R. Venugopalan, Nucl. Phys. B557, 237 (1999).

[200] A. Krasnitz and R. Venugopalan, Phys. Rev. Lett. 84, 4309 (2000).

[201] A. Krasnitz and R. Venugopalan, Phys. Rev. Lett. 86, 1717 (2001).

[202] T. Lappi, Phys. Rev. C67, 054903 (2003).

[203] H. Kowalski, L. Motyka and G. Watt, Phys. Rev. D74, 074016 (2006).

[204] H. Kowalski, T. Lappi and R. Venugopalan, Phys. Rev. Lett. 100, 022303 (2008).

[205] C. Gale, S. Jeon, B. Schenke, Int. J. Mod. Phys. A28, 1340011 (2013).

[206] K. Dusling, F. Gelis and R. Venugopalan, Nucl. Phys. A872, 161 (2011).

[207] K. Dusling, T. Epelbaum, F. Gelis and R. Venugopalan, Nucl. Phys. A850, 69 (2011).

[208] T. Epelbaum and F. Gelis, Nucl. Phys. A872, 210 (2011).

[209] K. Dusling, T. Epelbaum, F. Gelis and R. Venugopalan, Phys. Rev. D86, 085040 (2012).

[210] G. Aad *et al.* (ATLAS Collaboration), Phys. Rev. C86, 014907 (2012).

[211] mckln3.52 by Yasushi Nara, http://www.aiu.ac.jp/∼ynara/mckln/, 24th March 2015.

[212] H. Niemi, G. S. Denicol, P. Huovinen, E. Molnar, and D. H. Rischke, Phys. Rev. Lett. 106, 212302 (2011).

[213] K. Aamodt *et al.* (ALICE Collaboration), Phys. Rev. Lett. 107, 032301 (2011).

[214] ALICE collaboration, Phys. Lett. B 746, 1 (2015).

[215] ATLAS collaboration, Phys.Rev.Lett. 114, 7, 072302 (2015).

[216] E. Iancu and B. Wu, JHEP 1510, 155 (2015).

[217] X. F. Guo and X. N. Wang, Phys. Rev. Lett. 85, 3591 (2000).

[218] P. B. Arnold, G. D. Moore and L. G. Yaffe, JHEP 0206, 030 (2002).

[219] M. Gyulassy, P. Levai and I. Vitev, Nucl. Phys. B571, 1970 (2000).

[220] R. Baier, Y. L. Dokshitzer, A. H. Mueller, S. Peigne and D. Schiff, Nucl. Phys. B483, 291-320 (1997).

[221] C. A. Salgado and U. A. Wiedemann, Phys. Rev. Lett. 89, 092303 (2002).

[222] W. A. Horowitz and M. Gyulassy, Nucl. Phys. A872, 265 (2011).

[223] A. Adare *et al.*, [PHENIX Collaboration], Phys.Rev. C87, 3, 034911 (2013).

[224] N. Armesto, L. Cunqueiro, C.A. Salgado and W.C. Xiang: JHEP 0802, 048 (2008).

[225] T. Renk: Phys. Rev. C 78, 034908 305 (2008).

[226] J. W. Qiu and G. Sterman, Nucl. Phys. B353, 105 (1991).

[227] E. Braaten and R. D. Pisarski, Phys. Rev. Lett.64, 1338 (1990).

[228] U. A. Wiedemann, Nucl. Phys. B582, 409 (2000).

[229] M. Gyulassy and X. N. Wang, Nucl. Phys. B420, 583 (1994).

[230] A. Adare *et al.*, [PHENIX Collaboration]: Phys. Rev. Lett. 101, 232301 (2008).

[231] S.A. Bass *et al.*, J. Phys. G35 (2008).

[232] R. B. Neufeld, Phys. Rev. D78, 085015 (2008).

[233] J. J. Friess, S. S. Gubser, G. Michalogiorgakis and S. S. Pufu, Phys. Rev. D75, 106003 (2007).

[234] S. S. Gubser and A. Yarom, Phys. Rev. D77, 066007 (2008).

[235] P. M. Chesler and L. G. Yaffe, Phys. Rev. D78, 045013 (2008).

[236] T. Renk, Phys. Rev. C85, 044903 (2012).

[237] T. Renk, H. Holopainen, R. Paatelainen and K. J. Eskola, Phys. Rev. C84, 014906 (2011).

[238] B. Betz, J. Noronha, G. Torrieri, M. Gyulassy and D. H. Rischke, Phys. Rev. Lett. 105, 222301 (2010).

[239] B. Betz, EPJ Web Conf. 13, 07002 (2011).

[240] B. Betz and M. Gyulassy, JHEP 1408, 090 (2014).

[241] B. Betz, EPJ Web Conf 13, 07002 (2011).

[242] A. Andronic *et al.*, [FOPI Collaboration], Nucl. Phys. A679, 765 (2001).

[243] A. Andronic *et al.*, [FOPI Collaboration], Phys. Rev. C64, 041604 (2001).

[244] A. Taranenko *et al.*, [TAPS Collaboration], Czech. J. Phys. 50S4, 139-166 (2000).

[245] P. L. Jain, G. Singh and A. Mukhopadhyay, Phys. Rev. Lett. 74, 1534 (1995).

[246] J. Barrette *et al.*, [E877 Collaboration], Phys. Rev. Lett. 73, 2532 (1994).

[247] J. Barrette *et al.*, [E877 Collaboration], Phys. Lett. B485, 319 (2000).

[248] K. Aamodt *et al.*, (ALICE Collaboration), Phys. Rev. Lett. 105, 252302, (2010).

[249] G. Agakichiev *et al.*, [CERES/NA45 Collaboration], J.Phys. G30, S709-S716 (2004).

[250] H. Appelshauser *et al.*, [NA49 Collaboration], Phys. Rev. Lett. 80, 4136 (1998).

[251] C. Alt *et al.*, [NA49 Collaboration], Phys. Rev. C68, 034903 (2003).

[252] M. M. Aggarwal *et al.*, [WA98 Collaboration], Phys. Lett. B469, 30 (1999).

[253] P. Danielewicz and G. Odyniec, Phys. Lett. B 157, 146, (1985).

[254] A. M. Poskanzer and S. A. Voloshin, Phys. Rev. C58, 1671-1678 (1998).

[255] M. Schulc and B. Tomášik, J. Phys. G40, 125104 (2013).

[256] R. P. G. Andrade, J. Noronha, G. S. Denicol, Phys. Rev. C90, 024914 (2014).

[257] T. Hirano and Y. Tachibana, Phys.Rev. C90, 021902, (2014).

[258] S. Floerchinger and K. C. Zapp, Eur. Phys. J. C74, 3189 (2014).

[259] K. C. Zapp and S. Floerchinger, Nucl. Phys. A931, 388 (2014).

[260] CMS collaboration, JHEP 1402, 088 (2014).

[261] I. Bouras, B. Betz, Z. Xu and C. Greiner, Phys.Rev. C90, 2, 024904 (2014).